NATIONAL TECHNICAL UNIVERSITY OF ATHENS
SCHOOL OF RURAL AND SURVEYING ENGINEERING
POSTGRADUATE PROGRAM ‘GEOINFORMATICS’

Soil Moisture Estimation based on Multispectral and SAR Satellite Data using Google Earth Engine and Machine Learning

Master Thesis

Vasiliki-Maria Pegiou-Malakou

Athens, October 2018

RSLab
Remote Sensing Laboratory
National Technical University of Athens
✓ Sensing ✓ Analytics ✓ Monitoring

ΕΘΝΙΚΟ ΜΕΤΣΟΒΙΟ ΠΟΛΥΤΕΧΝΕΙΟ
ΣΧΟΛΗ ΑΓΡΟΝΟΜΩΝ ΚΑΙ ΤΟΠΟΓΡΑΦΩΝ ΜΗΧΑΝΙΚΩΝ
ΠΡΟΓΡΑΜΜΑ ΜΕΤΑΠΤΥΧΙΑΚΩΝ ΣΠΟΥΔΩΝ «ΓΕΩΠΛΗΡΟΦΟΡΙΚΗ»

Εκτίμηση Εδαφικής Υγρασίας από Πολυφασματικά και Ραντάρ Δορυφορικά Δεδομένα με χρήση του Google Earth Engine και Τεχνικών Μηχανικής Μάθησης

ΜΕΤΑΠΤΥΧΙΑΚΗ ΕΡΓΑΣΙΑ

Βασιλική-Μαρία Πέγιου-Μαλακού

Αθήνα, Οκτώβριος 2018

ΕΘΝΙΚΟ ΜΕΤΣΟΒΙΟ ΠΟΛΥΤΕΧΝΕΙΟ
ΣΧΟΛΗ ΑΓΡΟΝΟΜΩΝ ΚΑΙ ΤΟΠΟΓΡΑΦΩΝ ΜΗΧΑΝΙΚΩΝ
ΠΡΟΓΡΑΜΜΑ ΜΕΤΑΠΤΥΧΙΑΚΩΝ ΣΠΟΥΔΩΝ «ΓΕΩΠΛΗΡΟΦΟΡΙΚΗ»

Εκτίμηση Εδαφικής Υγρασίας από Πολυφασματικά και Ραντάρ Δορυφορικά Δεδομένα με χρήση του Google Earth Engine και Τεχνικών Μηχανικής Μάθησης

ΜΕΤΑΠΤΥΧΙΑΚΗ ΕΡΓΑΣΙΑ

Βασιλική-Μαρία Πέγιου-Μαλακού

……………..

Επιβλέπων : Κωνσταντίνος Καράντζαλος
Αν. Καθηγητής Ε.Μ.Π.

Εγκρίθηκε από την τριμελή εξεταστική επιτροπή την 25η Οκτωβρίου 2018.

(Υπογραφή)	*(Υπογραφή)*	*(Υπογραφή)*
....	....	....
Κωνσταντίνος Καράντζαλος Αν. Καθηγητής Ε.Μ.Π.	Δημήτριος Αργιαλάς Καθηγητής Ε.Μ.Π.	Παντελής Μπαρούχας Επ. Καθηγητής Τ.Ε.Ι.Δ.Ε.

To my grandmother, my grandfather,
my mom and my little brother,
who supported me and whom I truly love,
as well as to all the friends of mine who were close
to me the whole time of this accomplishment.

Table of Contents

ACKNOWLEDGEMENTS 5

ABSTRACT 6

ΕΚΤΕΝΗΣ ΠΕΡΙΛΗΨΗ 7

1 INTRODUCTION 1

  1.1 SOIL MOISTURE 1

  1.2 REMOTE SENSING 5

    1.2.1 ACTIVE AND PASSIVE SENSORS 5

    1.2.2 SENTINEL 1 6

    1.2.3 LANDSAT 8 12

  1.3 LITERATURE REVIEW 16

  1.4 STUDY AREA 18

2 GEOSPATIAL DATA 20

  2.1 GEOSPATIAL FRAMEWORKS AND COMPUTATIONAL TOOLS 27

    2.1.1 GOOGLE EARTH ENGINE 27

    2.1.2 R STATISTICAL PACKAGE 30

3 METHODOLOGY 33

4 EXPERIMENTAL RESULTS 45

5 DISCUSSION 68

6 CONCLUSION 70

7 REFERENCES 72

  7.1 WEB PAGES 77

APPENDICES 78

  APPENDIX A – Sentinel 1 Metadata of the Selected Images 78

  APPENDIX B – Landsat 8 Metadata of the Selected Images 92

LIST OF FIGURES 95

LIST OF TABLES 97

ACKNOWLEDGEMENTS

First and foremost, I wish to express my sincere gratitude to my advisor and research supervisor, Prof. Konstantinos Karantzalos, for his patience, motivation, dedicated involvement and immense knowledge. The door to Prof. Karantzalos office was always open in case I ran into a dead end or had any kind of question about my research, steering me in the right direction whenever I needed it. He showed tremendous comprehension to the fact that sometimes my time was limited and did not let this to be a suppressive factor to finish my research. His aspiring guidance, invaluably constructive criticism and friendly advice on my research were more than valuable and I could not have imagined having a better advisor and mentor for my Master's degree study.

Furthermore, I would like to extend my gratitude to Prof. Pantelis Barouchas, Assistant Professor in the Department of Agricultural Technology in the Technological Educational Institute of Western Greece, for providing me with the appropriate In Situ soil moisture data.

I also place on record, my sincere thank you to all the developers who helped me in the Google Earth Engine Developers list, by responding to my -sometimes maybe really basic-questions and especially to Gennadii Donchyts who kept on replying to every occurring question I was coming up with after his responses.

Moreover, I would like to express my sense of thankfulness to one and all, who directly or indirectly, have lent their hand in this venture.

Last but by no means least, I must take this opportunity to express my very profound gratitude to my beloved family, my partner and my friends for providing me with unfailing moral and emotional support and unceasing encouragement throughout my years of study as well as through the process of researching and writing this dissertation. This accomplishment stands as a testament to their unconditional love and encouragement and would not have been possible without them.
Thank you.

Vasiliki Pegiou

Abstract

Soil Moisture can be described as the level of saturation in the upper soil layer relative to the soil field capacity, regulated by the precipitation and potential evaporation, while being highly variable in space and time. It constitutes a key factor for agricultural management such as optimizing the fertilizer rates and irrigation, applying pesticides or herbicides and crop management. Moreover, soil moisture is considered as valuable information in many sectors such as Hydrology, Biogeography, Geomorphology, Agronomy and Climatology. To this end, the main objective in this master thesis was to evaluate the concurrent use of satellite multispectral and SAR radar data for estimating soil moisture in large spatial scales. In particular, Landsat 8 Surface Reflectance data as well as Sentinel 1 GRD SAR data were employed in the region of Arta across the Amvrakikos Gulf and the Amvrakikos Wetlands Natural Park. Recent studies have indicated that the amplitude derived by SAR data in VV polarization along with information about the Normalized Difference Vegetation Index (NDVI), the Normalized Difference Moisture Index (NDMI) and the Moisture Index (MI) from multispectral data can be proxies of soil moisture. In-situ measurements from the Enhydris project were also acquired spanning three different years. Google Earth Engine was exploited for mining the satellite data through the Javascript API services. Then several experiments we performed in order to establish correlations between the In-Situ and satellite data based on statistical and machine learning tools like Linear Regression, Polynomial Regression, Generalized Additive Models (based on R Statistical tool), as well deep learning models, using the TensorFlow Framework in association with the Keras library in R. Generally speaking, based on the considered relative large, multitemporal dataset, the statistical approaches did not manage to establish concrete correlations in any of the performed experiments and combinations. The MI index along with the VV backscatter though was closer to the expressed variation in the In-Situ dataset. Based on the deep machine learning framework, stronger correlations were established between the In-Situ data from Enhydris and a combination of VV amplitude and NDVI satellite observations.

Keywords: *Remote Sensing, Earth Observation, Radar, High Resolution, Deep Learning, Correlation, In-situ, Soil, R*

ΕΚΤΕΝΗΣ ΠΕΡΙΛΗΨΗ

Βασική επιδίωξη της παρούσας εργασίας αποτέλεσε η εκτίμηση της εδαφικής υγρασίας με χρήση ταυτόχρονα πολυφασματικών και ραντάρ δορυφορικών δεδομένων. Τα βασικά υπολογιστικά εργαλεία για την εκτίμηση και ανάπτυξη συσχετίσεων μεταξύ των δορυφορικών παρατηρήσεων και των δεδομένων εδάφους ήταν η πολυμεταβλητή στατιστική ανάλυση, τεχνικές μηχανικής μάθησης αλλά και τεχνολογίες διαχείρισης και ανάκτησης μεγάλων γεωχωρικών δεδομένων όπως το Google Earth Engine. Στα πλαίσια της μελέτης και υλοποίησης αξιοποιήθηκαν νέες τεχνολογίες, αλγόριθμοι και συστήματα, όπου με αυτόματο τρόπο δίνουν τη δυνατότητα για συστηματική ανάκτηση και επεξεργασία δορυφορικών και γεωχωρικών δεδομένων.

Εδαφική Υγρασία

Η εδαφική υγρασία ορίζεται ως το επίπεδο κορεσμού στο ανώτερο στρώμα του εδάφους και εξαρτάται από τις κατακρημνίσεις και την εξατμισοδιαπνοή. Η εδαφική υγρασία μεταβάλλεται τόσο στο χώρο όσο και στο χρόνο και αποτελεί ιδιαίτερα σημαντικό παράγοντα για την υγεία και την ανάπτυξη της βλάστησης και των καλλιεργειών, αφού μέσω αυτής διαλύονται τα συστατικά του εδάφους ενώ παράλληλα συμβάλλει στην φωτοσύνθεση. Επιπλέον, συμβάλλει στην διαπνοή των φυτών και την εξατμισοδιαπνοή στο έδαφος, η οποία επηρεάζει την θερμοκρασία καθώς και την υγρασία του επιφανειακού ανέμου. Τέλος, η εκτίμηση της εδαφικής υγρασίας είναι μια ιδιαίτερα σημαντική πληροφορία για την διαχείριση των καλλιεργειών και την λήψη σχετικών αποφάσεων όπως η άρδευση.

Περιοχή Μελέτης

Η περιοχή μελέτης της παρούσας έρευνας βρίσκεται στο νότιο τμήμα του Νομού Άρτας, στην Ήπειρο, και περιλαμβάνει την πεδιάδα της Άρτας καθώς και το Εθνικό Πάρκο Υγροτόπων Αμβρακικού, που εκτείνεται κατά μήκος του Αμβρακικού Κόλπου. Η πεδιάδα της Άρτας, η οποία είναι και η μεγαλύτερη σε έκταση πεδινή περιοχή του νομού, βρίσκεται στο νοτιότερο τμήμα της Ηπείρου και αποτελεί μέρος των υδρολογικών λεκανών των ποταμών Λούρου και Άραχθου. Χαρακτηρίζεται από χαμηλές κλίσεις και υψόμετρα, της τάξεως του 0%-25% και 0m έως 100m αντίστοιχα, ενώ το κλίμα της περιοχής είναι Μεσογειακού τύπου με ήπιους, βροχερούς χειμώνες και υψηλές θερμοκρασίες κατά την θερινή περίοδο. Ο Αμβρακικός Κόλπος συνδέεται με το Ιόνιο Πέλαγος και καταλαμβάνει μια έκταση 405km^2, με μέσο βάθος τα 26m. Τα μορφολογικά του χαρακτηριστικά οφείλονται τόσο σε φυσικούς όσο και σε ανθρωπογενείς παράγοντες και αποτελεί προστατευόμενη περιοχή μέσω της Συνθήκης Ramsar (Ramsar, 2014). Οι υγρότοποι του Αμβρακικού εκτείνονται στις βόρειες ακτές του Αμβρακικού Κόλπου και στο ανώτερο τμήμα τους συναντούν την πεδιάδα της Άρτας. Χαρακτηρίζονται από ιδιαίτερα και πολύπλοκα μορφολογικά χαρακτηριστικά ενώ φιλοξενούν μεγάλη ποικιλία πανίδας με σπάνια και υπό εξαφάνιση είδη. Το Εθνικό Πάρκο Υγροτόπων του Αμβρακικού περιλαμβάνει ένα μεγάλο τμήμα της πεδιάδας της Άρτας και τους υγροτόπους, ενώ είναι σημαντικό να αναφερθεί ότι αποτελεί μια από τις σημαντικότερες προστατευόμενες περιοχές της Ευρώπης ανήκοντας στο δίκτυο των περιοχών NATURA 2000 (EEA, 2014; ΕΚΒΥ, 2014).

Γεωχωρικά Δεδομένα

Στην έρευνα αυτή χρησιμοποιήθηκαν τόσο οπτικά δεδομένα όσο και δεδομένα radar. Το χρονικό εύρος που εξετάστηκε καθώς και οι ακριβείς ημερομηνίες λήψης των δεδομένων προέκυψαν ως συνάρτηση της διαθεσιμότητας του συνόλου των δεδομένων, δηλαδή σύμφωνα με την διαθεσιμότητα τόσο των επίγειων όσο και των δορυφορικών μετρήσεων. Οι επίγειες μετρήσεις που χρησιμοποιήθηκαν στα πλαίσια της παρούσας μελέτης, αντλήθηκαν από την Βάση Δεδομένων «Ενυδρίς» και διέθεταν επίγειες μετρήσεις της εδαφικής υγρασίας από 6 σταθμούς. Τα δεδομένα της βάσης «Ενυδρίς» είναι προσβάσιμα μέσω της αντίστοιχης διαδικτυακής διεπαφής (http://system.irrigation-management.eu και https://enhydris.readthedocs.org) και περιλαμβάνουν χρονοσειρές τόσο Μετεωρολογικών όσο και Υδρολογικών δεδομένων. Οι σταθμοί που επιλέχθηκαν βρίσκονταν στις περιοχές Άγιος Σπυρίδωνας, Καμπή, Κομμένο, Κόμποτι, ΤΕΙ Ηπείρου – Κωστακιοί και ΤΟΕΒ Λούρου.

Τα δορυφορικά δεδομένα που χρησιμοποιήθηκαν, αντλήθηκαν από το Google Earth Engine, και περιλάμβαναν εικόνες από τους δορυφόρους Landsat 8 και Sentinel 1. Το Google Earth Engine εκτός από τα αρχικά, παρέχει την πρόσβαση και σε προεπεξεργασμένα δεδομένα συμβάλλοντας έτσι σε μικρότερους απαιτούμενους χρόνους επεξεργασίας. Τα πολυφασματικά δεδομένα που χρησιμοποιήθηκαν, έχουν παραχθεί από τον δορυφόρο Landsat 8 και συγκεκριμένα αξιοποιήθηκε η πληροφορία επιφανειακής ανακλαστικότητας. Το συγκεκριμένο σετ δεδομένων αφορά ατμοσφαιρικά διορθωμένα δεδομένα του οργάνου καταγραφής OLI/TIRS. Κάθε εικόνα περιείχε 5 φασματικά κανάλια στο τμήμα του ορατού και του εγγύς υπέρυθρου, 2 φασματικά κανάλια στο τμήμα του μέσου υπέρυθρου καθώς και 2 στο θερμικό υπέρυθρο. Όσον αφορά τα radar δεδομένα που επιλέχθηκαν, λήφθηκαν από τον δορυφόρο Sentinel 1 και συγκεκριμένα από το Radar Συνθετικού Ανοίγματος (SAR), ενώ ήταν τύπου GRD.

Ανάλυση

Τα δεδομένα SAR είχαν υποστεί προεπεξεργασία κατά την οποία είχαν ενημερωθεί τα δεδομένα τροχιάς, είχαν απαλλαχθεί από θορύβους, ήταν ραδιομετρικά διορθωμένα και τέλος είχαν υποστεί ορθοαναγωγή. Επιπλέον οι τιμές του οπισθοσκεδαζόμενου σήματος ήταν εκφρασμένες σε decibels (db). Η μεθοδολογία που επιλέχθηκε για την εκπόνηση της παρούσας μελέτης περιλάμβανε την εφαρμογή και αξιολόγηση μεθόδων πολυμεταβλητής στατιστικής ανάλυσης και μηχανικής μάθησης όπως Γραμμική Παλινδρόμηση, Πολυωνυμική Παλινδρόμηση, Γενικευμένα Προσθετικά Μοντέλα και Τεχνητά Νευρωνικά Δίκτυα. Πιο συγκεκριμένα, αρχικά πραγματοποιήθηκε η προεπεξεργασία των δορυφορικών δεδομένων στο περιβάλλον του Google Earth Engine σε γλώσσα προγραμματισμού Javascript. Στο Google Earth Engine εισήχθησαν τα σημεία όπου βρίσκονται οι σταθμοί των μετρήσεων αφού μετατράπηκαν σε Fusion Tables από την μορφή Shapefile χρησιμοποιώντας το web-based περιβάλλον του Shape Escape. Έχοντας φιλτράρει τις συλλογές δεδομένων που παρέχονται στο Google Earth Engine με βάση τις επιθυμητές παραμέτρους κι έχοντας τις εικόνες που αναφέρθηκαν παραπάνω, υπολογίστηκαν οι τιμές 3 δεικτών στα σημεία των σταθμών των μετρήσεων, με βάση τα δεδομένα Επιφανειακής Ανακλαστικότητας του δορυφόρου Landsat 8. Οι δείκτες αυτοί ήταν ο Κανονικοποιημένος Δείκτης Βλάστησης (NDVI), ο Κανονικοποιημένος Δείκτης Υγρασίας (NDMI) και ο Δείκτης Υγρασίας (MI). Στην συνέχεια, χρησιμοποιώντας τα δεδομένα του δορυφόρου Sentinel 1, εξήχθησαν και οι τιμές οπισθοσκέδασης σε πόλωση VV, στα σημεία των σταθμών των μετρήσεων. Αφού συλλέχθηκαν όλες οι απαραίτητες τιμές για τον κάθε σταθμό, εξήχθησαν 6 αρχεία μορφής .csv από την επεξεργασία των δορυφορικών δεδομένων Landsat 8 και άλλα 6 αρχεία από την επεξεργασία των δορυφορικών δεδομένων Sentinel 1. Οι τελικές συλλογές δεδομένων από τα δεδομένα Landsat 8 περιείχαν από 39 εγγραφές κάθε μεταβλητής για τους σταθμούς Άγιος Σπυρίδωνας, Καμπή και ΤΟΕΒ Λούρου, 43 εγγραφές για τον σταθμό ΤΕΙ Ηπείρου-Κωστακιοί και 84 εγγραφές στους σταθμούς Κομπότι και Κομμένο. Το αποτέλεσμα ήταν ένα σετ δεδομένων 328 εγγραφών. Αντίστοιχα, από τα δεδομένα Sentinel 1 εξήχθησαν από 144 εγγραφές τιμών οπισθοσκέδασης των σταθμών Άγιος Σπυρίδωνας, Κομμένο, Κομπότι, ΤΕΙ Ηπείρου-Κωστακιοί και ΤΟΕΒ Λούρου ενώ για τον σταθμό Καμπή εξήχθησαν 145 εγγραφές, οδηγώντας σε ένα τελικό σετ δεδομένων 865 εγγραφών. Σε κάθε εγγραφή των προαναφερθέντων σετ δεδομένων εντοπίστηκαν και συνενώθηκαν οι αντίστοιχες πραγματικές μετρήσεις εδαφικής υγρασίας. Στα παρακάτω διαγράμματα απεικονίζονται οι χρονοσειρές των μεταβλητών που εξήχθησαν.

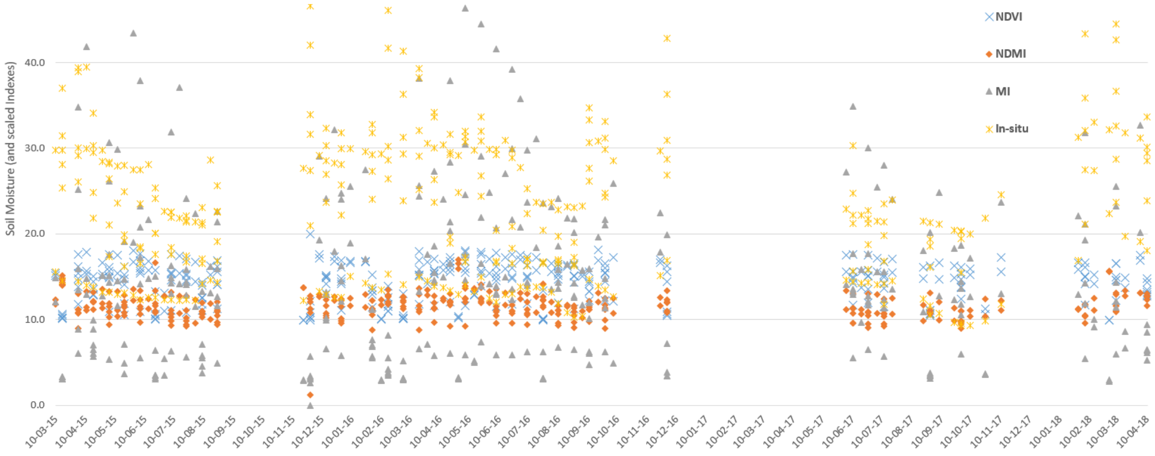

Figure 1: Επίγειες μετρήσεων εδαφικής υγρασίας (In-situ) και τιμές πολυφασματικών δεικτών NDVI, NDMI, MI. Συνολικά 328 μετρήσεις και αντίστοιχες τιμές (x10) NDVI, (x10) NDMI και (x3) MI σε ένα διαστημα +/- 2 ημερών.

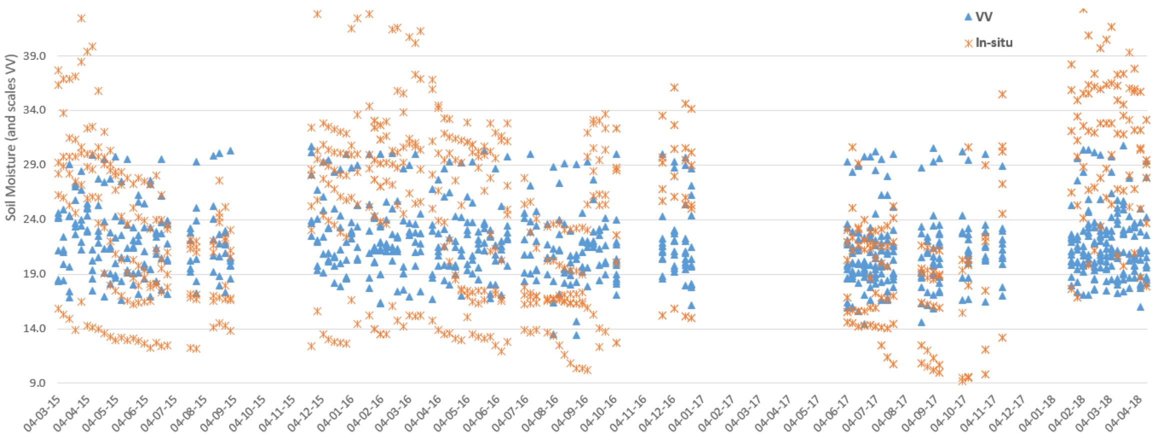

Figure 2: Επίγειες μετρήσεων εδαφικής υγρασίας (In-situ) και τιμές οπισθοσκέδασης VV (db). Συνολικά 865 μετρήσεις και αντίστοιχες τιμές (+30) VV σε ένα διαστημα +/- 2 ημερών.

Συσχετίσεις και Αξιολόγηση

Αφού ολοκληρώθηκε η προετοιμασία των δεδομένων, χωρίστηκαν σε δεδομένα εκπαίδευσης (training set), επιλέγοντας το 80% των συνολικών δεδομένων, και σε δεδομένα επαλήθευσης (validation set), όπου επιλέχθηκε το υπόλοιπο 20% των συνολικών δεδομένων, κι εφαρμόστηκε μια σειρά πειραμάτων για την ανάπτυξη συσχετίσεων. Η πρώτη μεθοδολογία που υλοποιήθηκε, αφορούσε την ανάπτυξη ενός Μοντέλου Γραμμικής Παλινδρόμησης χρησιμοποιώντας ως εξαρτημένη μεταβλητή τις επίγειες μετρήσεις της εδαφικής υγρασίας και κάθε φορά μια από τις μεταβλητές NDVI, NDMI, MI, Οπισθοσκέδαση VV, ως ανεξάρτητη μεταβλητή. Οι τιμές που ελέγχθηκαν με σκοπό την αξιολόγηση των αποτελεσμάτων ήταν η Τετραγωνική Ρίζα του Μέσου Τετραγωνικού Σφάλματος (RMSE), ο συντελεστής Pearson στο τετράγωνο (r^2) και ο συντελεστής Spearman (p-value). Στην συνέχεια αναπτύχθηκε κι εφαρμόστηκε μια σειρά Μοντέλων Πολυωνυμικής Παλινδρόμησης για κάθε μια από τις ανεξάρτητες μεταβλητές και αξιολογήθηκαν με βάση τις τιμές των παραμέτρων που αναφέρθηκαν και στα μοντέλα Γραμμικής Παλινδρόμησης. Έπειτα, υλοποιήθηκε μια σειρά Γενικευμένων Προσθετικών Μοντέλων για κάθε μια από τις ανεξάρτητες μεταβλητές, τα οποία αξιολογήθηκαν με βάση την Τετραγωνική Ρίζα του Μέσου Τετραγωνικού Σφάλματος (RMSE) και τον συντελεστή Pearson στο τετράγωνο (r^2).

Αφού υλοποιήθηκαν τα παραπάνω μοντέλα, σειρά είχε η εφαρμογή μιας τεχνικής Βαθιάς Μηχανικής Μάθησης, με Τεχνητά Νευρωνικά Δίκτυα, χρησιμοποιώντας αυτή την φορά δυο ανεξάρτητες μεταβλητές, τον NDVI και τις τιμές Οπισθοσκέδασης VV. Για να γίνει αυτό εφικτό, κρίθηκε σκόπιμο να εντοπιστούν οι εικόνες Landsat 8 και Sentinel 1 με διαφορά ημερομηνιών +-2 μέρες. Η συγχώνευση των εικόνων έγινε με την χρήση του Google Earth Engine από το οποίο προέκυψαν 6 σετ δεδομένων, ένα για κάθε σταθμό, όπου το καθένα περιλάμβανε 19 εγγραφές. Το τελικό αποτέλεσμα ήταν ένα σετ δεδομένων με 114 εγγραφές. Η υλοποίηση των Τεχνητών Νευρωνικών Δικτύων πραγματοποιήθηκε με την χρήση της προγραμματιστικής γλώσσας R. Αρχικά τα δεδομένα χωρίστηκαν σε δεδομένα εκπαίδευσης και δεδομένα επαλήθευσης όπως πραγματοποιήθηκε και κατά την εφαρμογή των προηγούμενων τεχνικών, όπου το 80% των δεδομένων χρησιμοποιήθηκε ως δεδομένα εκπαίδευσης ενώ το υπόλοιπο 20% ως δεδομένα επαλήθευσης. Στην συνέχεια, κρίθηκε απαραίτητη η κανονικοποίηση των δεδομένων σε κλίμακα [0,1]. Η διαδικασία αυτή αποτελεί απαραίτητο βήμα πριν την εισαγωγή των δεδομένων στα Τεχνητά Νευρωνικά Δίκτυα. Αφού δοκιμάστηκαν διάφορες τεχνικές υλοποίησης Νευρωνικών Δικτύων, η πιο αποτελεσματική ήταν η χρήση του εργαλείου TensorFlow σε συνδυασμό με την βιβλιοθήκη Keras. Το αρχικό βήμα περιείχε το ορισμό των παραμέτρων του μοντέλου Νευρωνικών Δικτύων, κατά τον οποίο ορίστηκε ένας αρχικός αριθμός Κρυφών Επιπέδων και των Νευρώνων τους, καθώς και η συνάρτηση ενεργοποίησης. Η συνάρτηση ενεργοποίησης που επιλέχθηκε ήταν οι γραμμικές μονάδες ανόρθωσης, γνωστές με το ακρώνυμο ReLU. Η επιλογή των παραμέτρων δεν βασίζεται σε κάποιον κανόνα αλλά στην διαδικασία δοκιμής και σφάλματος. Η διαδικασία μάθησης ορίστηκε ώστε να πραγματοποιεί 100 επαναληπτικά περάσματα στα δεδομένα (epochs). Αφού ορίστηκαν όλες οι απαραίτητες παράμετροι, εκτελέστηκε η διαδικασία εκπαίδευσης κι αξιολόγησης των τελικών μοντέλων.

Τα αποτελέσματα που προέκυψαν από τα πολλαπλά πειράματα με τη ανάλυση παλινδρόμησης έδειξαν σε γενικές γραμμές ότι δεν υπήρξαν συσχετίσεις για το γενικευμένο σετ δεδομένων και τις διαχρονικές παρατηρήσεις. Οι τιμές του RMSE αναδεικνύουν τις αποκλίσεις σε mm μεταξύ των πραγματικών και των υπολογισμένων τιμών εδαφικής υγρασίας. Συγκεκριμένα, τα πειράματα Γραμμικής Παλινδρόμησης με χρήση του NDVI ως ανεξάρτητη μεταβλητή, έδειξαν μια τιμή RMSE ίση με 7.48, r^2 0.04 και συντελεστή Spearman 0.33. Η Γραμμική Παλινδρόμηση με ανεξάρτητη μεταβλητή τον NDMI είχε RMSE 7.27 και r^2 0.033, ενώ η τιμή του συντελεστή Spearman ήταν 0.004. Στην συνέχεια, η τιμή του RMSE που προέκυψε από την εφαρμογή της Γραμμικής Παλινδρόμησης, με χρήση του MI ως ανεξάρτητη μεταβλητή ήταν 7.22, ενώ οι τιμές του r^2 και του συντελεστή Spearman ήταν 0.043 και 0.155, αντίστοιχα. Το μοντέλο Γραμμικής Παλινδρόμησης με ανεξάρτητη μεταβλητή τις τιμές της οπισθοσκέδασης VV, είχε τιμή RMSE ίση με 8.058, η τιμή του r^2 ήταν 0.043, ενώ ο συντελεστής Spearman ήταν 0.00000006. Στα παρακάτω διαγράμματα, παρουσιάζεται η σύγκριση μεταξύ των υπολογισμένων και των πραγματικών τιμών εδαφικής υγρασίας που προέκυψαν από κάθε μοντέλο.

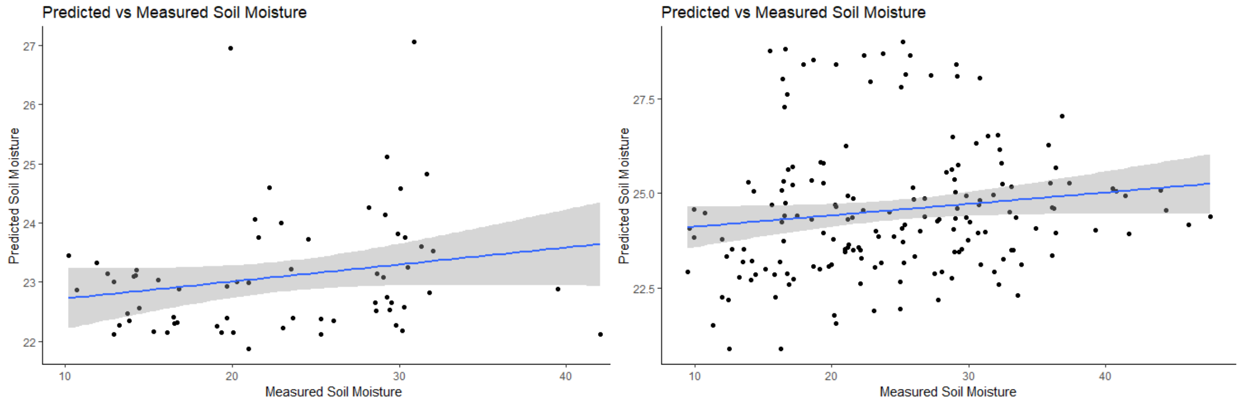

Figure 3: Σύγκριση υπολογισμένων και πραγματικών τιμών υγρασία με ανεξάρτητη μεταβλητή τον NDVI (αριστερά) και τον NDMI (δεξιά) στο Μοντέλο Γραμμικής Παλινδρόμησης (n = 66 παρατηρήσεις των δεδομένων επαλήθευσης).

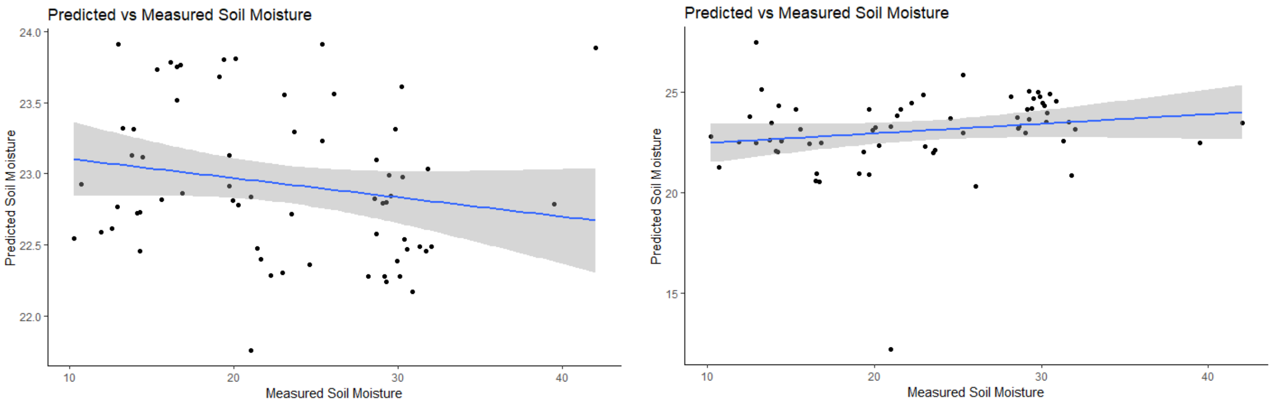

Figure 4: Σύγκριση υπολογισμένων και πραγματικών τιμών υγρασίας με ανεξάρτητη μεταβλητή τον MI (αριστερά) (n = 66 παρατηρήσεις των δεδομένων επαλήθευσης) και την οπισθοσκέδαση VV (δεξιά) (n = 173 παρατηρήσεις των δεδομένων επαλήθευσης) στο Μοντέλο Γραμμικής Παλινδρόμησης.

Όσον αφορά το μοντέλο Πολυωνυμικής Παλινδρόμησης με χρήση του NDVI, το RMSE που προέκυψε ήταν 8.229, το r^2 0.016 και ο συντελεστής Spearman 0.099. Το RMSE του αντίστοιχου μοντέλου με ανεξάρτητη μεταβλητή τον NDMI ήταν 7.646, ενώ το r^2 και ο συντελεστής Spearman, ήταν 0.02 και 0.012, αντίστοιχα. Η χρήση του MI ως ανεξάρτητη μεταβλητή του μοντέλου είχε ως αποτέλεσμα το RMSE να είναι 7.273, το r^2 0.038 και ο συντελεστής Spearman 0.00027. Τέλος, το μοντέλο Πολυωνυμικής Παλινδρόμησης με χρήση τως τιμών οπισθοσκέδασης VV ώς ανεξάρτητη μεταβλητή, είχε ως αποτέλεσμα τιμή RMSE ίση με 8.058, r^2 0.042 και συντελεστή Spearman με τιμή 0.00000000000000022. Τα παρακάτω διαγράμματα απεικονίζουν την σύγκριση μεταξύ των υπολογισμένων και των πραγματικών τιμών εδαφικής υγρασίας που προέκυψαν από κάθε μοντέλο Πολυωνυμικής Παλινδρόμησης.

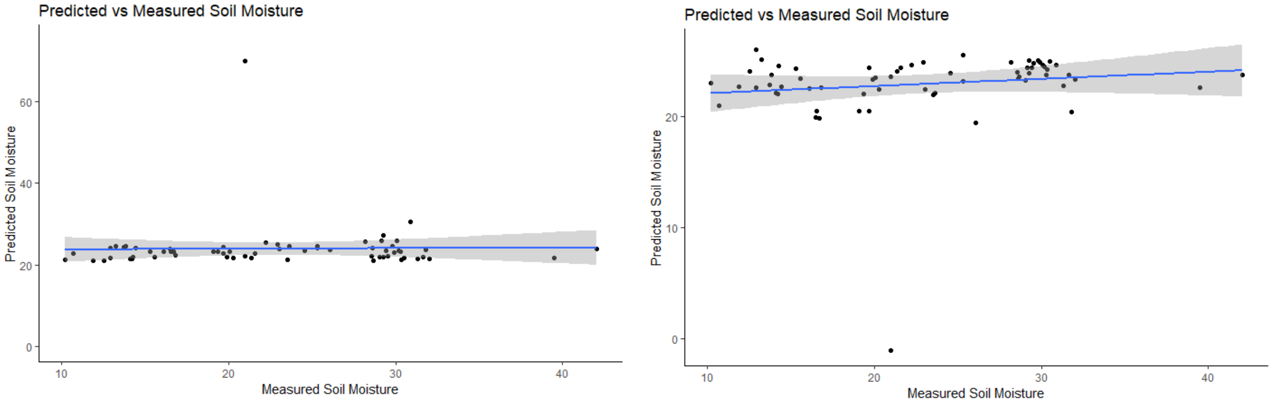

Figure 5: Σύγκριση υπολογισμένων και πραγματικών τιμών υγρασίας με ανεξάρτητη μεταβλητή τον NDVI (αριστερά) και του NDMI (δεξιά) στο Μοντέλο Πολυωνυμικής Παλινδρόμησης (n = 66 παρατηρήσεις των δεδομένων επαλήθευσης).

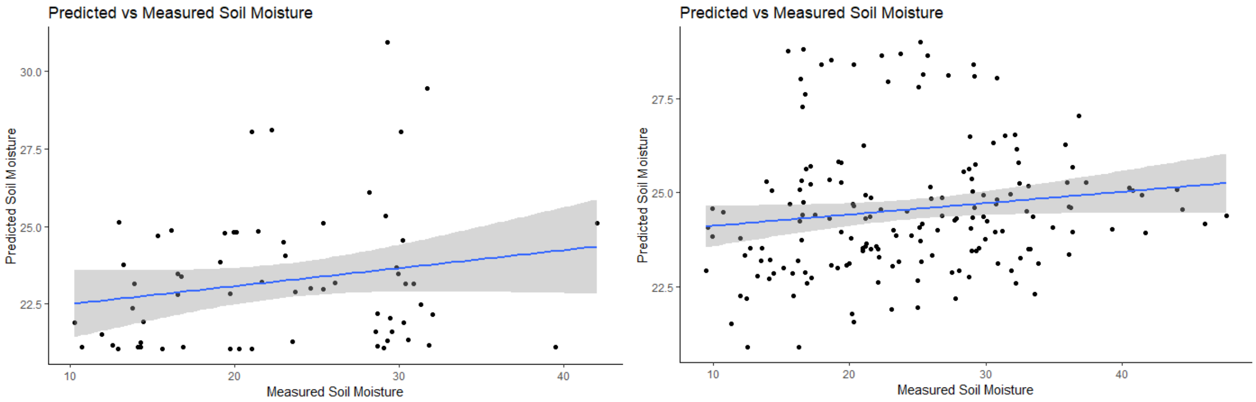

Figure 6: Σύγκριση υπολογισμένων και πραγματικών τιμών υγρασίας με ανεξάρτητη μεταβλητή τον MI (αριστερά) (n = 66 παρατηρήσεις των δεδομένων επαλήθευσης) και την οπισθοσκέδαση VV (δεξιά) (n = 173 παρατηρήσεις των δεδομένων επαλήθευσης) στο Μοντέλο Πολυωνυμικής Παλινδρόμησης.

Τα αποτελέσματα της εφαρμογής του Γενικευμένου Προσθετικού Μοντέλου με χρήση του NDVI ως ανεξάρτητη μεταβλητή είχαν αποτέλεσμα τιμή RMSE 7.441 και r^2 0.03 ενώ οι τιμές του RMSE και r^2 με χρήση του NDMI ως ανεξάρτητη μεταβλητή ήταν 7.268 και 0.033 αντίστοιχα. Η χρήση του MI ως ανεξάρτητη μεταβλητή στο Γενικευμένο Προσθετικό Μοντέλο είχε τιμή RMSE 8.985116 και r^2 0.085. Τέλος, το RMSE που προέκυψε από την εφαρμογή του παραπάνω μοντέλου με χρήση της Οπισθοσκέδασης VV ήταν 7.79 ενώ το r^2 ήταν 0.12. Η σύγκριση μεταξύ των υπολογισμένων και των πραγματικών τιμών εδαφικής υγρασίας φαίνεται στα παρακάτω διαγράμματα.

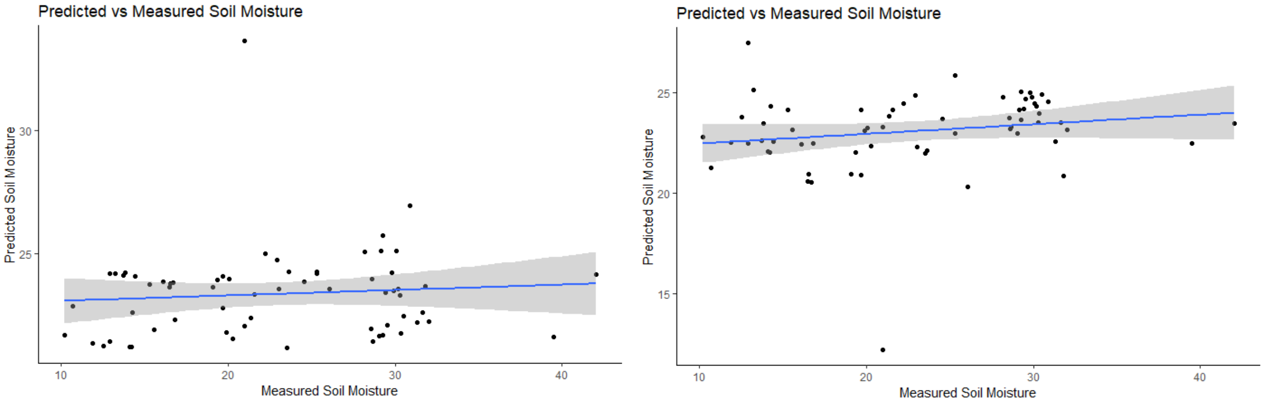

Figure 8: Σύγκριση υπολογισμένων και πραγματικών τιμών υγρασίας με ανεξάρτητη μεταβλητή τον NDVI (αριστερά) και του NDMI (δεξιά) στο Γενικευμένο Προσθετικό Μοντέλο (n = 66 παρατηρήσεις των δεδομένων επαλήθευσης).

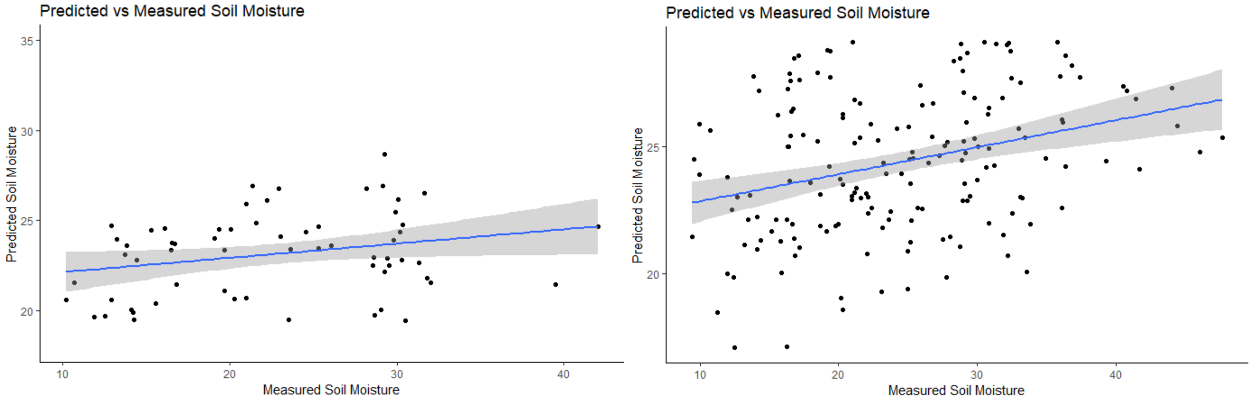

Figure 7: Σύγκριση υπολογισμένων και πραγματικών τιμών υγρασίας με ανεξάρτητη μεταβλητή τον MI (αριστερά) (n = 66 παρατηρήσεις των δεδομένων επαλήθευσης) και την οπισθοσκέδαση VV (δεξιά) (n = 173 παρατηρήσεις των δεδομένων επαλήθευσης) στο Γενικευμένο Προσθετικό Μοντέλο.

Το τελευταίο μοντέλο που υλοποιήθηκε ήταν αυτό των Τεχνητών Νευρωνικών Δικτύων, με χρήση του NDVI και των τιμών οπισθοσκέδασης VV ως ανεξάρτητες μεταβλητές, όπου η τιμή του RMSE διαμορφώθηκε σε 6.204. Στο παρακάτω διάγραμμα φαίνεται η σύγκριση των υπολογισμένων και των πραγματικών μετρήσεων εδαφικής υγρασίας.

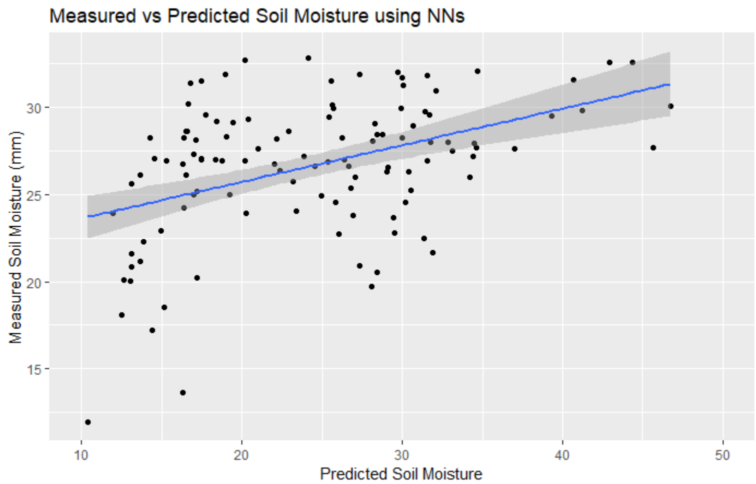

Figure 9: Σύγκριση υπολογισμένων και πραγματικών τιμών υγρασίας με ανεξάρτητες μεταβλητές τον NDVI και τις τιμές οπισθοσκέδασης VV στο Μοντέλο Τεχνητών Νευρωνικών Δικτύων (n = 114 παρατηρήσεις).

Στον παρακάτω πίνακα, συνοψίζονται τα αποτελέσματα όλων των μεθόδων που εφαρμόστηκαν στην παρούσα έρευνα.

Table 1: Σύνοψη των αποτελεσμάτων των εφαρμοσμένων μοντέλων

Γραμμική Παλινδρόμηση			
Ανεξάρτητη Μεταβλητή	**RMSE**	**r^2**	**p-value**
NDVI	7.478	0.040	0.330
NDMI	7.268	0.033	0.004
MI	7.222	0.043	0.155
Οπισθοσκέδαση VV	8.058	0.043	0.00000006
Πολυωνυμική Παλινδρόμηση			
NDVI	8.229	0.016	0.099
NDMI	7.646	0.020	0.012
MI	7.272	0.038	0.00027
Οπισθοσκέδαση VV	8.058	0.042	0.00000000000000022
Γενικευμένα Προσθετικά Μοντέλα			
NDVI	7.441	0.030	-
NDMI	7.268	0.033	-
MI	8.985	0.085	-
Οπισθοσκέδαση VV	7.789	0.120	-
Τεχνητά Νευρωνικά Δίκτυα			

NDVI + Οπισθοσκέδαση VV	6.204		

Σύμφωνα με τα παραπάνω αποτελέσματα, τα συμπεράσματα που προκύπτουν είναι ότι καμία από τις πειραματικές συσχετίσεις που πραγματοποιήθηκαν δεν παρήγαγε αρκετά ικανοποιητικά αποτελέσματα. Παρατηρήθηκε όμως ότι κατά τον υπολογισμό των μοντέλων Γραμμικής Παλινδρόμησης, το ακριβέστερο μοντέλο παρήχθη με την χρήση των τιμών Οπισθοσκέδασης VV ως ανεξάρτητη μεταβλητή αφού ο συντελεστής Spearman ήταν ο χαμηλότερος και το r^2 υψηλότερο, σε σχέση με τα υπόλοιπα μοντέλα που παρήχθησαν μέσω της ίδιας μεθόδου. Παρόλα αυτά και τα αποτελέσματα του δείκτη NDMI ήταν επίσης ικανοποιητικά σε σχέση με αυτά των δεικτών NDVI και MI. Όσον αφορά τα αποτελέσματα της εφαρμογής των Μοντέλων Πολυωνυμικής Παλινδρόμησης, οι τιμές οπισθοσκέδασης VV καθώς και ο δείκτης MI ως ανεξάρτητες μεταβλητές, ανέδειξαν τιμές RMSE που φανέρωναν μέσες αποκλίσεις κατά 8.058 mm (μέγεθος δείγματος, n=865) και 7.273 mm (μέγεθος δείγματος, n=328), αντίστοιχα, μεταξύ των πραγματικών και των υπολογισμένων τιμών εδαφικής υγρασίας, και τιμές r^2 ίσες με 0.042 και 0.038, αντίστοιχα. Ιδιαίτερο ενδιαφέρον είχε και ο συντελεστής Spearman των δυο παραπάνω μοντέλων, αφού ήταν 0.00000000000000022 στο μοντέλο με τις τιμές οπισθοσκέδασης VV και 0.00027 στο μοντέλο όπου χρησιμοποιήθηκε ο δείκτης MI. Το ακριβέστερο μοντέλο που προέκυψε κατά την εφαρμογή των Γενικευμένων Προσθετικών Μοντέλων ήταν το μοντέλο κατά το οποίο ως ανεξάρτητη μεταβλητή χρησιμοποιήθηκαν οι τιμές οπισθοσκέδασης VV, με RMSE που αναδείκνυε ότι η μέση απόκλιση μεταξύ των πραγματικών και των εκτιμώμενων τιμών υγρασίας ήταν +/-7.79 mm και r^2 ίσο με 0.12 (μέγεθος δείγματος, n=865).

Όσον αφορά τα συμπεράσματα που προκύπτουν αναφορικά με την ικανότητα κάθε μεταβλητής να συμβάλει στην εκτίμηση της εδαφικής υγρασίας, παρατηρήθηκε ότι η χρήση των τιμών οπισθοσκέδασης VV έδωσε τα καλύτερα αποτελέσματα σχεδόν σε κάθε τύπο μοντέλου. Από την άλλη πλευρά, τα λιγότερο επιθυμητά αποτελέσματα παρατηρήθηκαν κατά την χρήση του NDVI ως ανεξάρτητη μεταβλητή στα μοντέλα. Ο NDMI φάνηκε να αποδίδει καλύτερα στο μοντέλο της Γραμμικής Παλινδρόμησης ενώ τα αποτελέσματα του MI ήταν αρκετά ικανοποιητικά κατά την εφαρμογή του μοντέλου Πολυωνυμικής Παλινδρόμησης αλλά και των Γενικευμένων Προσθετικών Μοντέλων. Παρόλα αυτά το RMSE του τελευταίου ήταν αρκετά υψηλό σε σχέση με τα υπόλοιπα μοντέλα φανερώνοντας μεγαλύτερες αποκλίσεις μεταξύ των πραγματικών και των εκτιμώμενων τιμών εδαφικής υγρασίας. Τέλος η χρήση των Τεχνητών Νευρωνικών Δικτύων έδωσε τα πιο ικανοποιητικά αποτελέσματα σε σχέση με τις υπόλοιπες μεθόδους, με την χαμηλότερη τιμή RMSE, αναδεικνύωντας μια μέση απόκλιση της τάξεως των +/-6.204 mm μεταξύ των πραγματικών και των υπολογισμένων τιμών εδαφικής υγρασίας (μέγεθος δείγματος, n=114).

1 INTRODUCTION

1.1 SOIL MOISTURE

Soil moisture is an important variable in earth system dynamics (Famiglietti et al., 1998) and it can be described as the amount of water that is stored within the pore spaces in between soil aggregates (inter-aggregate pore space), and within soil aggregates (intra-aggregate pore space). The soil moisture content is the percentage of moisture contained in a sample of soil at a given time, ranging from 0 (completely dry) to the value of the soil's porosity at saturation (completely saturated). It is mainly regulated by the precipitation, the potential evaporation, the temperature and the soil characteristics and is highly variable in space and time (Shouse et al., 1995; Grayson et al., 2002; Zhao et al., 2010; Vachaud et al., 1985; Lin, 2006; O'Geen, 2010).

The term surface soil moisture refers to the water that is present in the upper 10 cm of soil while the term root zone soil moisture is used to describe the water that is available to plants, which is considered to be approximately in the upper 200 cm of soil (Famiglietti et al., 1998; Zhao et al., 2012).

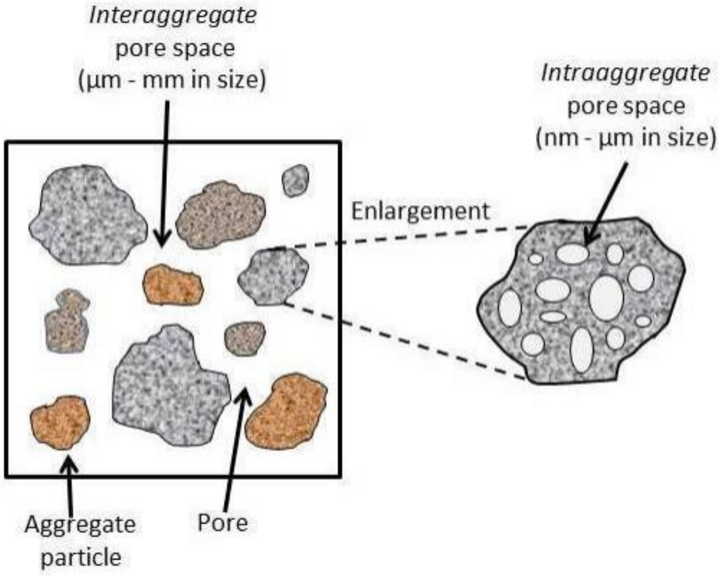

Figure 10: Pore spaces of soil (Source: https://www.jove.com)

Soil moisture is considered a crucial factor for the health and growth of crops and the efficiency of plants (Wang & Qu, 2009) as it serves as a solvent and carrier of nutrients while being essential for photosynthesis. Soil moisture is observed as the water above the water table, whereas the water observed above the water table is known as ground water.

Soil moisture can be expressed as (Sharma, 2007):

- gravimetric moisture which is the mass of water/mass of solid material:

$$Soil\ Water = \frac{weight\ of\ wet\ soil\ (g) - \ weight\ of\ dry\ soil\ (g)}{weight\ of\ dry\ soil\ (g)}$$

$$Gravimetric\ Soil\ Moisture(\theta_m) = \frac{mass\ of\ water}{mass\ of\ dry\ soil}$$
$$= \frac{mass\ of\ wet\ soil - mass\ of\ dry\ soil}{mass\ of\ dry\ soil}$$

- as volumetric which is defined as the volume of soil/total porosity:

$$Volumetric\ Soil\ Moisture\ (\theta_v) = \frac{volume\ of\ water}{volume\ of\ soil} = \frac{(\frac{mass\ of\ water}{density\ of\ water})}{volume\ of\ soil}$$

The process where the water is entering the soil from sources such as rainfall, is called infiltration and it is mainly caused by the gravity. Permeability describes the ease of soil to transmit water and air while porosity describes the space between particles. The process of infiltration depends on the porosity of the soil.

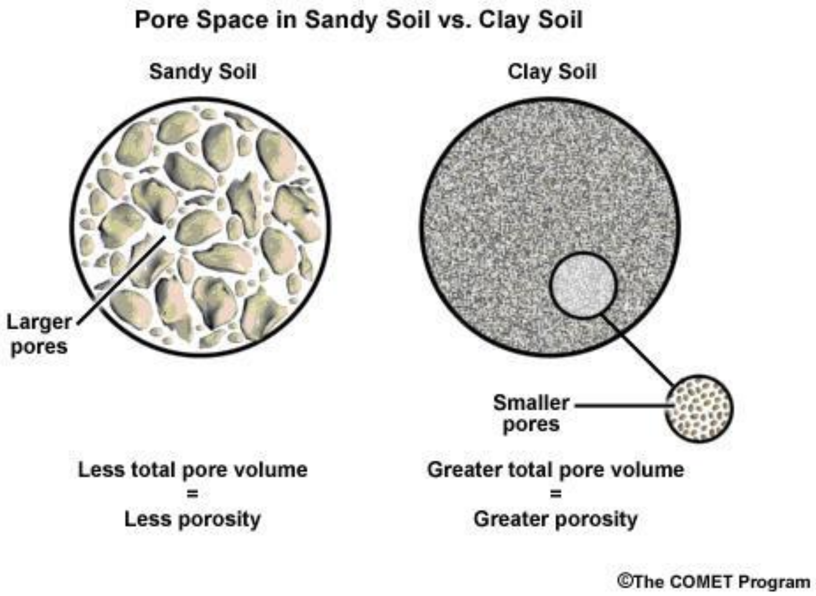

Figure 11: Comparison of the porosity of sandy soil and clay soil

The accumulation of moisture in the soil can be classified in three levels: saturation, field capacity and permanent wilting point. Saturation refers to the condition in which all the spaces between soil particles are completely filled with water which is slowly transmitted to the lower levels of soil with downward movements. When the excess water is drained, the downward movements have decreased and the capillary properties of water overcome the gravitational dynamics, the soil pores are filled with both air and water. This stage is ideal for plant growth. The wilting point is described as the minimum amount of soil moisture that is required for the plants' root to absorb water and not to wilt. In case the soil moisture content becomes lower than the wilting point, then the plants wilt irreversibly due to the fact that the capillary properties of water outmatch the absorption of water by the plants.

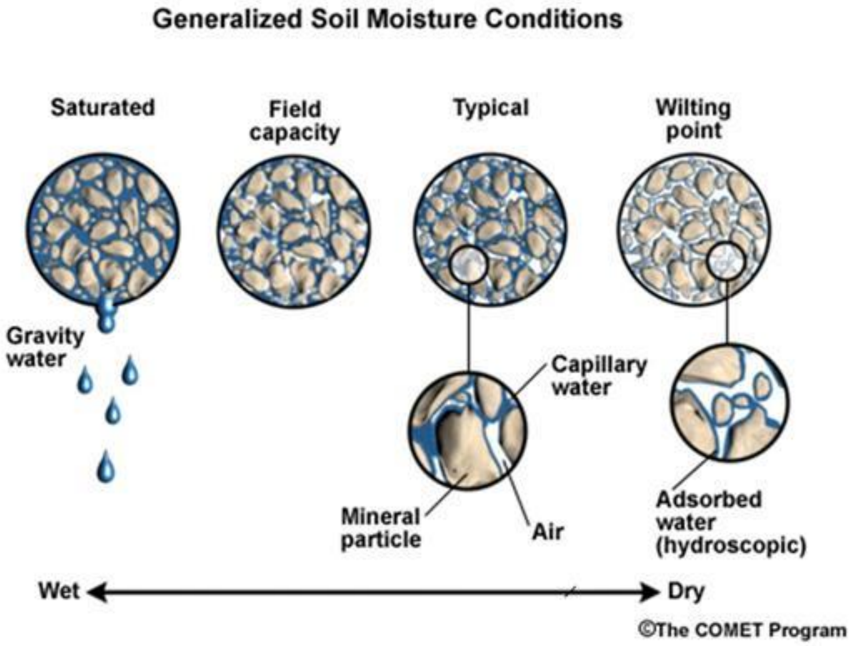

Figure 12: Soil Moisture Conditions

Soil moisture plays an important role in many sectors such as Hydrology, Biogeography, Geomorphology, Agronomy and Climatology (Legates et al., 2010; Liu, et al., 2011).

Soil moisture, referring to the discrimination between wet and dry condition, is a key information for agricultural management such as optimizing the fertilizer rates, irrigation as well as applying pesticides, herbicides, crop management etc. For this reason, soil moisture mapping is a powerful tool for farmers and has encouraged improvements in soil management practices. (Howard et al., 1992).

Many processes such as surface run-off, mineralisation of organic matter or evapo-transpiration, but also irrigation scheduling or forecast of the onset of drought, cannot be examined without investigating the moisture status of the soil (Akinremi and McGinn, 1996, Woodward et al., 2001).

Soil Moisture is included in the list of Essential Climate Variables (ECV) since 2010, and is considered to play an important role in the characterization of Earth's Climate (GCOS 2010).

The major source of water being added to the soil surface is precipitation, where a part of this water flows down through infiltration, another part is absorbed by plants, in order to perform photosynthesis and grow, and the rest flows as runoff through streams and surface water. (Sharma, 2006). Soil moisture contributes in the plant transpiration as well as in the soil evapotranspiration, which affect the near surface air temperature, the humidity and the atmospheric water vapour. Soil moisture though varies from place to place because of the spatial variability of factors such as meteorological conditions, topography and vegetation cover. (Dente, 2016).

1.2 REMOTE SENSING

1.2.1 ACTIVE AND PASSIVE SENSORS

There is always an interaction between electromagnetic radiation and the targets, such as trees, buildings, soil etc. This interaction can be classified either as reflection, scattering or absorption. As a result, the electromagnetic radiation that is emitted by the Sun, interacts with the atmosphere and the surface of the Earth. Earth observation systems receive the reflected or backscattered radiation from the targets. It is important to mention though that the Earth Observation systems are divided into two categories according to the source of the radiation that is received or reflected by the targets. The Earth Observation systems can be categorized either as active or passive.

The Passive Earth Observation systems measure the reflected radiation which is emitted from a natural source, which is the Sun. These sensors, since they depend on another source of radiation, are able to acquire data only during the day and the part of the spectrum they use is the Visible and Infrared. The reflected radiation power measured by passive sensors depends on the surface roughness, the physical temperature, the surface composition and other physical characteristics of the Earth. Passive Remote Sensing is really similar to how our eyes interpret the world and it is mostly used in applications related to Climate, Ecosystem and Land Use.

On the other hand, the Active sensors measure signals transmitted by the sensor itself which are reflected, scattered or refracted by the Earth's surface or the atmosphere. They use the microwave part of the electromagnetic spectrum and they are capable of acquiring data during day as well as during the night in any occurring weather condition. Active Remote Sensing has a variety of applications related to Meteorology, Topography, Security, Natural disasters etc.

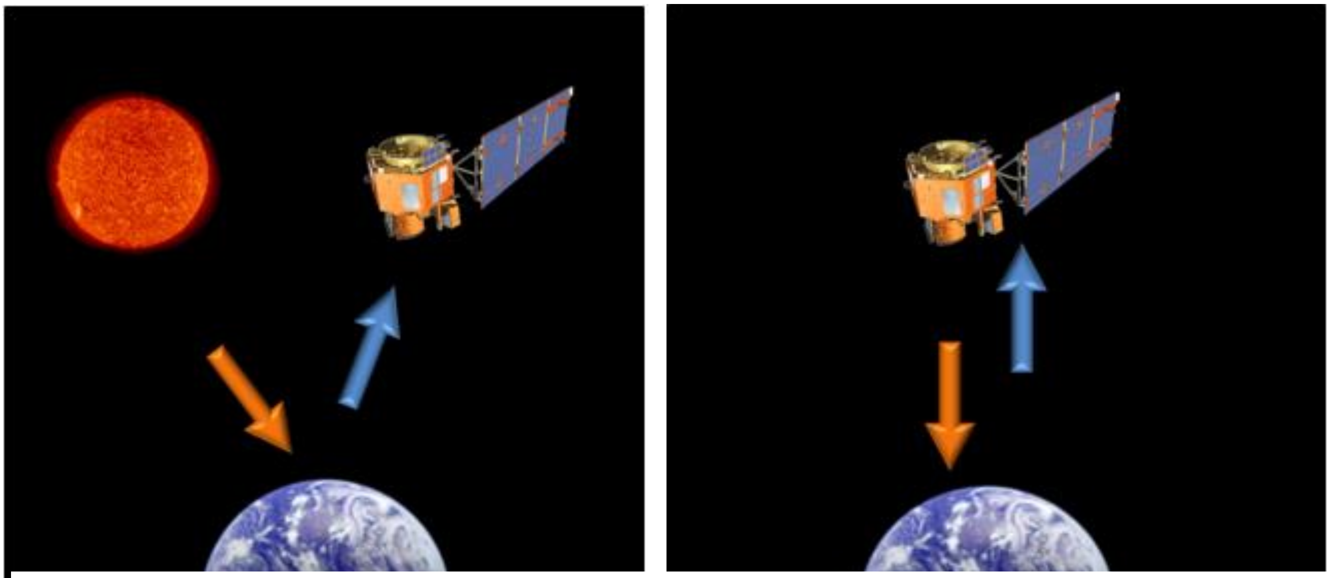

Figure 13: Passive (left) and Active (right) sensors. Source: NASA (www.nasa.gov)

1.2.2 SENTINEL 1

One of the datasets that was used in the current study was acquired from the Sentinel 1 mission which is the European Radar Observatory for the Copernicus joint initiative of the European Commission (EC) and the European Space Agency (ESA). Copernicus is a European initiative responsible for the implementation of services related with security and environment. The Sentinel 1 mission is comprised of C-band imaging systems which operate in four modes and offer products of different resolutions and coverage, short revisit times and dual polarization capabilities (HH+HV, VV+VH), which is useful for land cover classification and sea-ice applications. The Sentinel 1 mission is composed of a two-satellite constellation, Sentinel 1A, which was launched on the 3rd of April in 2014, and Sentinel 1B which was launched on the 22nd of April in 2016, sharing the same orbital plane and they are equipped with a C-band Synthetic Aperture Radar instrument, operating at a center frequency of 5.405 GHz. It includes a right-looking active phased array antenna providing fast scanning in elevation and azimuth. As mentioned in the previous chapters, Synthetic Aperture Radar (SAR) is not affected by cloud cover or lack of illumination and is also capable of acquiring data during the day as well as during the night.

Figure 14: Sentinel-1 spacecraft (image credit: ESA, TAS-I)

Each Sentinel 1 spacecraft is a three-axis, stabilised satellite, characterised by sun, star, gyro and magnetic field sensors, a set of four reaction wheels dedicated to orbit and attitude control and three torque rods as actuators to provide steering capabilities on each axis. Each satellite has a total mass of approximately 2300kg at launch and is equipped with two solar array wings capable of producing 5900 W (at end of life) to be stored in a modular battery. Highly accurate pointing knowledge (better than 0.004°) on each axis, high pointing accuracy (about 0.01° on each axis) and real-time orbit determination together with a dedicated propulsion system for precise orbit control are provided by the PRIMA (Piattaforma Italiana Multi Applicativa) bus. Some of Sentinel 1 mission's specifications can be found in the following table.

Table 2: Sentinel 1 Specifications

Parameter	Sentinel-1
Launch date	April 03, 2014 of S1-A April 22, 2016 of S1-B
Orbit type	SSO (Sun-synchronous Orbit) 12 day repeat cycle LTAN = 18:00 hours
Orbital altitude	693 km
Sensor complement	C-SAR (C-band Synthetic Aperture Radar)
Spacecraft mass Spacecraft size Spacecraft power	2300 kg 3.4 m x 1.3 m x 1.3 m 4.8 kW (EOL)
Downlink X-band data rate	520 Mbit/s
TT&C S-band	64 kbit/s uplink 128 kbit/s or 2 Mbit/s downlink
Science data storage	1.4 Tbit (EOL)
Required data quality	BER (Bit Error Rate): < 10^{-9}
Operational autonomy	8 days
Prime contractor	TAS-I (Thales Alenia Space-Italy)
Baseline launcher	Soyuz (Kourou)

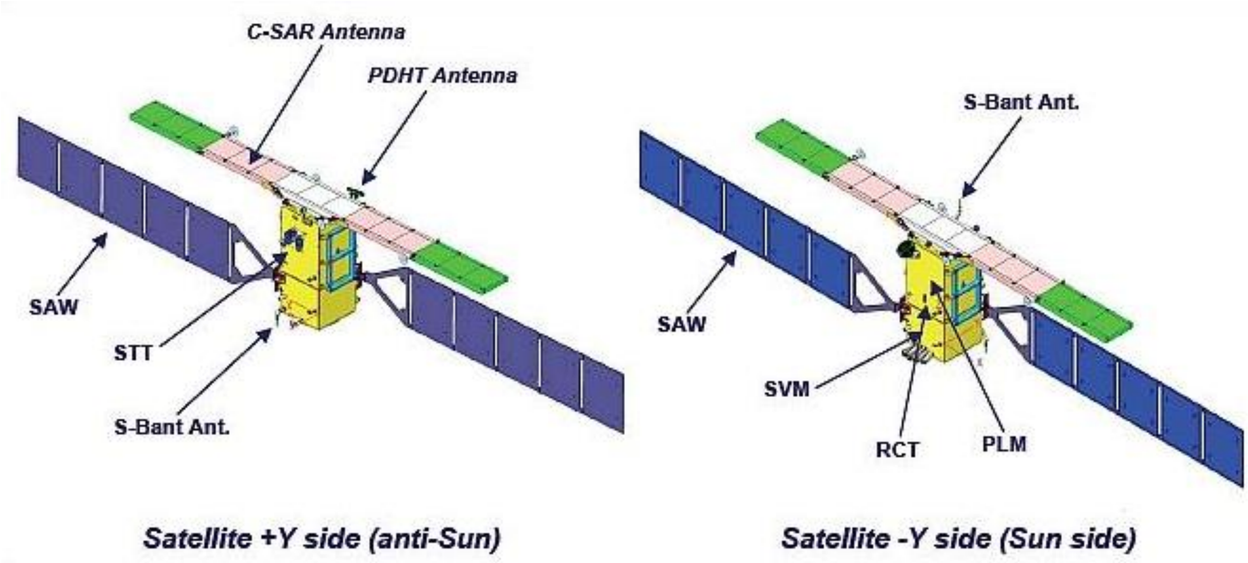

Figure 15: Overview of a Sentinel 1 mission spacecraft. (Source: https://sentinel.esa.int)

The reference orbit is an Earth-fixed orbital tube of a 100m diameter during normal operation.

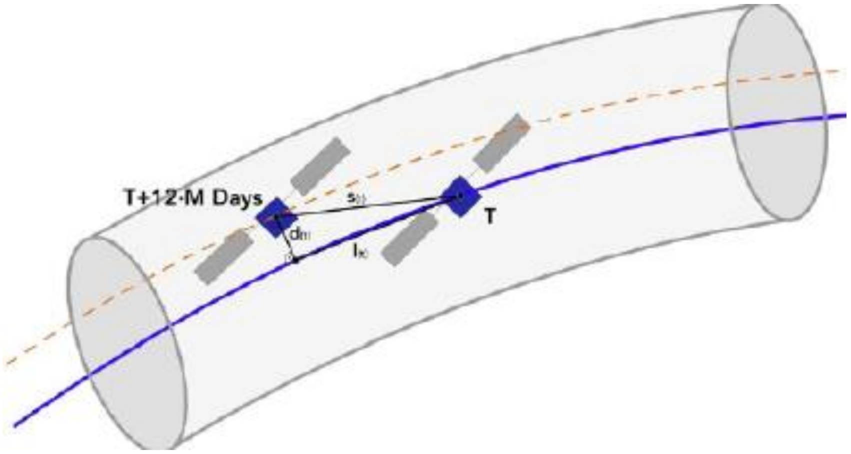

Figure 16: Sentinel 1 Orbit Tube (https://sentinel.esa.int/web/sentinel/missions/sentinel-1/satellite-description/orbit)

Both Sentinel 1A's and Sentinel 1B's orbit is near-polar, sun-synchronous with a 12 day repeat cycle and 175 orbits per cycle for a single satellite and having both satellites operating the repeat cycle is 6 days. This means that each Sentinel 1 satellite is able to map the entire world in 12 days.

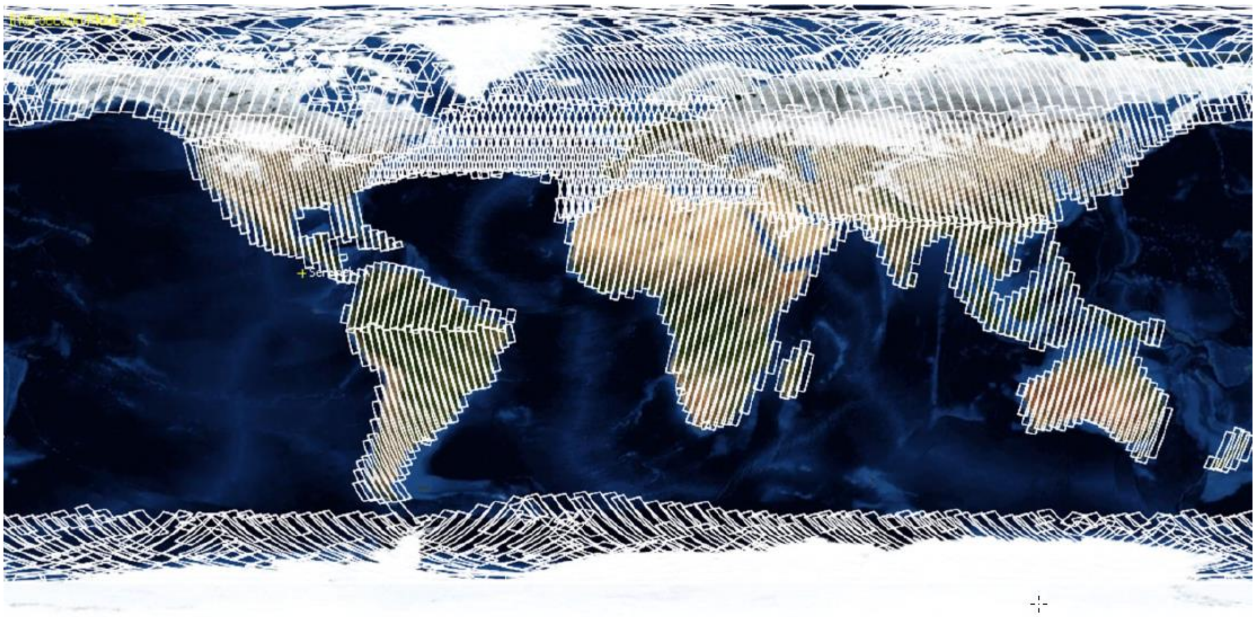

Figure 17: Sentinel 1 Coverage (Source: https://sentinel.esa.int)

They both also share the same orbit plane with a 180° orbital phasing difference. Approximately one hour after the acquisition, radar data are delivered to Copernicus services.

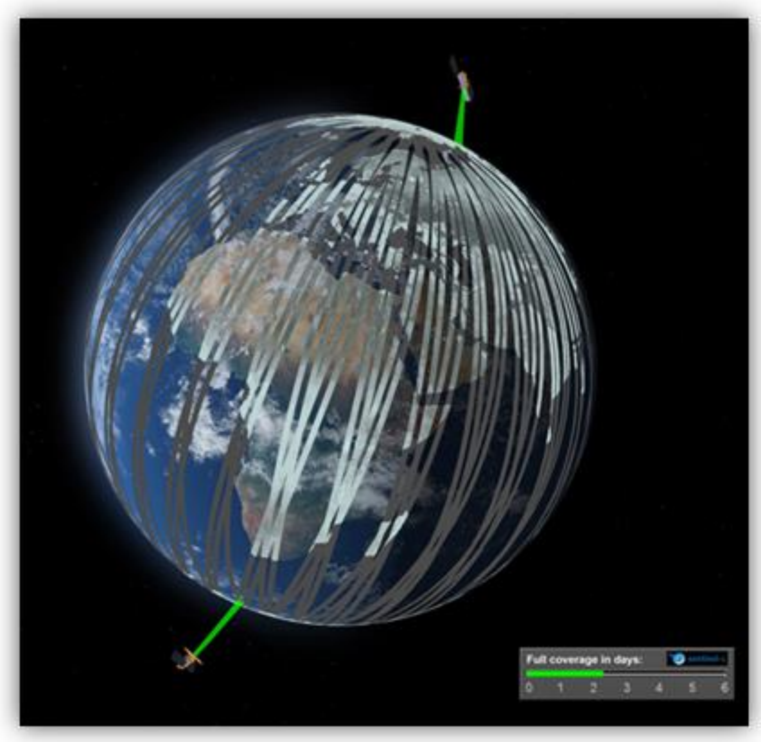

Figure 18: Sentinel 1 Constellation and orbits (Source: https://sentinel.esa.int)

It is important to mention that Sentinel 1 operates in four different imaging modes:

- **Stripmap Mode**, which provides 5m by 5m resolution over a narrow swath of 80 km.
- **Interferometric Wide Swath Mode (IW)**, which combines a large swath of 250 km with a moderate resolution of 5m by 20m and employs the Progressive Scans SAR or TOPSAR technique. This is the default acquisition mode over land.
- **Extra Wide Swath Mode (EW)**, which is similar to the IW mode but with a lower resulting resolution of 20m by 40m. This mode is intended for maritime, ice and polar zone operational services where wide coverage and short revisit times are demanded.
- **Wave Mode**, which results in stripmap imagettes of 20km by 20km, acquired every 100 km with imagettes of the same incidence angle being separated by 200km. This mode is useful for the investigation of the direction, height and wavelength of waves in the oceans.
-

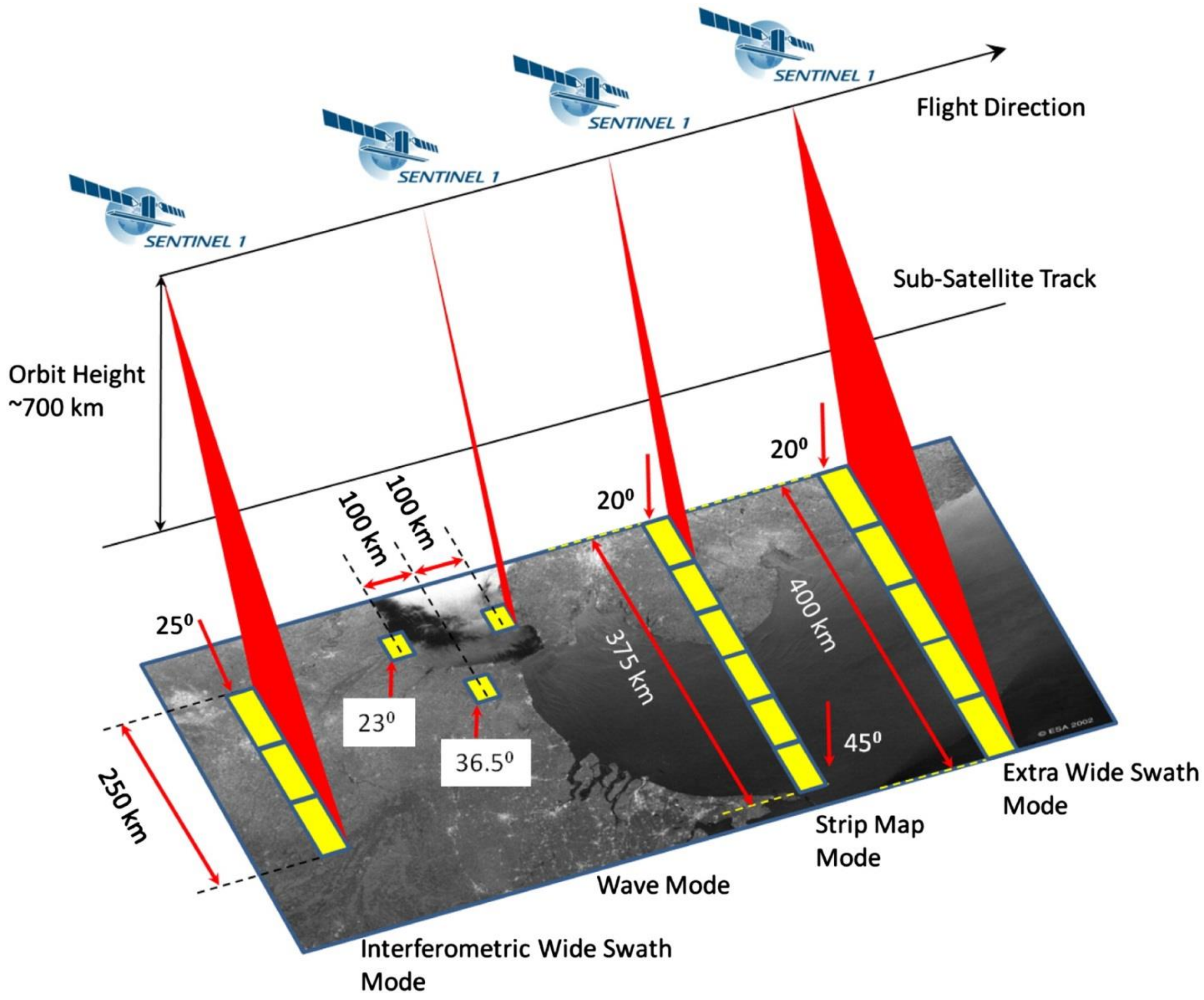

Figure 19: Sentinel 1 Modes (Source: https://sentinel.esa.int)

In the following table, the specifications of each mode can be found.

Table 3: Description of the four Acquisition Modes

Mode	Incidence Angle	Resolution	Swath Width	Polarization (H = Horizontal V = Vertical)
Stripmap	20 - 45	5 x 5 m	80 km	HH+HV, VH+VV, HH, VV
Interferometric Wide swath	29 - 46	5 x 20 m	250 km	HH+HV, VH+VV, HH, VV
Extra Wide swath	19 - 47	20 x 40 m	400 km	HH+HV, VH+VV, HH, VV
Wave	22 - 35 35 - 38	5 x 5 m	20 x 20 km	HH, VV

The format of the Sentinel 1 products is the Sentinel Standard Archive Format for Europe (SAFE) and they can be produced at SAR Level-0, Level-1 SLC, Level-1 GRD, and Level-2 OCN. The processing levels of the produced data can be described briefly as:

- **Level 0** products consist of a sequence of compressed unfocused SAR raw data. For the data to be usable, it will need to be decompressed and processed using a SAR processor.
- **Level 1** products can either be **Single Look Complex (SLC)**, which consist of focused SAR data geo-referenced using orbit and attitude data from the satellite and provided in zero-Doppler slant-range geometry, or **Ground Range Detected (GRD)**, which consist of focused SAR data that has been detected, multi-looked and projected to ground range using an Earth ellipsoid model. There is no phase information in GRD products. The resulting product has approximately square spatial resolution pixels and square pixel spacing with reduced speckle at the cost of worse spatial resolution. GRD products are devided into three kinds of resolution; full, high and medium resolution and the pixel values depict the detected magnitude. In the current study Sentinel 1 Level 1 High Resolution GRD products in Interferometric Wide swath Mode were used. The product characteristics are described in the following table.

Table 4: IW GRD High Resolution product characteristics per beam mode (Source: https://sentinel.esa.int)

Beam ID	IW1	IW2	IW3
Spatial Resolution rg x az m	20.4x22.5	20.3x22.6	20.5x22.6
Pixel spacing rg x az m	10x10	10x10	10x10
Incidence angle º	32.9	38.3	43.1
Equivalent Number of Looks (ENL)	4.4	4.3	4.3
Radiometric resolution	1.7	1.7	1.7
Range look bandwidth MHz	14.1	12.1	10.7
Azimuth look bandwidth Hz	315	301	301
Range Hamming weighting coefficient	0.70	0.73	0.75
Azimuth Hamming weighting coefficient	0.70	0.75	0.75

Table 5: IW GRD High Resolution product characteristics common to all beams (Source: https://sentinel.esa.int)

Product ID	**IW_GRD_HR**
Pixel value	Magnitude detected
Coordinate system	Ground range
Bits per pixel	16
Polarisation options single	(HH or VV) or Dual (HH+HV or VV+VH)
Ground range coverage km	251.8
Absolute location accuracy m (NRT)	7
Number of looks (range x azimuth)	5 x 1
Look overlap (range x azimuth)	0.25 x 0.00

- **Level 2 OCN** products include components for Ocean Swell spectra (OSW), Ocean Wind Fields (OWI) and Surface Radial Velocities (RVL).

(Snoeij, 2009)

1.2.3 LANDSAT 8

The Landsat Program has been providing its user community with medium spatial resolution, multispectral satellite data, on a global basis, since 1972. Landsat data are distributed by the U.S. Geological Survey (USGS), they are available to the public for free and support many land surface change studies. Moreover, Landsat data constitute the longest remote sensing record of Earth’s continental surface.

Landsat 8 was developed as a collaboration between NASA and the U.S. Geological Survey (USGS) and it was launched on the 11th of February, 2013, on an Atlas-V 401 rocket, from Vandenberg Air Force Base, California. Landsat 8 operates in a near-circular, near-polar, Sun-Synchronous orbit with a 16-day repeat cycle with a 705 km altitude at the Equator. There is an 8-day offset between Landsat 7 and Landsat 8 coverage of each Worldwide Reference System-2 (WRS-2) path. Its payload consists of two push-broom instruments; the Operational Land Imager (OLI) and the Thermal Infrared Sensor (TIRS), viewing at-nadir on the Sun-synchronous Worldwide Reference System-2 (WRS-2) orbital path. These sensors provide data of the global landmass at a spatial resolution of 30 meters (visible, NIR, SWIR); 100 meters (thermal); and 15 meters (panchromatic), as well as improved signal-to-noise (SNR) radiometric performance quantized over a 12-bit dynamic range, enabling finer characterization of land cover. OLI and TIRS collect data jointly in order to provide coincident images over the same surface areas, with each scene covering a 190 by 180 km surface area. Furthermore, each Landsat 8 product includes a Quality Assessment band which facilitates the application of per pixel filters.

The Operational Land Imager (OLI) is a push-broom sensor with a four-mirror anastigmatic telescope, collecting data in nine spectral bands, including visible, near infrared and short wave infrared spectral bands. It is equipped with long linear detector arrays with thousands of detectors per spectral band. The data produced by OLI are quantized to 12bits, compared to the 8-bit data of TM and ETM+ sensors and they are collected over a 190 km across-track ground swath. OLI also offers a panchromatic band in addition to two new spectral bands; a shortwave infrared channel (band 9; 1.36-1.38 μm) for cirrus cloud detection and a deep blue visible channel (band 1; 0.435-0.451 μm) for coastal zone observations (USGS).

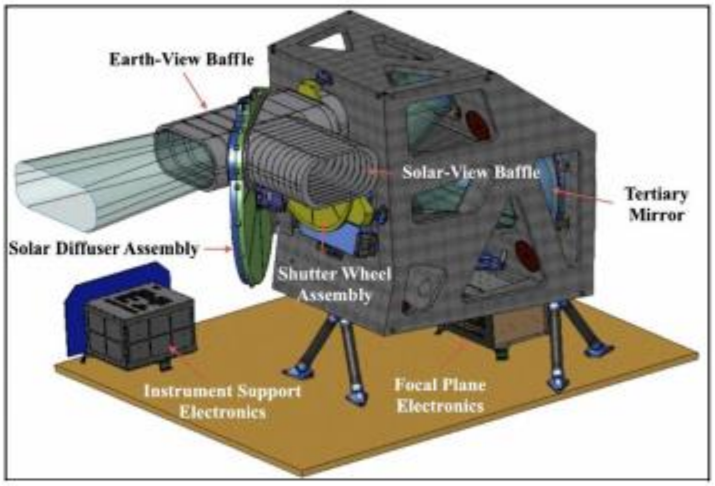

Figure 20: The OLI Instrument (Source: https://landsat.usgs.gov)

The Thermal Infrared Sensor (TIRS) was added to the satellite in order to enable tracking of land and water use. It has a focal plane with long arrays of photosensitive detectors and is able to measure longwave Thermal Infrared (TIR) energy emitted by the Earth's surface, the intensity of which is a function of surface temperature. This instrument is capable of collecting data in two thermal bands, with a 100 m spatial resolution over a 190 km swath, for the wavelength covered by a single band on the previous TM and ETM+ sensors.

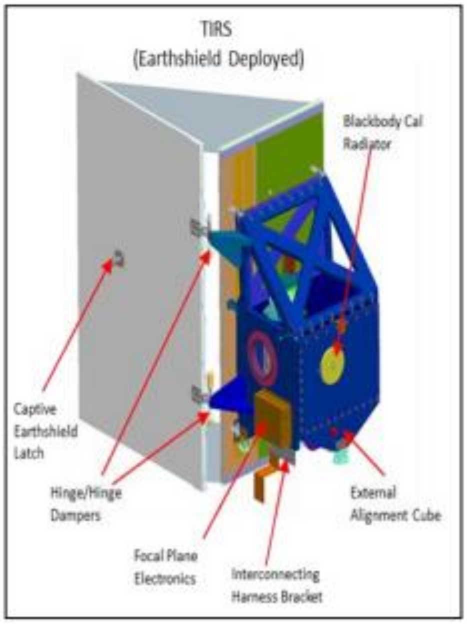

Figure 21: The TIRS Instrument (https://landsat.usgs.gov)

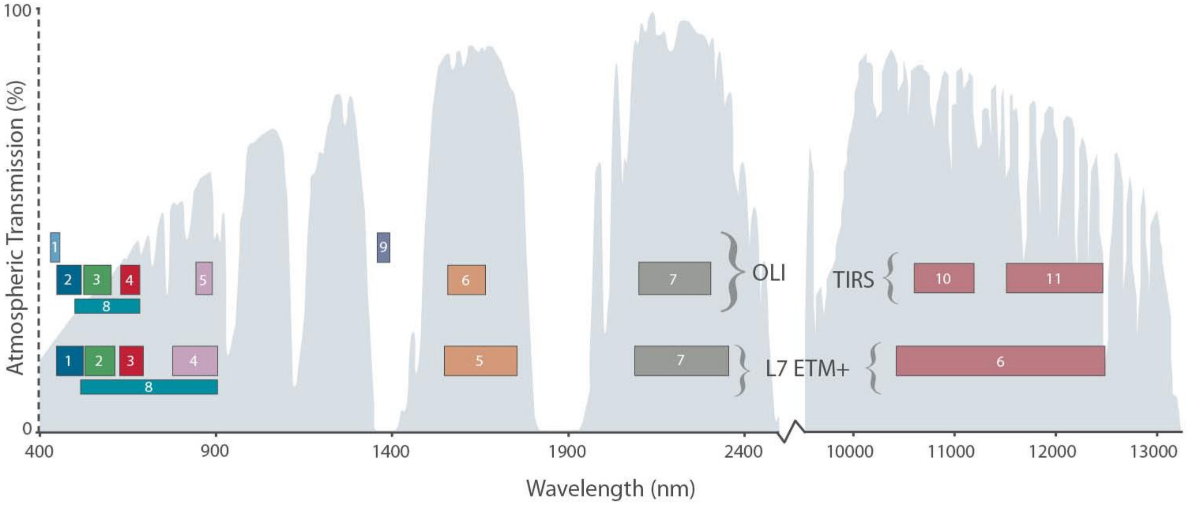

Figure 22: Spectral Bands of Landsat 8 and Landsat 7 (Graphic created by L.Rocchio & J.Barsi., accessed through https://landsat.gsfc.nasa.gov)

Table 6: Description of Landsat 8 spectral bands (created by B. Markham, accessed through https://landsat.gsfc.nasa.gov)

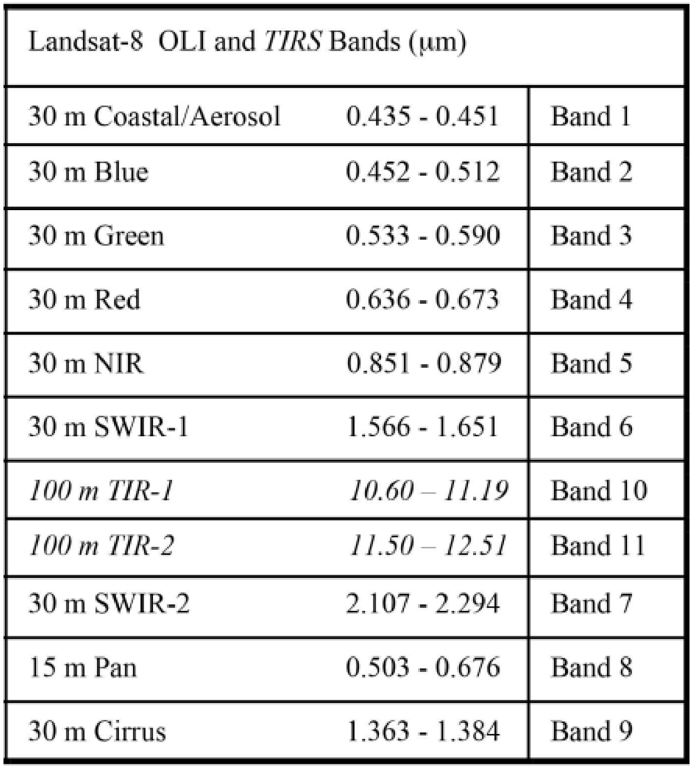

Landsat-8 OLI and *TIRS* Bands (μm)		
30 m Coastal/Aerosol	0.435 - 0.451	Band 1
30 m Blue	0.452 - 0.512	Band 2
30 m Green	0.533 - 0.590	Band 3
30 m Red	0.636 - 0.673	Band 4
30 m NIR	0.851 - 0.879	Band 5
30 m SWIR-1	1.566 - 1.651	Band 6
100 m TIR-1	*10.60 – 11.19*	Band 10
100 m TIR-2	*11.50 – 12.51*	Band 11
30 m SWIR-2	2.107 - 2.294	Band 7
15 m Pan	0.503 - 0.676	Band 8
30 m Cirrus	1.363 - 1.384	Band 9

Landsat 8 data are derived in several processing levels as described briefly below:

Level 1 products are radiometrically and geometrically corrected, free from distortions related to the sensor, satellite or Earth. The Level 1 Images are in units of DNs which can be scaled to spectral radiance or Top Of Atmosphere (TOA) Reflectance.

1.3 LITERATURE REVIEW

During the past years, numerous attempts have been made to estimate soil moisture with the contribution of innovative Remote Sensing techniques.

Wagner et al (1999) investigated the potential of using ERS Scatterometer data for soil moisture monitoring over Ukraine. The algorithm applied required remote sensing data as well as wilting level, field capacity and porosity derived from soil data.

Magagi and Kerr (2001) used NOAA/AVHRR visible and NIR daily reflectance data (in order to obtain the vegetation fractional cover parameter) and ERS-1 Wind Scatterometer (WSC) data in VV polarization. Soil moisture content was retrieved by using empirical models for bare and vegetated soil.

Verstraeten et al (2006) estimated Soil Moisture Content using optical and thermal spectral information from METEOSAT imagery, based on thermal inertia, as well as ERS Scatterometer (for Soil Water Index computation) and EUROFLUX data.

Baup et al. (2007) retrieved Soil Moisture over a semi-arid environment in Mali, by using ENVISAT/ASAR Wide Swath mode products (in HH polarization) and ground data. Correlation and error analysis was conducted.

Zhang et al. (2009) used L1B ENVISAT/ASAR Alternate Polarization mode products (in VV polarization) and In-Situ data for soil moisture retrieval and mapping over LOPEX05 area in China, by applying inversion methods.

Lakhankar et al. (2009) examined the implementation of non-parametric methods to retrieve soil moisture using remote sensing data. In this study two RADARSAT-1 ScanSAR Narrow Mode backscatter products along with one Landsat image for the derivation of NDVI, were used. As long as the training and the validation of the methods are concerned, ESTAR and STATSGO soil classification data were used. The method applied includes the computation of the Grey Level Co-Occurence Matrix (for the extraction of 8 eight textural images: Homogeneity, Contrast, Dissimilarity, Mean, Variance, Entropy, Angular Second Moment, Correlation) and the use of these images as inputs into Multiple Regression, Neural Networks and fuzzy logic algorithms.

Brocca et al. (2011) examined the retrieval of soil moisture using AMSR-E and ASCAT data. Using the AMSR-E data, Land Parameter Retrieval Model (LRPM), standard NASA algorithm and Polarization Ratio Index were applied. ASCAT data were used in the application of the TU Wien change detection algorithm. Also, algorithms based on Linear Regression Correction and Cumulative Density Function (CDF) were employed.

Gherboudj et al. (2011) estimated soil moisture by applying semi-empirical backscatter models using RADARSAT-2 SAR data over agricultural fields in Canada.

Van der Velde et al. (2012) proposed soil moisture retrieval using ENVISAT/ASAR Wide Swath (WS) mode products in VV polarization and In-Situ data. The retrieval method was based on the IEM surface scattering model.

Ahmad, Runping and Jing (2012) used MODIS and In-Situ data for soil moisture retrieval in a region of China. More specifically MOD11A2 (Land Surface Temperature) and MOD13A2 (NDVI) products were used in order to calculate the TDVI which was used in the equation for Relative Soil Moisture retrieval. Ground data of soil moisture from 98 stations were also used. These data were divided into two groups: data from 75 stations were used for the development of the model and data from 23 stations were used for the validation.

Kolassa et al. (2016) conducted analysis of the daily retrieval of soil moisture by the fusion of active and passive microwave data, acquired from ASCAT Scatterometer and AMSR-E Radiometer, using Neural Networks.

El Hajj et al. (2016) developed an inversion approach to estimate surface soil moisture over irrigated grassland areas in Southern France, using time-series of TerraSAR-X, Cosmo-SkyMed, SPOT 4/5 and Landsat 7/8. Neural Network techniques were applied.

Gilewski et al. (2017) retrieved soil moisture using VH/VV Sentinel-1 backscatter and In-Situ data. Multiple Linear Regression Model (MRM) was applied.

Wang et al. (2017) investigated three model-based polarimetric decompositions (Freeman-Durden, Hajnsek and An) for soil moisture retrieval over agricultural fields covered by several crops. UAVSAR polarimetric Multi-look product and SMAPVEX12 ground campaign data were used.

Kolassa et al. (2017) used Neural Networks to estimate soil moisture using SMAP Brightness Temperature products and GEOS-5 Catchment land surface Model soil moisture field. In addition, SMAP L2, AMSR2 and ASCAT Soil Moisture products, In-Situ SMAP core validation sites and International Soil Moisture Network (ISMN) data were used for validation.

Santi et al. (2018) estimated soil moisture over Italy using Ground Range Detected (GRD) Sentinel-1 Images in Interferometric Wide Swath (IW) mode, SMAP L1B Radiometer Half-Orbit Time-Ordered Brightness Temperature and AMSR2 L1B V2 Multi-frequency products, as well as SMEX02 In-Situ data. Disaggregated microwave data, generated using Smoothing Filter based Intensity Modulation, were implemented into an Artificial Neural Network.

1.4 STUDY AREA

The study area includes the plain of Arta and the Amvrakikos Wetlands National Park, which are located at the Southern part of the municipality of Arta in the region of Epirus.

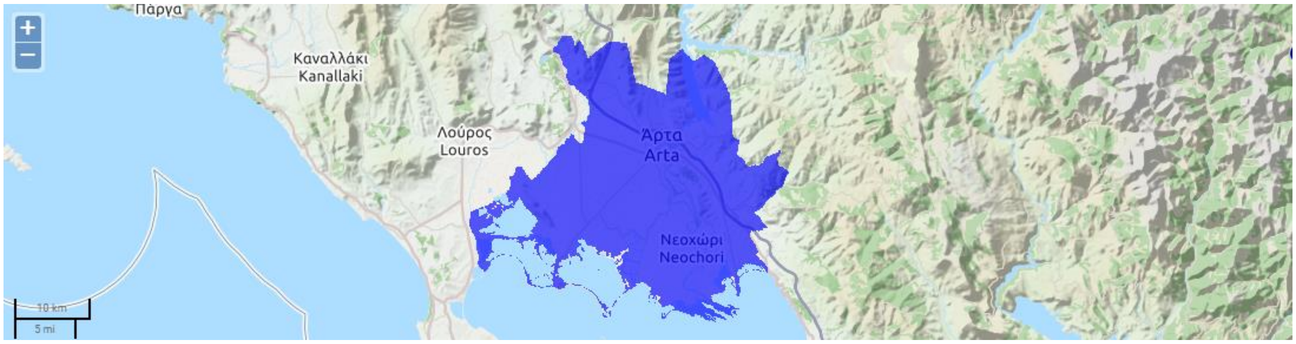

Figure 23: The study area including the Arta plain and the Amvrakikos Wetlands National Park. (Source: http://arta.irrigation-management.eu/)

The region of Epirus is located at the North-West part of Greece. Epirus has a total area of 9.203km^2 of which the 14% corresponds to agricultural land and a population of 353.820 people (Malamos et al., 2015).

The plain of Arta is located at the southest part of Epirus and is part of the Louros and Aracthos hydrological basins. The plain was created by the silts of the rivers Louros and Aracthos and is considered the largest plain of the region with an area of 45.329 ha and it intersects with the Amvrakikos Wetlands National Park.

The plain is almost flat with slight slopes between 0% and 25% and its altitude lies between 0m and 100m. The water table of area is very shallow and its climate is of Mediterranean type with rainy moderate winters and hot summers. (Tsirogiannis et al., 2015)

As long as the Amvrakikos gulf is concerned, it occupies an area of 405 km^2, is a marine lake connected to the Ionian sea through a narrow and shallow channel whose form is the result of both natural and man-made factors. It has an average depth of 26m with a maximum depth of 65m. The submerging of land was caused by the intense tectonic activity of Pleiocene and lower Pleistocene periods, but it was filled up with sediments carried by Aracthos and Louros rivers while water from the Ionian sea flood into the land cavity due to the graduate increase of the sea level during the Holocene. These processes gave the gulf its present shape. It is also important to mention that the Amvrakikos gulf is protected by Ramsar Convention (Ramsar, 2014) (Tsirogiannis et al., 2015).

The Amvrakikos Wetlands are located at the north coast of the gulf, is adjacent to Arta's plain and consists of a total area of 20.000 ha (Tsirogiannis et al., 2015). The wetlands consist of a complex landscape with hills, peninsulas and lagoons as well as rich vegetation including crops, oak woods, cliff forests and pasture lands. Also many rare and endangered species can be found in this area (Rigas et al., 2003).

The Amvrakikos Wetlands National Park includes a big part of Arta's plain and the wetlands and is one of Europe's most important protected areas being a part of the EU NATURA 2000 network (EEA, 2014; EKBY, 2014). The park is managed by Amvrakikos Wetlands Management Body (AWMD, 2014) (Tsirogiannis et al., 2015).

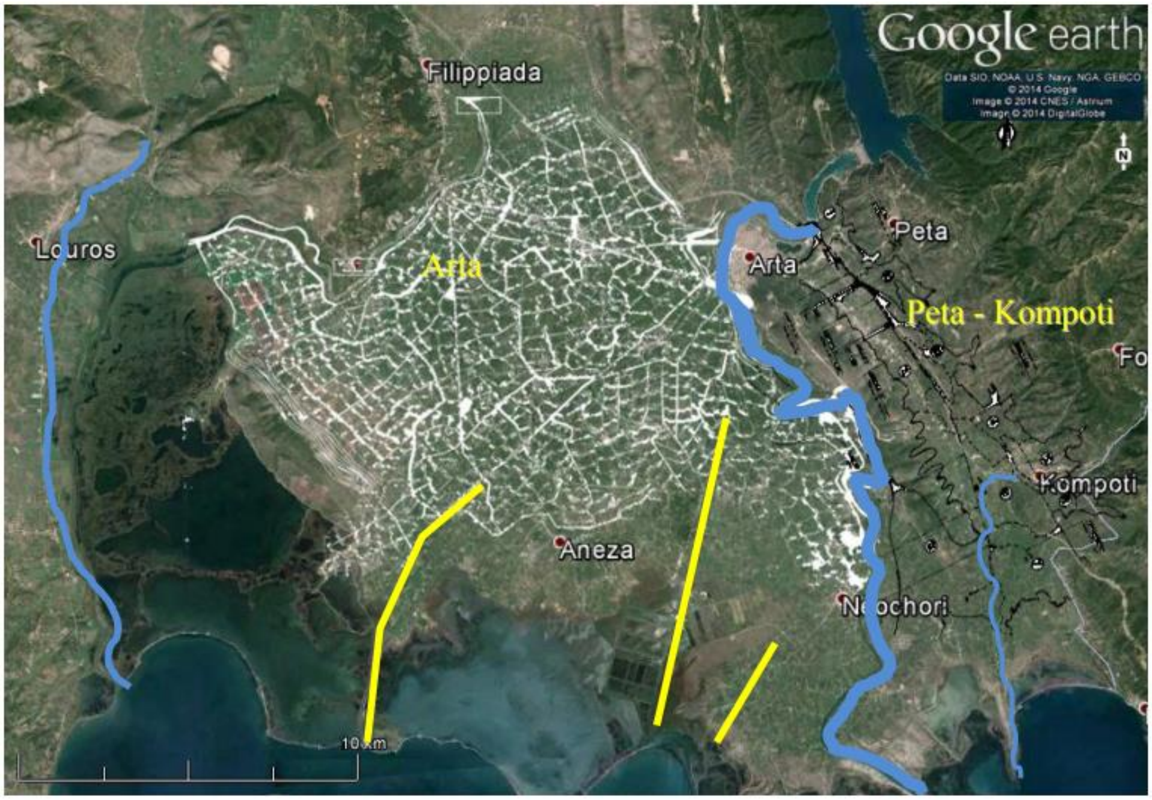

Figure 24: The irrigation scheme of the plain of Arta (white lines;Arta (west part); black lines; Peta-Kompoti (east part)), the 3 rivers (blue lines; from left to right: Louros, Aracthos and Vovos) and the 3 main drainage canals of the plain (yellow lines; from left to right: Salaoras (DC1), Fidocastrou (DC2) and Neochoriou (DC3)) (Source: Tsirogiannis et al. 2015)

2 GEOSPATIAL DATA

In order to train the Artificial Neural Network, real measurements of Soil Moisture were needed to be used as output data. For this purpose, In-Situ data of Soil Moisture were derived from six stations through the Enhydris database. Enhydris is a free software, available under the GNU Affero General Public License, and it can run on UNIX or Windows. It is written in Python/Django and includes a database in which hydrological and meteorological time series are stored and managed. The time series can be accessed through a web interface with tables, graphs and mapping capabilities and they can also be downloaded in plain text format or they can be directly loaded to Hydrognomon. Hydrognomon is a free tool for analysis and processing of meteorological time series. The Enhydris database web interface also includes a map that provides information about the location of each station, together with the identification numbers, water basin, water division, owner and type of the meteorological stations. The database can be accessed in http://system.irrigation-management.eu or https://enhydris.readthedocs.org through a webservice API. Enhydris is being used by openmeteo.org, Hydrological Observatory of Athens, Hydroscope, the Athens Water Supply Company, and WQ DREAMS (Christofides et al., 2011a; Christofides et al., 2011b; Malamos et al., 2015).

The selected In-Situ data were measured from six meteorological and hydrological stations which were located in Agios Spyridonas, Kampi, Kommeno, Kompoti, the Technological Educational Institute of Epirus in Kostakii and the TOEB Lourou. A more detailed description of the stations can be found in the following table.

Table 7: Description of In-situ Measurements' stations (Source: http://openmeteo.org)

ID	Name	Water Department	Prefecture	Coordinates	Altitude	Instrument	Type	Responsibility
1402	**TEI Epirus-Kostakii**	Epirus	Epirus	39.12208, 20.94737	30.00	ADCON S08	Meteorological	Decentralized Administration of Epirus and Western Macedonia
1403	**Agios Spiridonas**	Epirus	Epirus	39.14904, 20.87591	10.00	ADCON S06	Meteorological	Decentralized Administration of Epirus and Western Macedonia
1404	**Kambi**	Epirus	Epirus	39.21634, 20.91295	20.00	ADCON S12	Meteorological	Decentralized Administration of Epirus and Western Macedonia

1405	**TOEB Lourou**	Epirus	Epirus	39.07888, 20.88525	10.00	ADCON S02	Meteorological	Decentralized Administration of Epirus and Western Macedonia
1406	**Kommeno**	Epirus	Epirus	39.05061, 21.01207	10.00	ADCON S09	Meteorological	Decentralized Administration of Epirus and Western Macedonia
1407	**Kompoti**	Epirus	Epirus	39.09518, 21.06071	15.00	ADCON S20	Meteorological	Decentralized Administration of Epirus and Western Macedonia

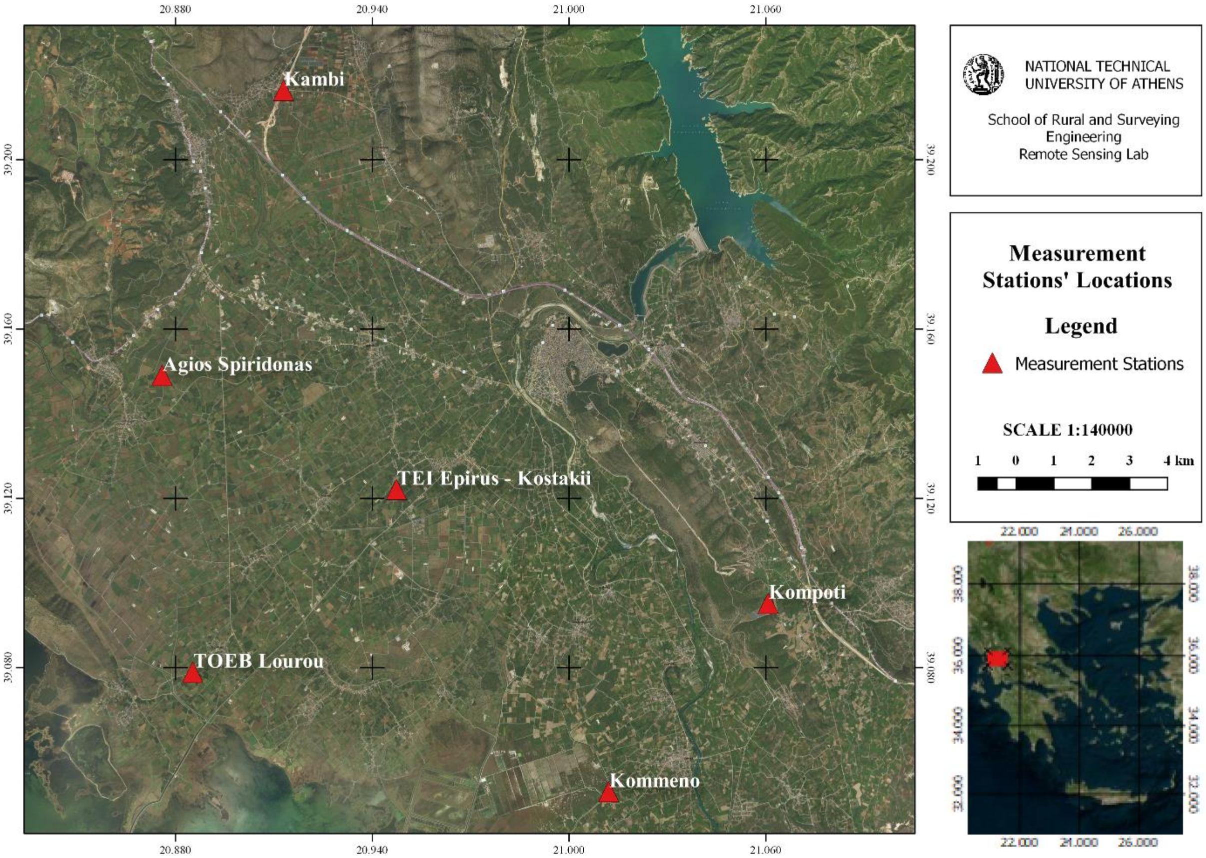

Figure 25: Map of In-Situ Measurements's Locations (Background Image by Bing Maps).

Except for the aforementioned In-Situ data, satellite data were also used which were derived from Google Earth Engine. The dataset included both optical and Radar data acquired from Landsat 8 and Sentinel 1 accordingly. Both datasets are already preprocessed to a certain level when used in Google Earth Engine. The purpose of using Landsat 8 data was to compute the

NDVI, NDMI and MI in each station location. The Image Collection that was used in Google Earth Engine was the Landsat 8 Surface Reflectance one which are provided by USGS. This dataset is the atmospherically corrected surface reflectance from the Landsat 8 OLI/TIRS sensors. These images contain 5 visible and near-infrared (VNIR) bands and 2 short-wave infrared (SWIR) bands processed to orthorectified surface reflectance, and two thermal infrared (TIR) bands processed to orthorectified brightness temperature. These data have been atmospherically corrected using LaSRC and includes a cloud, shadow, water and snow mask produced using CFMASK, as well as a per-pixel saturation mask. Strips of collected data are packaged into overlapping "scenes" covering approximately 170km x 183km using a standardized reference grid.

In order to obtain the most suitable data, the collection was filtered according to a starting date and an end date and the study area extend. The starting and end date were decided according to the range of dates observed in the merged In-Situ data.

In the following table, a description of the available bands and masks is provided.

Table 8: GEE Landsat 8 Image Collection Band Description (Source: GEE Documentation)

Name	Units	Scale	Wavelength	Description
B1		0.0001	0.435-0.451 µm	Band 1 (ultra blue) surface reflectance
B2		0.0001	0.452-0.512 µm	Band 2 (blue) surface reflectance
B3		0.0001	0.533-0.590 µm	Band 3 (green) surface reflectance
B4		0.0001	0.636-0.673 µm	Band 4 (red) surface reflectance
B5		0.0001	0.851-0.879 µm	Band 5 (near infrared) surface reflectance
B6		0.0001	1.566-1.651 µm	Band 6 (shortwave infrared 1) surface reflectance
B7		0.0001	2.107-2.294 µm	Band 7 (shortwave infrared 2) surface reflectance
B10	Kelvin	0.1	10.60-11.19 µm	Band 10 brightness temperature. This band, while originally collected with a resolution of 100m / pixel, has been resampled using cubic convolution to 30m.
B11	Kelvin	0.0001	11.50-12.51 µm	Band 11 brightness temperature. This band, while originally collected with a resolution of 100m / pixel, has been resampled using cubic convolution to 30m.
sr_aerosol				Aerosol attributes
Bitmask for sr_aerosol • **Bit 0: Fill** • **Bit 1: Aerosol retrieval - valid** • **Bit 2: Aerosol retrieval - interpolated** • **Bit 3: Water pixel** • **Bit 4: Water aerosol retrieval failed - needs interpolated** • **Bit 5: Neighbor of failed aerosol retrieval**				

• **Bits 6-7: Aerosol content** ○ **0: Climatology** ○ **1: Low** ○ **2: Medium** ○ **3: High**	
pixel_qa	Pixel quality attributes generated from the CFMASK algorithm.
Bitmask for pixel_qa • **Bit 0: Fill** • **Bit 1: Clear** • **Bit 2: Water** • **Bit 3: Cloud Shadow** • **Bit 4: Snow** • **Bit 5: Cloud** • **Bits 6-7: Cloud Confidence** ○ **0: None** ○ **1: Low** ○ **2: Medium** ○ **3: High** • **Bits 8-9: Cirrus Confidence** ○ **0: None** ○ **1: Low** ○ **2: Medium** ○ **3: High** • **Bit 10: Terrain Occlusion**	
radsat_qa	Radiometric saturation QA
Bitmask for radsat_qa • **Bit 0: Data Fill Flag** ○ **0: Valid data** ○ **1: Invalid data** • **Bit 1: Band 1 data saturated** • **Bit 2: Band 2 data saturated** • **Bit 3: Band 3 data saturated** • **Bit 4: Band 4 data saturated** • **Bit 5: Band 5 data saturated** • **Bit 6: Band 6 data saturated** • **Bit 7: Band 7 data saturated** • **Bit 8: Unused** • **Bit 9: Band 9 data saturated** • **Bit 10: Band 10 data saturated** • **Bit 11: Band 11 data saturated**	

The script that led to the selection of the dataset is presented below:

```
// 1. functions to add NDVI, NDMI and MI
var addNDMI = function(image) {
  return image.addBands(image.normalizedDifference(['B5', 'B6']).rename('NDMI'))
}

var addNDVI = function(image) {
  return image.addBands(image.normalizedDifference(['B5', 'B4']).rename('NDVI'))
}

var addMI = function(image) {
  return image.addBands(image.select('B5').divide(image.select('B2'))
  .rename('MI'))
}

// 2. define start/end dates
var dateStart ='2015-03-04'
var dateEnd='2018-04-12'

// LANDSAT 8 DATA
var l8data = ee.ImageCollection('LANDSAT/LC08/C01/T1_SR')

//Fetch the data
var l8 = l8data
  .filterBounds(stations2)
  .filterDate(dateStart,dateEnd)
  .map(addNDVI)
  .map(addNDMI)
  .map(addMI)
  .map(addTime)
  .map(function(img){
  return img.addBands(ee.Image.pixelLonLat())
})
```

Another Image Collection that was imported in Google Earth Engine contained the Sentinel-1 C-band Synthetic Aperture Radar Ground Range Detected (GRD) scenes, which were processed to backscatter coefficient (σ°) in decibels (dB). The backscatter coefficient represents target backscattering area (radar cross-section) per unit ground area. Due to the fact that it can vary by several orders of magnitude, it is converted to dB as 10*log10σ°. It measures whether the radiated terrain scatters the incident microwave radiation preferentially away from the SAR sensor (dB < 0) or towards the SAR sensor (dB > 0). This scattering behavior depends on the physical characteristics of the terrain, primarily the geometry of the terrain elements and their electromagnetic characteristics. This collection included the S1 Ground Range Detected (GRD) scenes, processed using the Sentinel-1 Toolbox to generate a calibrated, ortho-corrected products. Each scene has one of 3 resolutions (10, 25 or 40 meters), 4 band combinations (corresponding to scene polarization) and 3 instrument modes. Each scene also contains either 1 or 2 out of 4 possible polarization bands, depending on the instrument's polarization settings. The possible combinations are single band VV or HH, and dual band VV+VH and HH+HV: 1. VV: single co-polarization, vertical transmit/vertical receive 2. HH: single co-polarization, horizontal transmit/horizontal receive 3. VV + VH: dual-band cross-polarization, vertical transmit/horizontal receive 4. HH + HV: dual-band cross-polarization, horizontal transmit/vertical receive. An additional 'angle' band is also included in each scene where the approximate viewing incidence angle in degrees at every point is contained. This band is generated by interpolating the 'incidenceAngle' property of the 'geolocationGridPoint' gridded field provided with each asset. Imagery in Google Earth Engine is preprocessed with Sentinel-1 Toolbox. The preprocessing steps that are implemented are the following:

1. Apply orbit file: Updates orbit metadata with a restituted orbit file.
2. GRD border noise removal: Removes low intensity noise and invalid data on scene edges. (As of January 12, 2018)
3. Thermal noise removal: Removes additive noise in sub-swaths to help reduce discontinuities between sub-swaths for scenes in multi-swath acquisition modes. (This operation cannot be applied to images produced before July 2015)
4. Radiometric calibration: Computes backscatter intensity using sensor calibration parameters in the GRD metadata.
5. Terrain correction (orthorectification): Converts data from ground range geometry, which does not take terrain into account, to σ° using the SRTM 30 meter DEM or the ASTER DEM for high latitudes (greater than 60° or less than -60°). The final terrain corrected values are converted to decibels via log scaling (10*log10(x)) and quantized to 16-bits.

In the following table, a description of the available bands is provided.

Table 9: GEE Sentinel-1 Image Collection Band Description (Source: GEE Documentation)

Name	Units	Min	Max	X Resolution	Y Resolution	Wavelength	Description
HH		-50*	1*	10 meters	10 meters	5.405GHz	Single co-polarization, horizontal transmit/horizontal receive
HV		-50*	1*	10 meters	10 meters	5.405GHz	Dual-band cross-polarization, horizontal transmit/vertical receive
VV		-50*	1*	10 meters	10 meters	5.405GHz	Single co-polarization, vertical transmit/vertical receive

VH		-50*	1*	10 meters	10 meters	5.405GHz	Dual-band cross-polarization, vertical transmit/horizontal receive
angle	Degrees	0*	90*				Approximate viewing incidence angle

* estimated min or max value

In order to obtain the most suitable data, the collection was filtered according to a starting date and an end date as done while filtering the Landsat 8 data, the study area extend, the Transmitter/Receiver Polarisation, the instrument mode and the desired Resolution.

The script that led to the selection of the dataset is presented below:

```
// SENTINEL 1 DATA
var collectionVV = ee.ImageCollection('COPERNICUS/S1_GRD')
    .filterDate(dateStart,dateEnd)
    .filterBounds(areaOfInterest)
    .filter(ee.Filter.eq('instrumentMode', 'IW'))
    .filter(ee.Filter.listContains('transmitterReceiverPolarisation', 'VV'))
    .filterMetadata('resolution_meters', 'equals' , 10)
    .select(['VV'])
    .map(addTime)
```

2.1 GEOSPATIAL FRAMEWORKS AND COMPUTATIONAL TOOLS

2.1.1 GOOGLE EARTH ENGINE

Google Earth Engine is a cloud – based platform, were measuring and monitoring the changes in the earth's environment as well as accessing high-performance computing resources for processing very large geospatial datasets are made easy. It offers a multi-petabyte catalogue of earth observation data and intrinsically-parallel computational access to thousands of computers, meaning massive CPUs, in Google’s data centers.

The main goal of this initiative is to put this platform into the hands of scientists, in order to advance the broader operational deployment of existing scientific methods, and strengthen the ability for public institutions and civil society to better understand, manage and report on the state of their natural resources.

Earth Engine is accessed and controlled through a web Application Programming Interface (API) and an associated web-based Interactive Development Environment (IDE) that enables rapid prototyping and visualization of results.

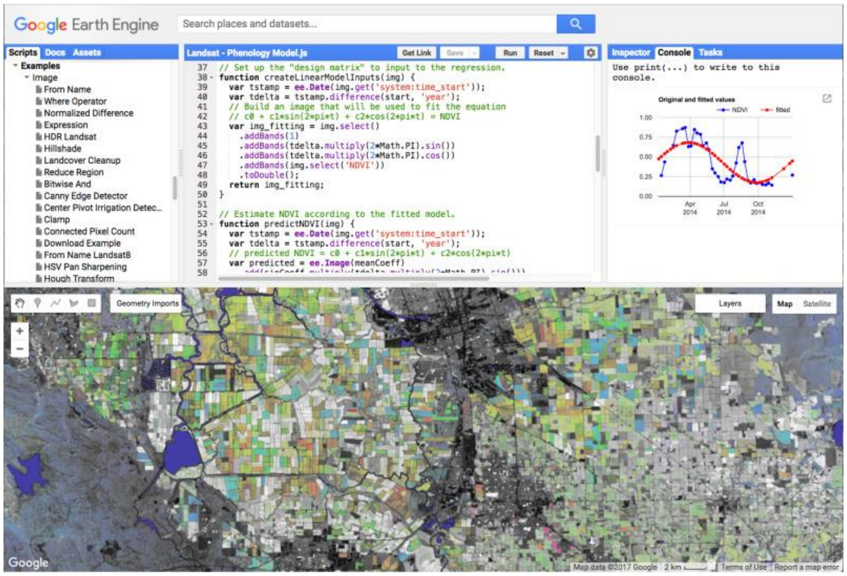

```
// Set up the "design matrix" to input to the regression.
function createLinearModelInputs(img) {
  var tstamp = ee.Date(img.get('system:time_start'));
  var tdelta = tstamp.difference(start, 'year');
  // Build an image that will be used to fit the equation
  // c0 + c1*sin(2*pi*t) + c2*cos(2*pi*t) = NDVI
  var img_fitting = img.select()
    .addBands(1)
    .addBands(tdelta.multiply(2*Math.PI).sin())
    .addBands(tdelta.multiply(2*Math.PI).cos())
    .addBands(img.select('NDVI'))
    .toDouble();
  return img_fitting;
}

// Estimate NDVI according to the fitted model.
function predictNDVI(img) {
  var tstamp = ee.Date(img.get('system:time_start'));
  var tdelta = tstamp.difference(start, 'year');
  // predicted NDVI = c0 + c1*sin(2*pi*t) + c2*cos(2*pi*t)
  var predicted = ee.Image(meanCoeff)
```

```
Use print(...) to write to this
console.
```

Figure 26: The User Interface of the Google Earth Engine Code Editor

Its large repository offers a variety of observations including numerous earth observation data from both active and passive sensors, weather and climate forecasts, topographic and socio-economic datasets, environmental variables and land cover. The data are pre-processed and ready to use while information-preserving, removing data management associated barriers and facilitating fast and efficient access. It should also be noted that all the images are always maintained in their original projection, resolution and bit depth, avoiding the data degradation that would be inherent in resampling all data to a fixed grid that may or may not be appropriate for any particular application. The data can be accessed by the users through a library provided by the Google Earth Engine API.

Table 10: Available data in the Google Earth Engine Catalogue (Source: GEE Documentation)

Dataset	Nominal resolution	Temporal granularity	Temporal coverage	Spatial coverage
Landsat				
Landsat 8 OLI/TIRS	30 m	16 day	2013–Now	Global
Landsat 7 ETM +	30 m	16 day	2000–Now	Global
Landsat 5 TM	30 m	16 day	1984–2012	Global
Landsat 4–8 surface reflectance	30 m	16 day	1984–Now	Global
Sentinel				
Sentinel 1 A/B ground range detected	10 m	6 day	2014–Now	Global
Sentinel 2A MSI	10/20 m	10 day	2015–Now	Global
MODIS				
MOD08 atmosphere	1°	Daily	2000–Now	Global
MOD09 surface reflectance	500 m	1 day/8 day	2000–Now	Global
MOD10 snow cover	500 m	1 day	2000–Now	Global
MOD11 temperature and emissivity	1000 m	1 day/8 day	2000–Now	Global
MCD12 Land cover	500 m	Annual	2000–Now	Global
MOD13 Vegetation indices	500/250 m	16 day	2000–Now	Global
MOD14 Thermal anomalies & fire	1000 m	8 day	2000–Now	Global
MCD15 Leaf area index/FPAR	500 m	4 day	2000–Now	Global
MOD17 Gross primary productivity	500 m	8 day	2000–Now	Global
MCD43 BRDF-adjusted reflectance	1000/500 m	8 day/16 day	2000–Now	Global
MOD44 veg. cover conversion	250 m	Annual	2000–Now	Global
MCD45 thermal anomalies and fire	500 m	30 day	2000–Now	Global
ASTER				
L1 T radiance	15/30/90 m	1 day	2000–Now	Global
Global emissivity	100 m	Once	2000–2010	Global
Other imagery				

PROBA-V top of canopy reflectance	100/300 m	2 day	2013–Now	Global
EO-1 hyperion hyperspectral radiance	30 m	Targeted	2001–Now	Global
DMSP-OLS nighttime lights	1 km	Annual	1992–2013	Global
USDA NAIP aerial imagery	1 m	Sub-annual	2003–2015	CONUS
Topography				
Shuttle Radar Topography Mission	30 m	Single	2000	60°N–54°S
USGS National Elevation Dataset	10 m	Single	Multiple	United States
USGS GMTED2010	7.5″	Single	Multiple	83°N–57°S
GTOPO30	30″	Single	Multiple	Global
ETOPO1	1′	Single	Multiple	Global
Landcover				
GlobCover	300 m	Non-periodic	2009	90°N–65°S
USGS National Landcover Database	30 m	Non-periodic	1992–2011	CONUS
UMD global forest change	30 m	Annual	2000–2014	80°N–57°S
JRC global surface water	30 m	Monthly	1984–2015	78°N–60°S
GLCF tree cover	30 m	5 year	2000–2010	Global
USDA NASS cropland data layer	30 m	Annual	1997–2015	CONUS
Weather, precipitation & atmosphere				
Global precipitation measurement	6′	3 h	2014–Now	Global
TRMM 3B42 precipitation	15′	3 h	1998–2015	50°N–50°S
CHIRPS precipitation	3′	5 day	1981–Now	50°N–50°S
NLDAS-2	7.5′	1 h	1979–Now	North America
GLDAS-2	15′	3 h	1948–2010	Global
NCEP reanalysis	2.5°	6 h	1948–Now	Global
ORNL DAYMET weather	1 km	Annual	1980–Now	North America
GRIDMET	4 km	1 day	1979–Now	CONUS
NCEP global forecast system	15′	6 h	2015–Now	Global
NCEP climate forecast system	12′	6 h	1979–Now	Global
WorldClim	30″	12 images	1960–1990	Global
NEX downscaled climate projections	1 km	1 day	1950–2099	North America
Population				
WorldPop	100 m	5 year	Multiple	2010–2015
GPWv4	30″	5 year	2000–2020	85°N–60°S

Each image is accompanied with metadata in a key/value format, containing information such as the acquisition time, the location, and the conditions under which the image was collected or processed. Moreover, related images, such as the images produced by a specific sensor, are grouped together and can be accessed as an "Image Collection". Collections provide fast filtering and sorting capabilities. This is crucial as it makes it easy for users to perform queries through millions of individual images and select data that meet specific spatial, temporal or other criteria.

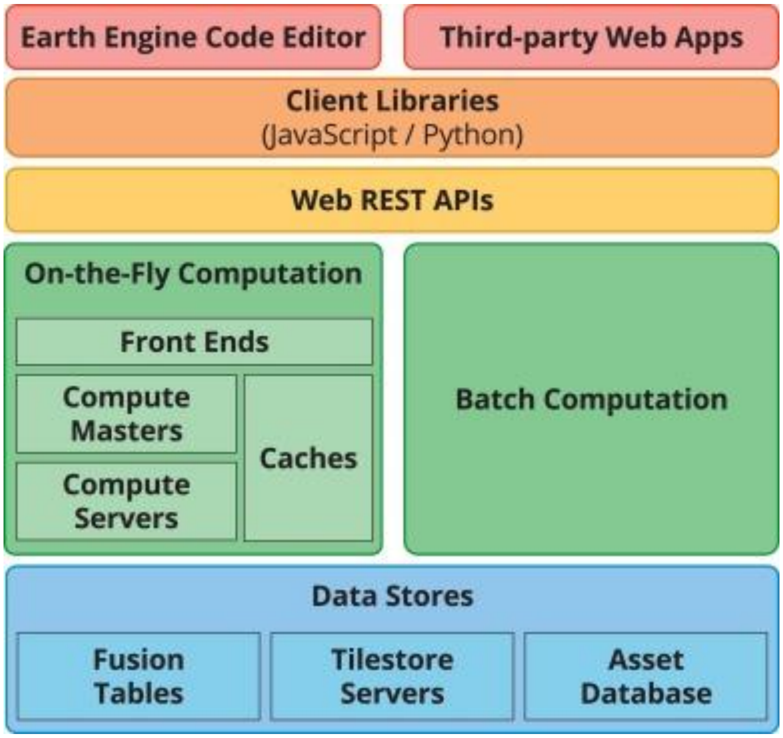

Figure 27: Google Earth Engine's System Architecture

2.1.2 R STATISTICAL PACKAGE

R is a free and open source software environment and programming language for statistical computing and graphics visualization, developed in 1995 at the University of Auckland as an environment for statistical computing and graphics (Ihaka and Gentleman, 1996). Open source means that the source code of R is accessible to everyone and anyone is allowed to contribute to the software. This, in fact, expands the capabilities of R dynamically. R comes as a base package with some basic statistical functionality but people contribute by creating packages which can be downloaded and implemented in R and expand the capabilities. R along with the additional packages are stored in 'Comprehensive R Archive Network', which is most commonly known as CRAN. CRAN is 'mirrored' at different places across the globe.

Since 1995 R has become one of the dominant software environments for data analysis and is used by a variety of scientific disciplines, including soil science, ecology, and geoinformatics (Envirometrics CRAN Task View; Spatial CRAN Task View). R is particularly popular for its graphical capabilities, but it is also prized for its GIS capabilities which make it relatively easy to generate raster-based models. More recently, R has also gained several packages which are designed specifically for analyzing soil data.

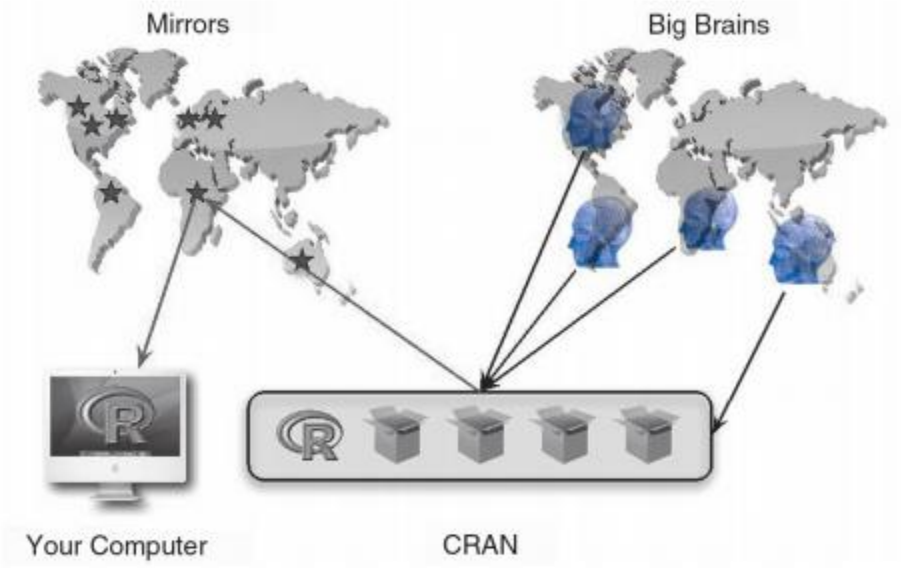

Figure 28: Users download R and install Packages (uploaded by Statisticians around the world) to their own computer via their nearest CRAN

R can be used along with RStudio which is a free, user friendly and open-source integrated development environment (IDE) for R.

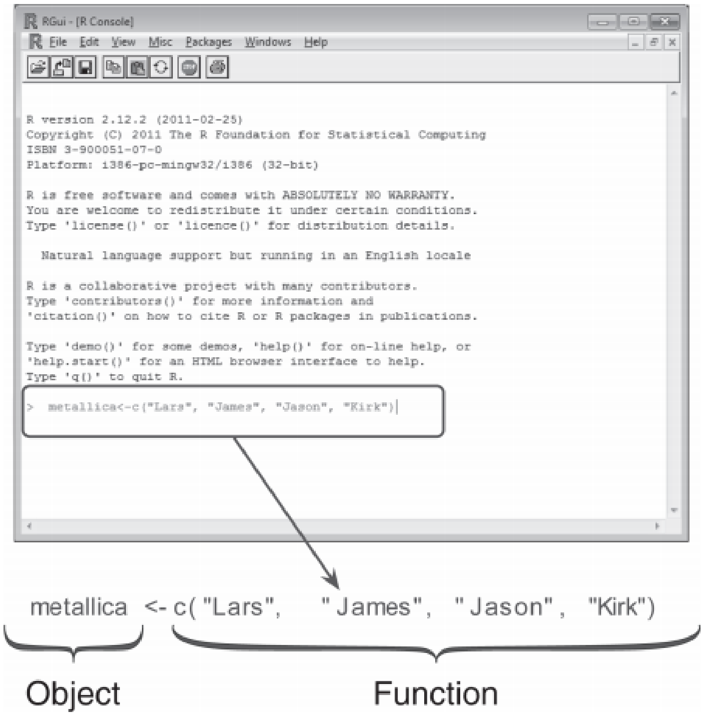

```
R version 2.12.2 (2011-02-25)
Copyright (C) 2011 The R Foundation for Statistical Computing
ISBN 3-900051-07-0
Platform: i386-pc-mingw32/i386 (32-bit)

R is free software and comes with ABSOLUTELY NO WARRANTY.
You are welcome to redistribute it under certain conditions.
Type 'license()' or 'licence()' for distribution details.

  Natural language support but running in an English locale

R is a collaborative project with many contributors.
Type 'contributors()' for more information and
'citation()' on how to cite R or R packages in publications.

Type 'demo()' for some demos, 'help()' for on-line help, or
'help.start()' for an HTML browser interface to help.
Type 'q()' to quit R.

> metallica<-c("Lars", "James", "Jason", "Kirk")
```

Figure 29: The R environment

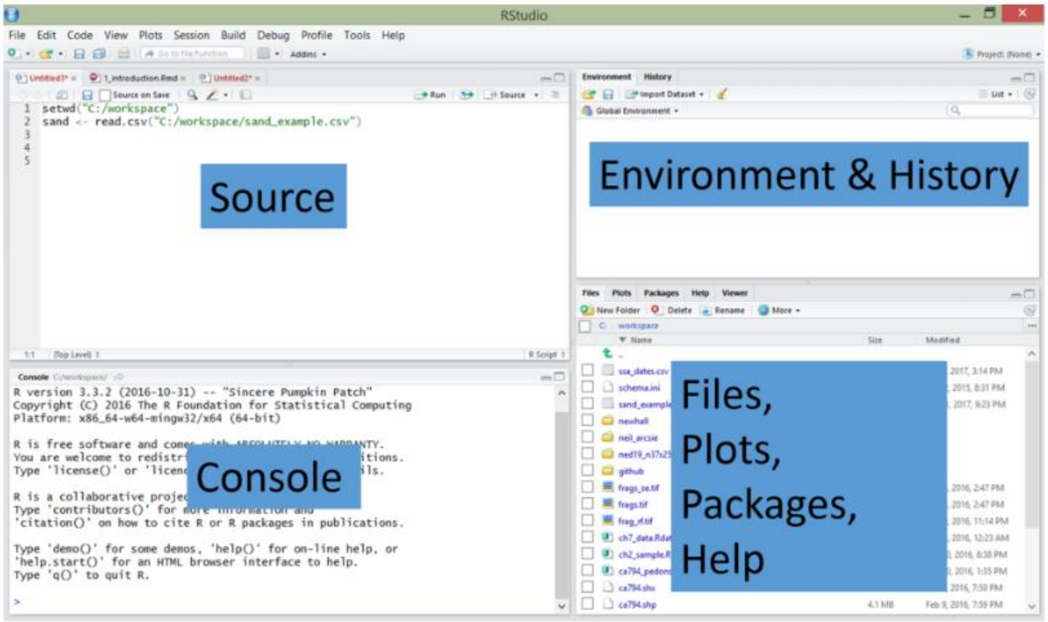

```
setwd("C:/workspace")
sand <- read.csv("C:/workspace/sand_example.csv")
```

```
R version 3.3.2 (2016-10-31) -- "Sincere Pumpkin Patch"
Copyright (C) 2016 The R Foundation for Statistical Computing
Platform: x86_64-w64-mingw32/x64 (64-bit)

R is free software and come                       TY.
You are welcome to redistr                      itions.
Type 'license()' or 'licenc                     ils.

R is a collaborative projec
Type 'contributors()' for
'citation()' on how to cite R or R packages in publications.

Type 'demo()' for some demos, 'help()' for on-line help, or
'help.start()' for an HTML browser interface to help.
Type 'q()' to quit R.

>
```

Figure 30: RStudio User Interface

3 METHODOLOGY

In this chapter, the applied methodology is going to be analyzed. In order to make the processing steps perfectly clear to understand, a flowchart exhibiting the methodology is presented below:

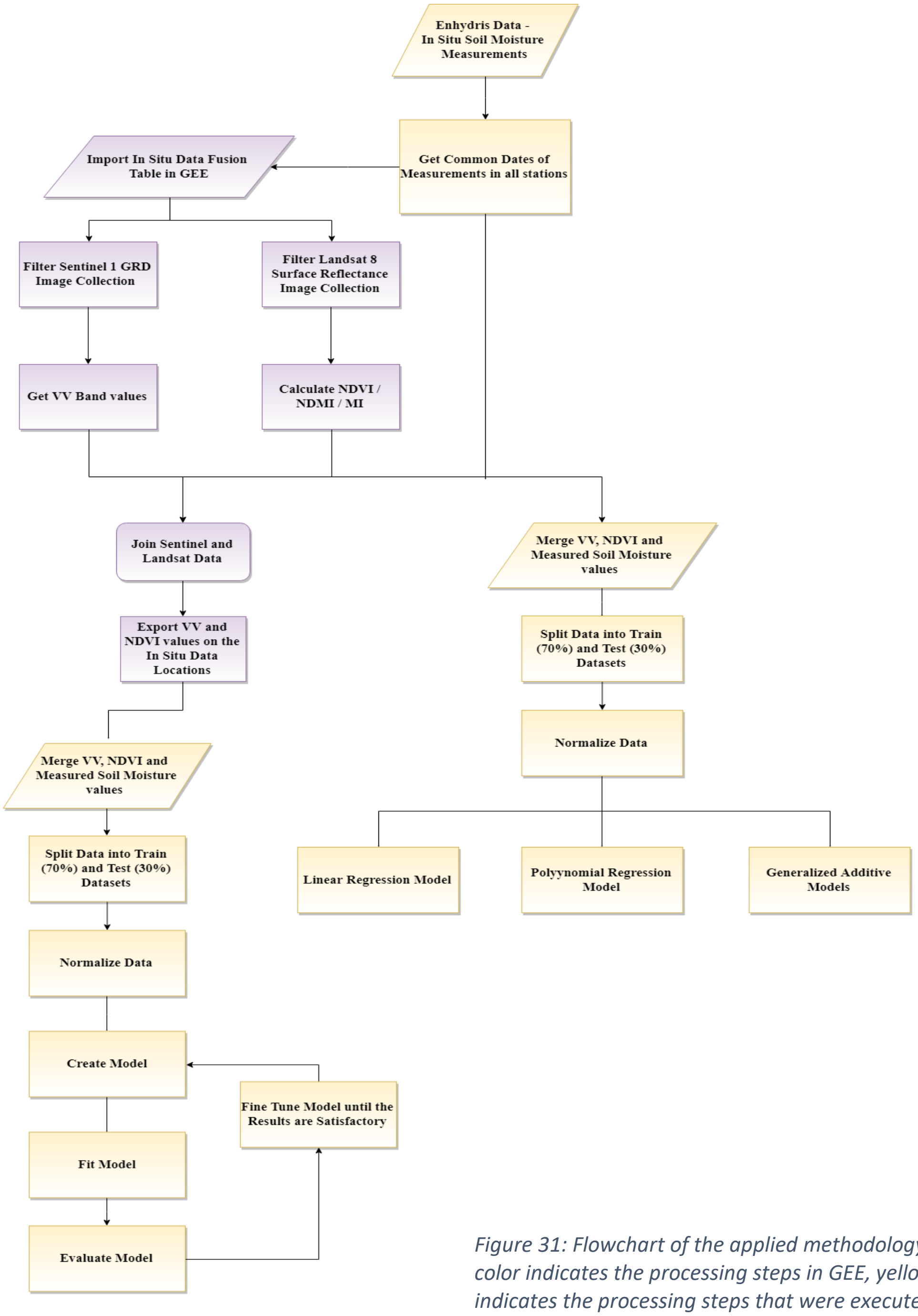

Figure 31: Flowchart of the applied methodology (purple color indicates the processing steps in GEE, yellow color indicates the processing steps that were executed in R)

The methodology which was implemented in the current study was divided into two parts. The first part included the preparation of the dataset that is going to be used as input and output in the statistical and machine learning techniques and the second part included the execution, the refinement and the evaluation of the selected statistical models and machine learning techniques which included Linear Regression Models, Polynomial Regression Models, Generalized Additive Models and Artificial Neural Networks. The available data that were ready to be processed included the pre-processed In-Situ data and the Sentinel-1 and Landsat 8 satellite images as obtained through Google Earth Engine.

During the preparation of the dataset, the selected Sentinel 1 and Landsat 8 satellite images were processed in Google Earth Engine using the Google Earth Engine Code Editor. The processing script was developed using the Javascript API. Before processing the satellite data, the locations of the stations were imported into Google Earth Engine. This was done by creating a Shapefile (ESRI format) from a CSV file with the stations' coordinates using R. A shapefile is a simple, nontopological format for storing the geometric location and attribute information of geographic features. Geographic features in a shapefile can be represented by points, lines, or polygons (areas). The workspace containing shapefiles may also contain dBASE tables, which can store additional attributes that can be joined to a shapefile's features. (ESRI, 1998).

Then Shape Escape was used in order to transform the shapefile into fusion tables which are supported by Google Earth Engine. Google Fusion Tables is a web service provided by Google for data management. Fusion tables can be used for gathering, visualising and sharing data tables. Data are stored in multiple tables that users can view and download. (Halevy and Shapley, 2009; Gonzalez et al., 2010).

Google Fusion Tables provide a relatively easy way to display geographic data on top of Google Maps. Data can be uploaded in .csv, .tsv, or .txt file formats. The data is geocoded based on a field (or fields) were location information (address, city, country, lat/long, etc.) is stored. This process works well for point data and for creating heat maps based on countries.

One way to import a shapefile directly into Google Fusion Tables is to use Shape Escape. Shape Escape was developed by Josh Livni (source code: http://code.google.com/p/shpescape/) and provides options to convert shapefiles to either Google Fusion Tables or GeoJSON and TopoJSON.

After the above steps were executed, the Normalized Difference Vegetation Index, the Normalized Difference Moisture Index and the Moisture Index were calculated for each one of the selected Landsat 8 Images and were added as separate new bands. Then the backscattering values were also added as a band in the corresponding images.

The Normalized Difference Vegetation Index (NDVI), as described by Rouse et al. (1974), is very effective in the determination of the density of vegetation in a specified area. It is based on the fact that chlorophyll, strongly absorbs visible light (from 0.4 to 0.7 μm) for use in photosynthesis while, on the contrary, the leaves' cell structure strongly reflects near-infrared light (from 0.7 to 1.1 μm). This means that the more leaves a plant has, the more these wavelengths of light are affected.

Figure 32: Vegetation indices with percentage of radiations emitted (Source: www.agricolus.com)

The mathematic formula of NDVI is formed as:

$$NDVI = \frac{NIR - Red}{NIR + Red}$$

The application of the NDVI equation on a given pixel results in a number that ranges from -1 to 1. A value of NDVI which is equal to zero is interpreted as no vegetation while NDVI values close to +1 indicate the highest possible density of green leaves.

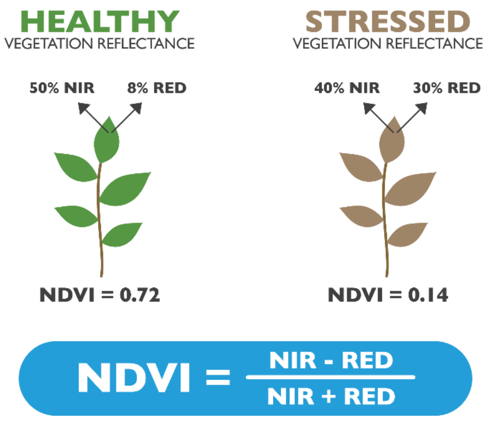

Figure 33: NDVI value interpretation (Source: www.agricolus.com)

It is important to note that NDVI was used in the current study, as according to Wang et al (2007), remotely sensed vegetation indices could be used effectively in order to estimate root zone soil moisture. Wang et al (2007) investigated the potential of NDVI to estimate root zone soil moisture using an 8-day average of NDVI and soil moisture.

Except for NDVI, Normalized Difference Moisture Index (NDMI) was also used as described by Vermote et al. (2016). The NDMI is able to describe the crop's water stress level and it is expressed as the ratio of the difference and the sum of the refracted radiations in the Near-Infrared (NIR) and Short-Wave Infrared (SWIR).

$$NDMI = \frac{NIR - SWIR}{NIR + SWIR}$$

NDMI's values vary between -1 and 1 where the positive data values correspond to typically moist areas while the negative values represent non-water features.

The SWIR reflectance reveals changes in both the spongy mesophyll structure in vegetation canopies and the vegetation water content, while the NIR reflectance depends on the leaf internal structure and leaf dry matter content but it is not affected by the water content. Combining the NIR with the SWIR leads to the removal of the variations induced by leaf internal structure and leaf dry matter content, which results in improved accuracy in retrieving the vegetation water content. The amount of water available in the internal leaf structure largely affects the spectral reflectance in the SWIR interval of the electromagnetic spectrum. SWIR reflectance is therefore negatively related to leaf water content (Gao, 1996). The bands of Landsat 8 that were used to compute the NDMI were Band 5 (NIR) and Band 6 (SWIR).

Last but not least, Moisture Index (MI) was also calculated as proposed by Dupigny and Lewis (1999). According to Dupigny and Lewis (1999), this index best captured the difference between urban areas, water bodies and full-leaf versus leafless conditions. MI can be calculated using the following formula and it has a native scaling of 0 to 1.

$$MI = \frac{NIR}{Blue}$$

The Blue band is able to differentiate between soil and vegetation as well as between deciduous and evergreen species. It is also known to provide water penetration properties. The NIR band is capable of determining the biomass while detecting the water bodies and vegetation.

The next processing step included the extraction of all the VV Backscattering, NDVI, NDMI and MI values on the stations' locations. This was implemented by using the ReduceRegions functionality of Google Earth Engine. The result of the aforementioned procedure was then exported in .csv format for each station.

Having the satellite data filtered, pre-processed and collected they needed to be joined to the In-Situ measurements in order to obtain two resulting 3D data frames (one for each Landsat 8 data and one for Sentinel 1 data, each consisting of 6 tables, one table for each station) with Date, NDVI, NDMI, MI and Measured Soil Moisture data for each station. In order to achieve this, all the available data, including the csv files exported through Google Earth Engine and the In-Situ measurements from Enhydris were imported into R and they were joined together by date.

As long as the Landsat 8 dataset is concerned, the stations Agios Spyridonas, Kampi and TOEB Lourou included 3 tables of 39 observations of each variable, the station TEI Epirus Kostakii included 1 table of 43 observations of each variable and the stations Kompoti and Kommeno included 84 observations of each variable. As a result, the final dataset included 328 observations of each variable derived by Landsat 8 data.

The Landsat 8 Images that led to the extraction of the values on the point locations are presented in the Appendix A.

The same procedure was also applied on the Sentinel 1 data. Each one of the stations Agios Spyridonas, Kommeno, Kompoti, TEI Epirus Kostakii and TOEB Lourou included 144 observations of the VV Backscattering while the station named Kampi included 145 observations of the aforementioned variable, resulting in a final dataset of 865 observations of the VV Backscattering derived by Sentinel 1 data. The Sentinel 1 Images that led to the extraction of the values on the point locations are presented in the Appendix B.

At this point the datasets were fully prepared to examine the potential of each variable to estimate and predict the soil moisture. Before applying any statistical or machine learning methodology on the data, all the variables were plotted versus the measured soil moisture values, in order to assess and detect any preliminary trends and correlations between the data. The following plot presents the comparison between the NDVI, NDMI, MI and measured soil moisture time series.

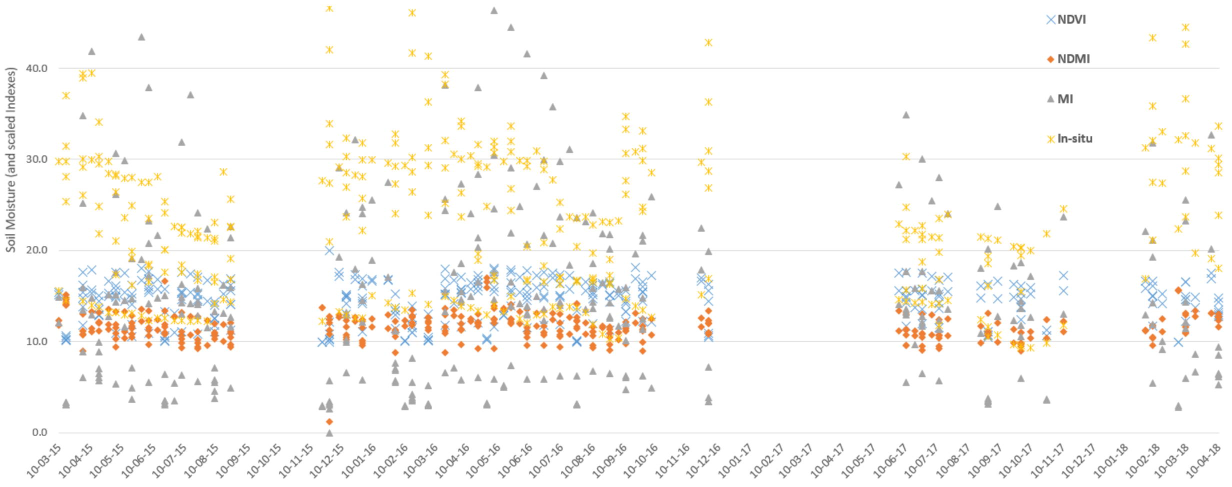

Figure 34: Soil Moisture In-Situ Measurements and values of NDVI, NDMI and MI, retrieved by Landsat 8 data. A total of 328 measurements of (x10) NDVI, (x10) NDMI and (x3) MI during a time range difference of +/- 2 days.

The following plot showcases the comparison between the values of the VV Backscattering and the measured soil moisture.

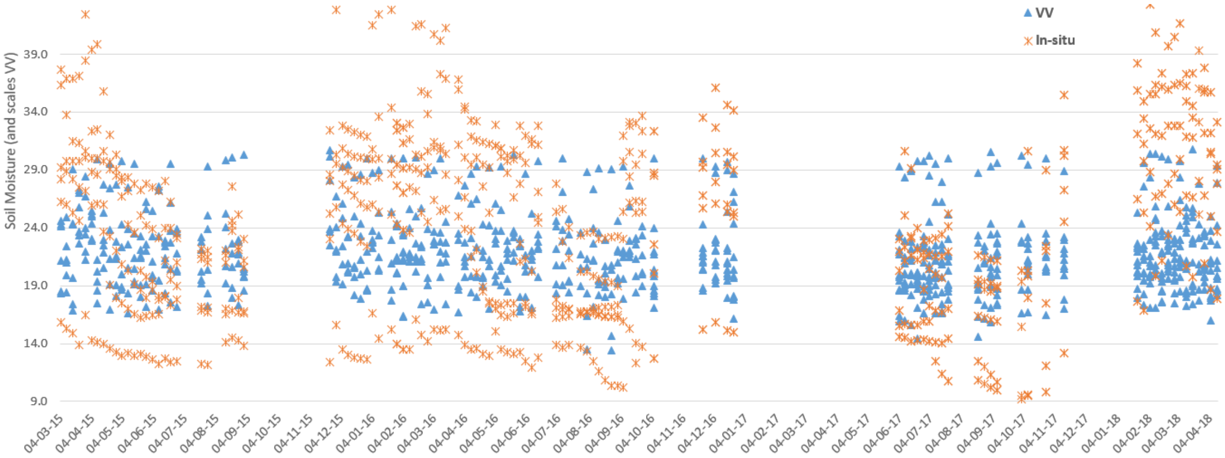

Figure 35: In-Situ Measurements of Soil Moisture and VV Backscattering values (db). A total of 865 measurements and the corresponding values of (+30) VV Backscattering during a time range of +/- 2 days.

The time series plot of the VV Backscattering and the measured soil moisture reveals a higher correlation between the two variables than the ones detected in the timeseries plots of the NDVI, NDMI, MI and measured soil moisture.

The next step of this research included the application of several statistical and machine learning techniques on the data, in order to identify the ability of the independent variables (NDVI, NDMI, MI and VV Backscattering) to estimate the soil moisture. The first technique that was applied was the most basic and commonly used model when it comes to statistical and predictive analysis and this is the Linear Regression Model. Linear Regression attempts to model the relationship between two continuous (quantitative) variables -one dependent and one (or more) independent variable(s)- by fitting a linear equation to the observations. The Linear Regression Model Equation is of the form:

$$y = b_0 + b_1 x$$

At this point, the dataset was partitioned into training and test datasets in order to evaluate each model's results using each time the 80% of the observations as training set and the remaining 20% as test dataset. After splitting the data, Linear Regression Analysis was performed using each time a different variable as the independent one and the measured soil moisture as a dependent one. The values of RMSE, r^2 and p-value were examined in order to evaluate the accuracy and predictability of the models. Except for the aforementioned information, the plots of the fitted model as well as of the plot of the predicted versus the measured soil moisture were also crucial to evaluate the models.

Except for examining linear models, nonlinear models were also examined. The next model that was examined was the Polynomial Regression Model.

In Polynomial Regression Analysis, the relationship between the independent variable and the dependent variable is modelled as an nth degree polynomial in x. Polynomial regression fits a nonlinear relationship between the two variables and is capable of describing nonlinear phenomena. The form of the Polynomial Regression Model equation is:

$$y = b_0 + b_1 x_1 + b_2 x_2^2 + \cdots + b_k x_k^k$$

It has to be noted that the fitted model is more reliable when a large number of observations is available. The determination of the order of the polynomial model applied using each of the independent variables, was a result of trial and error until the plotted models' fit was satisfactory and their significance was high.

The next model that was implemented, was the Generalized Additive Model (GAM). In case a nonlinear relationship is detected, the polynomial terms may not be flexible enough to capture the relationship, and spline terms require too detailed configuration. The Generalized additive models are capable of automatically fitting a spline regression. Generalized additive models are considered a powerful technique as the usual Linear relationship between the independent variable and the predictors is replaced by nonlinear smooth functions in order to capture and model the nonlinearities of the data. Using this model, the regression equation becomes:

$$y = a + f_1(x_1) + f_2(x_2) + \cdots + f_k(x_k)$$

where f_1, f_2…f_k are different nonlinear Functions on variables x_k.

Having examined the previously mentioned techniques, it was considered useful to examine the possibility to estimate soil moisture using both the NDVI and VV Backscattering as the predictor variables, using Deep Machine Learning Techniques such as Artificial Neural Networks. In order to achieve this, using the two satellite image datasets, Landsat 8 Surface Reflectance and Sentinel 1, a join algorithm was executed using again the Google Earth Engine API, in order to keep only the Landsat images which were acquired with a maximum acquisition date difference of 2 days in accordance to the Sentinel 1 Images. After executing this join procedure, 19 Sentinel 1 GRD and 19 Landsat 8 Surface Reflectance Images were kept in the dataset and the values of the two variables (NDVI and VV Backscattering) were exported in .csv format. After implementing the exported .csv in R and joining the extracted data with the corresponding In-Situ measurements the resulting dataset for each station included 19 dates of observations (19 dates x 6 stations resulted in 114 observations in total).

The 19 Landsat 8 Surface Reflectance Images that were joined to the Sentinel 1 Images are presented in the following table.

Table 11: Landsat 8 Metadata of the Joined Images

IMAGE ID	Date	CLOUD COVER (LAND)	SATELLITE	WRS PATH	WRS ROW
LC08_185033_20150317	2015-03-17	99,91	LANDSAT_8	185	33
LC08_185033_20150402	2015-04-02	12,9	LANDSAT_8	185	33
LC08_185033_20150504	2015-05-04	1,35	LANDSAT_8	185	33

LC08_185033_20150520	2015-05-20	18,15	LANDSAT_8	185	33
LC08_185033_20150621	2015-06-21	46,58	LANDSAT_8	185	33
LC08_185033_20150824	2015-08-24	11,29	LANDSAT_8	185	33
LC08_185033_20151128	2015-11-28	77,52	LANDSAT_8	185	33
LC08_185033_20151230	2015-12-30	27,74	LANDSAT_8	185	33
LC08_185033_20160216	2016-02-16	96,32	LANDSAT_8	185	33
LC08_185033_20160303	2016-03-03	82,08	LANDSAT_8	185	33
LC08_185033_20160404	2016-04-04	0,66	LANDSAT_8	185	33
LC08_185033_20160420	2016-04-20	2,69	LANDSAT_8	185	33
LC08_185033_20160522	2016-05-22	45,06	LANDSAT_8	185	33
LC08_185033_20160607	2016-06-07	16,35	LANDSAT_8	185	33
LC08_185033_20160709	2016-07-09	0,23	LANDSAT_8	185	33
LC08_185033_20160725	2016-07-25	28,73	LANDSAT_8	185	33
LC08_185033_20160826	2016-08-26	3,5	LANDSAT_8	185	33
LC08_185033_20160911	2016-09-11	59,84	LANDSAT_8	185	33
LC08_185033_20161216	2016-12-16	18,56	LANDSAT_8	185	33

The 19 Sentinel 1 Images that were joined to the Landsat 8 Images are presented in the following table.

Table 12: Sentinel 1 Metadata of the Joined Images

Date	Instrument	Instrument Mode	Platform	Product Class	Product Type	Orbit Pass	Relative Orbit	Resolution	Transmitter Receiver Polarisation
2015-03-16	Synthetic Aperture Radar	IW	A	SAR Standard L1 Product	GRD	Descending	80	H – 10m	[VV, VH]
2015-04-03	Synthetic Aperture Radar	IW	A	SAR Standard L1 Product	GRD	Ascending	175	H – 10m	[VV, VH]
2015-05-03	Synthetic Aperture Radar	IW	A	SAR Standard L1 Product	GRD	Descending	80	H – 10m	[VV, VH]
2015-05-21	Synthetic Aperture Radar	IW	A	SAR Standard L1 Product	GRD	Ascending	175	H – 10m	[VV, VH]
2015-06-20	Synthetic Aperture Radar	IW	A	SAR Standard L1 Product	GRD	Descending	80	H – 10m	[VV, VH]
2015-08-25	Synthetic Aperture Radar	IW	A	SAR Standard L1 Product	GRD	Ascending	175	H – 10m	[VV, VH]

2015-11-29	Synthetic Aperture Radar	IW	A	SAR Standard L1 Product	GRD	Ascending	175	H – 10m	[VV, VH]
2015-12-29	Synthetic Aperture Radar	IW	A	SAR Standard L1 Product	GRD	Descending	80	H – 10m	[VV, VH]
2016-02-15	Synthetic Aperture Radar	IW	A	SAR Standard L1 Product	GRD	Descending	80	H – 10m	[VV, VH]
2016-03-04	Synthetic Aperture Radar	IW	A	SAR Standard L1 Product	GRD	Ascending	175	H – 10m	[VV, VH]
2016-04-03	Synthetic Aperture Radar	IW	A	SAR Standard L1 Product	GRD	Descending	80	H – 10m	[VV, VH]
2016-04-21	Synthetic Aperture Radar	IW	A	SAR Standard L1 Product	GRD	Ascending	175	H – 10m	[VV, VH]
2016-05-21	Synthetic Aperture Radar	IW	A	SAR Standard L1 Product	GRD	Descending	80	H – 10m	[VV, VH]
2016-06-08	Synthetic Aperture Radar	IW	A	SAR Standard L1 Product	GRD	Ascending	175	H – 10m	[VV, VH]
2016-07-08	Synthetic Aperture Radar	IW	A	SAR Standard L1 Product	GRD	Descending	80	H – 10m	[VV, VH]
2016-07-26	Synthetic Aperture Radar	IW	A	SAR Standard L1 Product	GRD	Ascending	175	H – 10m	[VV, VH]
2016-08-25	Synthetic Aperture Radar	IW	A	SAR Standard L1 Product	GRD	Descending	80	H – 10m	[VV, VH]
2016-09-12	Synthetic Aperture Radar	IW	A	SAR Standard L1 Product	GRD	Ascending	175	H – 10m	[VV, VH]
2016-12-17	Synthetic Aperture Radar	IW	B	SAR Standard L1 Product	GRD	Descending	80	H – 10m	[VV, VH]

The next step included the configuration and the execution of the Artificial Neural Network. The processing steps were executed using R programming language in the RStudio IDE. Before importing the data in the Artificial Neural Network, the data had to be split into train and test data. It is crucial to use the majority of data to train the network, thus a percentage of 80% of the data was used as train data. Accordingly, the rest of the data were used for testing the predictions. After splitting the data, it is considered best practice to normalize them, so the input dependent and independent variables were scaled to [0, 1]. Normalization or scaling is not really a functional requirement in order to train the Neural Network, but it significantly helps as it transposes the input variables into the data range that the activation functions lie in (i.e. for logistic [0, 1] and tanh [-1, 1]. The method that was used to scale the data was the standardization. Standardization or Z-score normalization is considered the most commonly used scaling technique. In order to be calculated the arithmetic mean and standard deviation of the given data are used. It is really important though to keep in mind that both standard deviation and mean are sensitive to outliers which implies that this technique does not guarantee a common numerical range for the normalized scores.

Generally pre-processing the data before importing them to the neural network has several advantages as making the training of the network faster, more memory efficient and resulting in more accurate forecasting. (Rotich, 2014)

As long as the training of the Neural Network is concerned, several packages were tried in order to tune it and get satisfactory results by trial and error. Firstly, the package ‘neuralnet’ was used. The results were not satisfactory enough and another package was to be tried for experimenting. The second approach included the introduction of TensorFlow and Keras.

TensorFlow, a novel open source deep learning library based on computational graphs. It was developed by Google Brain Team and it was released in 2015 (Goldsborough, (2016). TensorFlow can be used with Python and with its low-level programming interface it provides a large scale of machine learning methods, especially powerful methods to build deep and complex neural networks, giving fine-grained control for their construction (Kallio, 2017).

Another tool that was used was Keras. Keras is an open source neural network library which is written in Python and is capable of running on top of TensorFlow, Microsoft Cognitive Toolkit or Theano. ("Keras backends", keras.io). It was developed as part of the project ONEIROS (Open-ended Neuro-Electronic Intelligent Robot Operating System), by a Google Engineer named François Chollet ("Keras Documentation", keras.io) Keras is user-friendly, modular and extensible, offering a high-level set of abstractions which make it easy to develop deep learning models.

The first step of creating a Neural Network with Keras, was to define the model. A sequential model was created by calling the keras_model_sequential() function and after that several layers were also defined. A sequential model is basically a linear stack of layers. The definition of the layers should include several information such as the output dimensions, which is the number of the neurons that consist in the next layer, and the activation function. When creating the first layer it is compulsory to define the input dimensions, which in this study is 2 since 2 variables will be the input. The activation function of a node defines the output of the node given an input. This output is then used as input for the next node and so on until a desired solution to the initial problem is found. The activation function that was chosen in the current study was the Rectified Linear Units (ReLU). ReLU can be described with the following mathematical formula.

$$R = \max(0, x)$$

This activation function has gotten extremely popular the last years as it is proven that avoids and rectifies vanishing gradient problem. For this reason, almost all Deep Learning Models use ReLU nowadays. Sigmoid and Tanh are two other possible alternatives but nowadays they are not suggested due to the vanishing Gradient Problem, which causes problems to the training process while it degrades the accuracy and performance of a Deep Neural Network Model.

After defining the initial properties of the network, it should be compiled which in fact means defining the learning process. The arguments that should be defined to compile the model are 3. The first argument is the Optimization algorithm or the Optimizer. Optimization algorithms help us minimize (or maximize) an Objective or Error function E(x) which is simply a mathematical function dependent on the Model's internal learnable parameters, such as Weights and Biases, which are used in computing the target values(Y) from the set of predictors(X) used in the model.

The gradient descent optimization function that was chosen was RMSprop, which is an unpublished, adaptive learning rate method proposed by Geoff Hinton in "Lecture 6e" of his Coursera Class (Hinton, 2012).

The next parameter that was introduced in the model was the Loss function. The Loss function is an important part in artificial neural networks, which measures the inconsistency between the actual and the predicted value. Neural networks are trained using gradient methods by an iterative process of decreasing a loss function, which is a non-negative value, where the robustness of model increases along with the decrease of the value of the loss function. The loss function that was chosen in the current study was the Mean Square Error (MSE). This function calculates the difference between the predicted and actual values, squares the result, making all the values positive, and then computes the mean value. The last argument that was required in order to compile the model was the metrics. A metric is basically a function that given the predicted and actual values of the sample, provides a scalar measure of how well the model fits the data. The metric that was selected in order to evaluate the model was the Mean Absolute Error (MAE). MAE measures the average magnitude of the errors in a set of predictions, without considering their direction. It's the average of the absolute differences between prediction and actual values where all individual differences have equal weight. It is computed through the following equation.

$$MAE = \frac{1}{n}\sum_{j=1}^{n} |y_j - \hat{y}_j|$$

At this point the training process should be defined and executed. In order to achieve this a set of 100 epochs was defined, which is the number of passes through the entire dataset, in order for the backpropagation algorithm to converge on a combination of weights with an acceptable level of accuracy. Moreover, setting the batch size is really important so that smaller parts of the data are training separately during an epoch. This results in updating the weights more than once during each epoch. After having all the above parameters set the training process was initiated and the model was fine-tuned by changing the number of the hidden layers and their neurons' and by setting a dropout rate. Dropout is a regularization technique for neural network models proposed by Srivastava, et al. (2014) and suggests a way to prevent Neural Networks from overfitting.

4 EXPERIMENTAL RESULTS

In this chapter, the results of the implemented methodologies, as described in the previous chapter, are going to be presented. It should be noted that the RMSE values indicate the mean deviation between the measured and the predicted soil moisture values.

The first approach to estimate and predict soil moisture in the study area included linear regression analysis using soil moisture as dependent variable and the indices that were calculated using Landsat 8 data, which were the NDVI, NDMI and MI, as independent variables. Linear regression was conducted using each independent variable separately while each variable was partitioned into training and test sets.

Firstly, linear regression using the measured soil moisture as dependent variable and NDVI as independent variable was performed. Before performing the linear regression though, the two variables were plotted in order to seek for any trends in their distribution. The resulting plot is presented below.

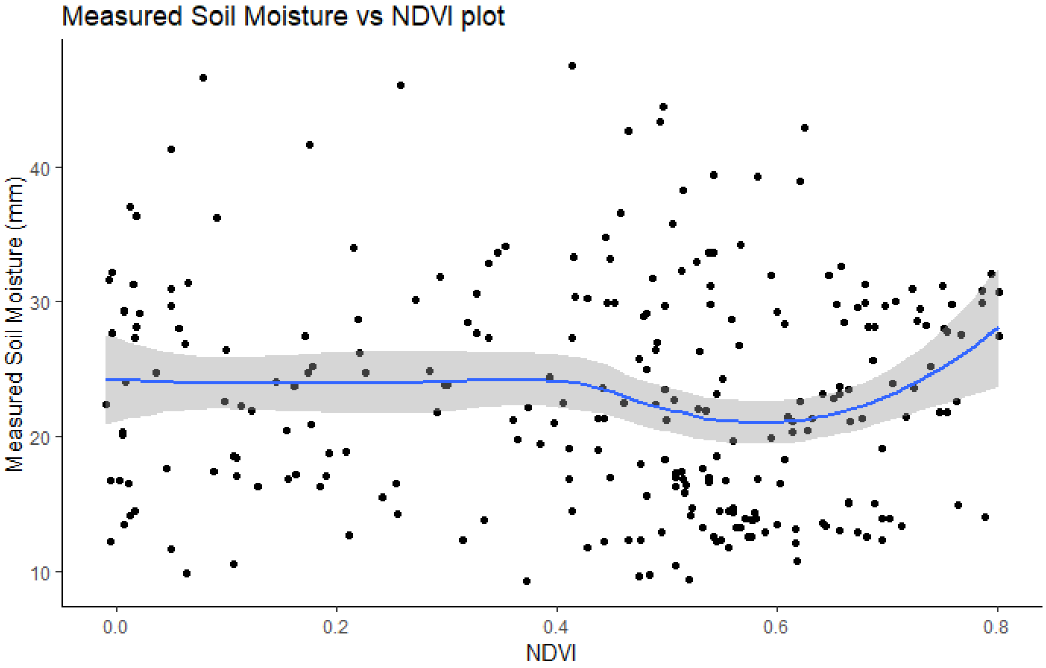

Figure 36: Plot of Measured Soil Moisture versus NDVI.

According to this plot, the two variables seem to have a nonlinear, though weak, relationship. A linear regression model was applied though in order to examine all the cases and exclude the poorly-fitting ones. The training set was used to train and compute the corresponding model, while the test set was used to predict and evaluate the results. The visualization of the resulting model is presented in the next graph.

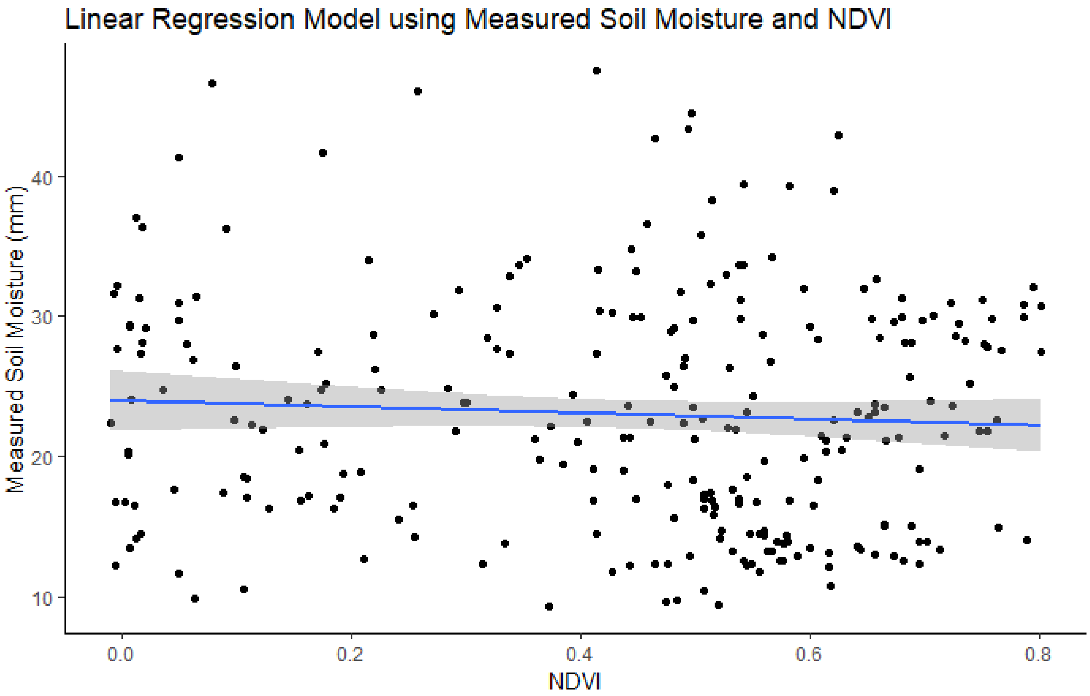

Figure 37: Linear Regression Model using Measured Soil Moisture and NDVI.

The metrics of the model accuracy, the RMSE and the r^2, were 7.479 and 0.04 respectively. RMSE indicates a deviation of about +/-7.479 mm between the predicted and measured soil moisture values. Moreover, the p-value was 0.33, implying that there is weak evidence against the null hypothesis and that the result was not statistically significant. After applying the linear regression on the training dataset, it was also applied to the test dataset in order to evaluate the model and compare the predicted soil moisture values with the measured ones, as shown in the next graph.

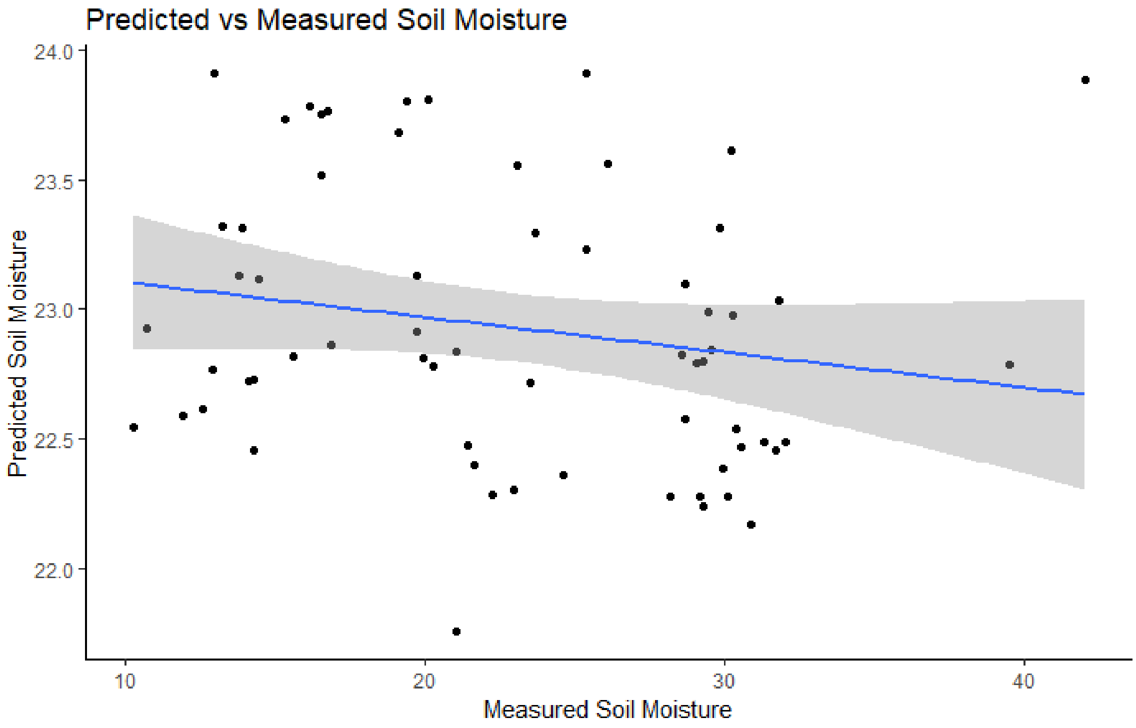

Figure 38: Predicted vs Measured Soil Moisture using Linear Regression Model and NDVI (n = 66 observations of the validation set).

According to the images presented above as well as the values of r^2 and RMSE, the linear regression model using the NDVI values, does not seem to be the most suitable one.

The next linear regression model that was calculated, included the soil moisture measurements as dependent variable and the NDMI as independent. The plot of the two variables showcased an almost linear relationship between them.

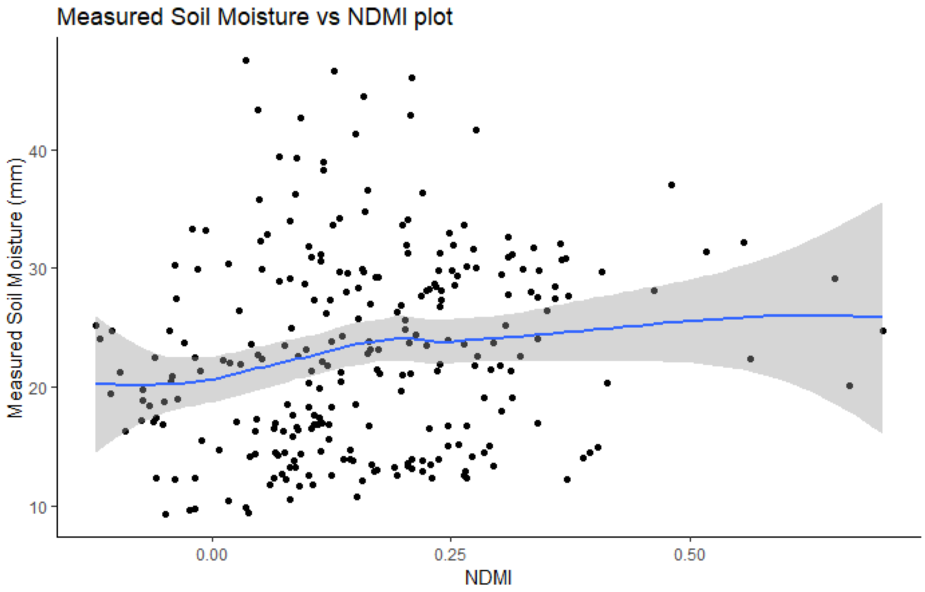

Figure 39: Plot of Measured Soil Moisture versus NDMI

.

The RMSE and r^2 that resulted from the application of the linear regression model were 7.268 and 0.033 respectively. It should be noted that the p-value of this model was 0.004 which is lower than the p-value of the previously implemented model and suggests that the result is statistically significant. The visualization of the model is presented below.

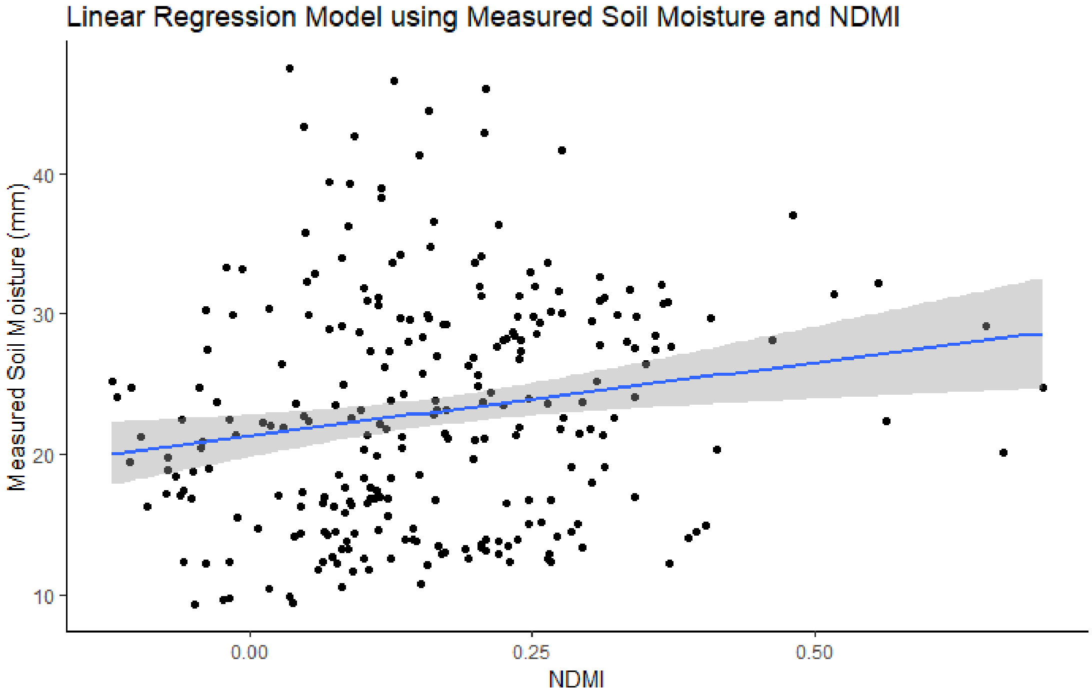

Figure 40: Linear Regression Model using Measured Soil Moisture and NDMI.

Moreover, the application of the model on the test dataset in comparison to the measured soil moisture values, is presented in the next image.

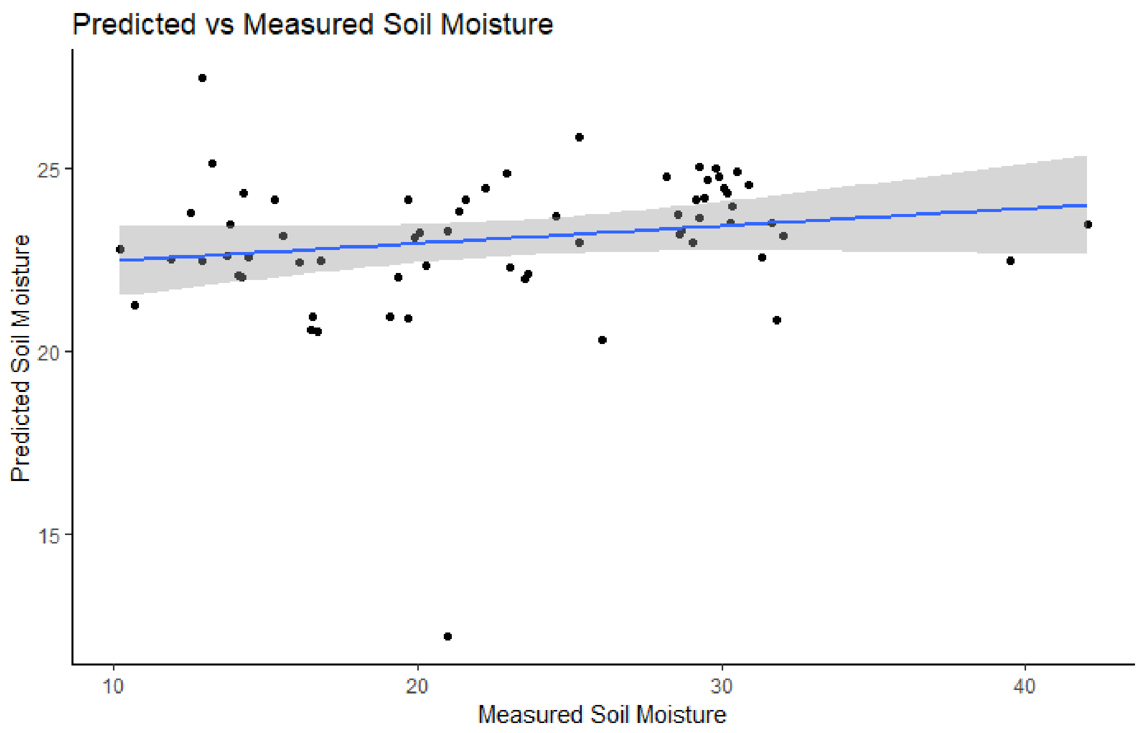

Figure 41: Predicted vs Measured Soil Moisture using Linear Regression Model and NDMI (n = 66 observations of the validation set).

According to the results as presented above, it appears that this model is more accurate than the previous one thought the results are still unsatisfactory.

The last variable that was used as a predictor in Linear Regression, being derived from Landsat 8 satellite data, was the MI. The result of plotting the dependent variable (measured soil moisture) with the independent variable showcased that the possibility of deriving a relationship between the two variables is low.

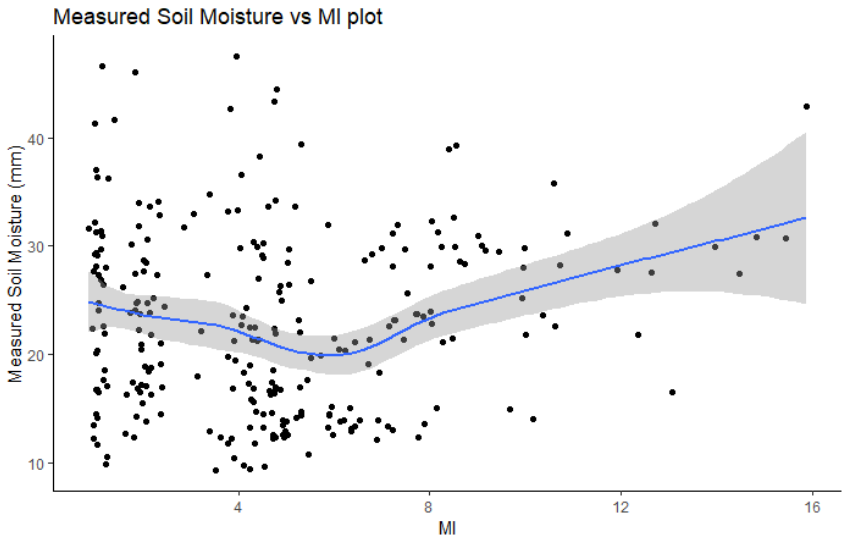

Figure 42: Plot of Measured Soil Moisture versus MI.

After applying the linear regression model using the MI as independent variable, the resulting RMSE and r^2 were 7.222 and 0.043 respectively, while the p-value being 0.1549, indicated that the result was not statistically significant. The visualization of the resulting model is presented below.

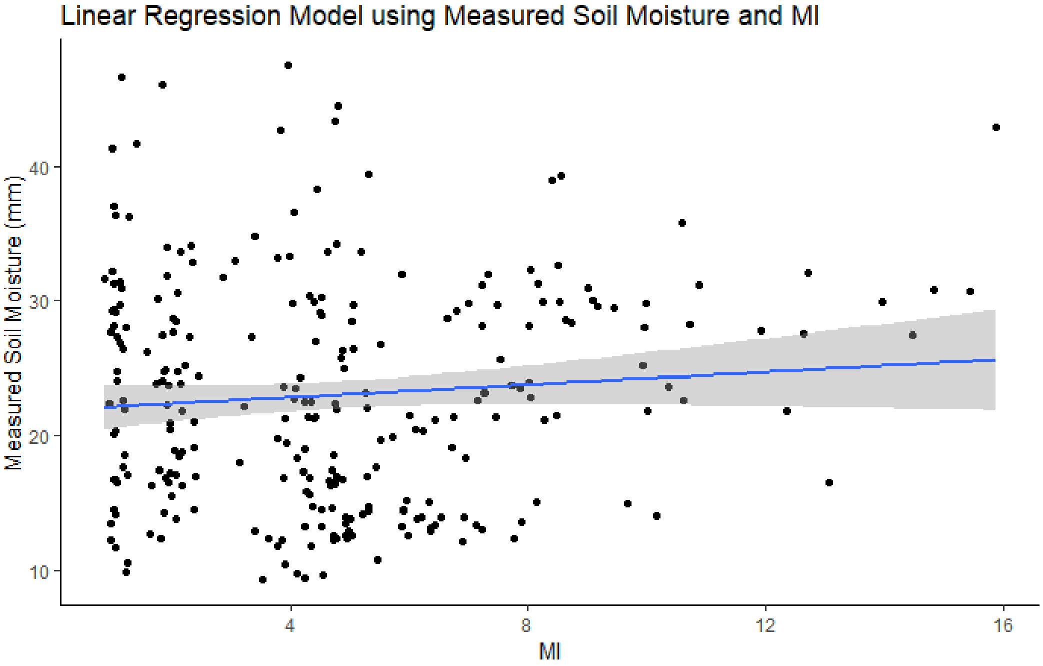

Figure 43: Linear Regression Model using Measured Soil Moisture and MI.

After applying the resulting linear regression model equation on the test dataset, the results were not found to be satisfactory.

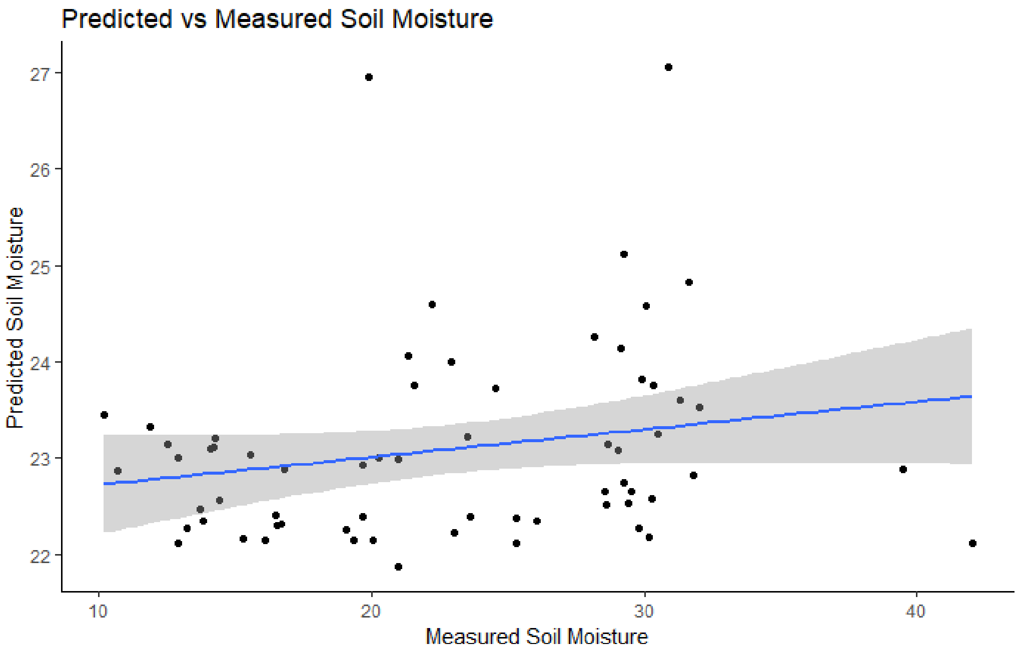

Figure 44: Predicted vs Measured Soil Moisture using Linear Regression Model and MI (n = 66 observations of the validation set).

After applying linear regression models using the indices derived by Landsat 8 data, linear regression was also implemented using the VV backscattering values derived by Sentinel 1 data. Before applying the linear regression model, the two variables were plotted.

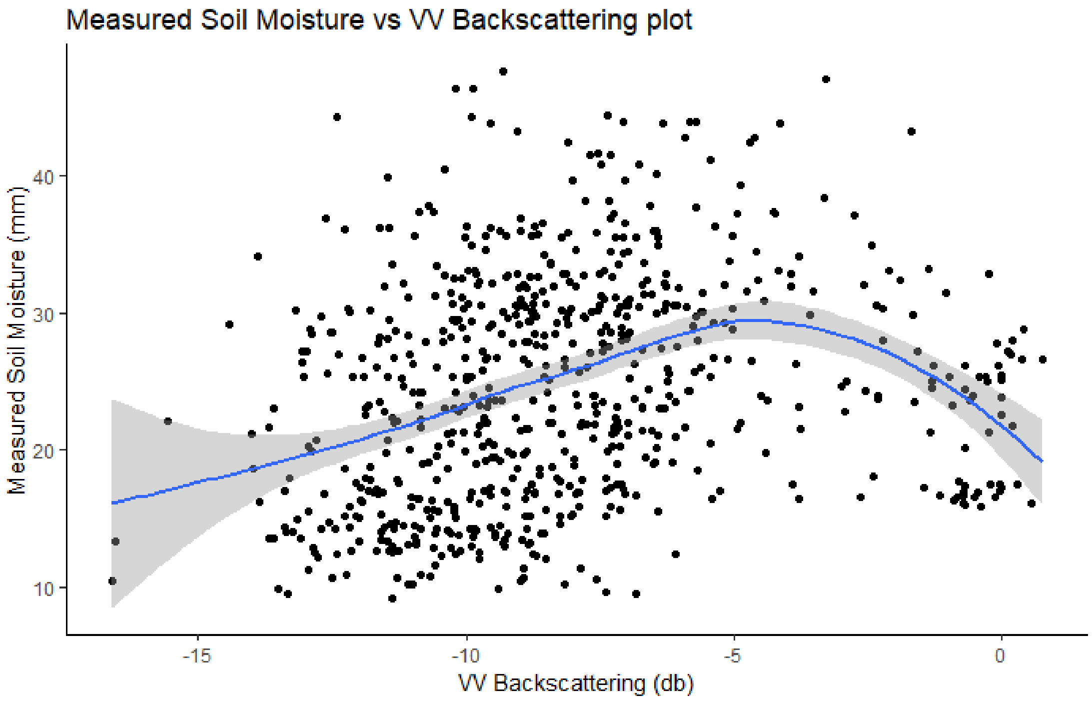

Figure 45: Plot of Measured Soil Moisture versus VV Backscattering.

The above plot suggests a nonlinear relationship between the two variables. The RMSE and r^2 of the resulting linear regression model using the VV Backscattering values were 8.058 and 0.043 respectively. Moreover, the p-value was 0.00000006. Being that low, it suggests a statistically significant result. The visualization of the model is presented below.

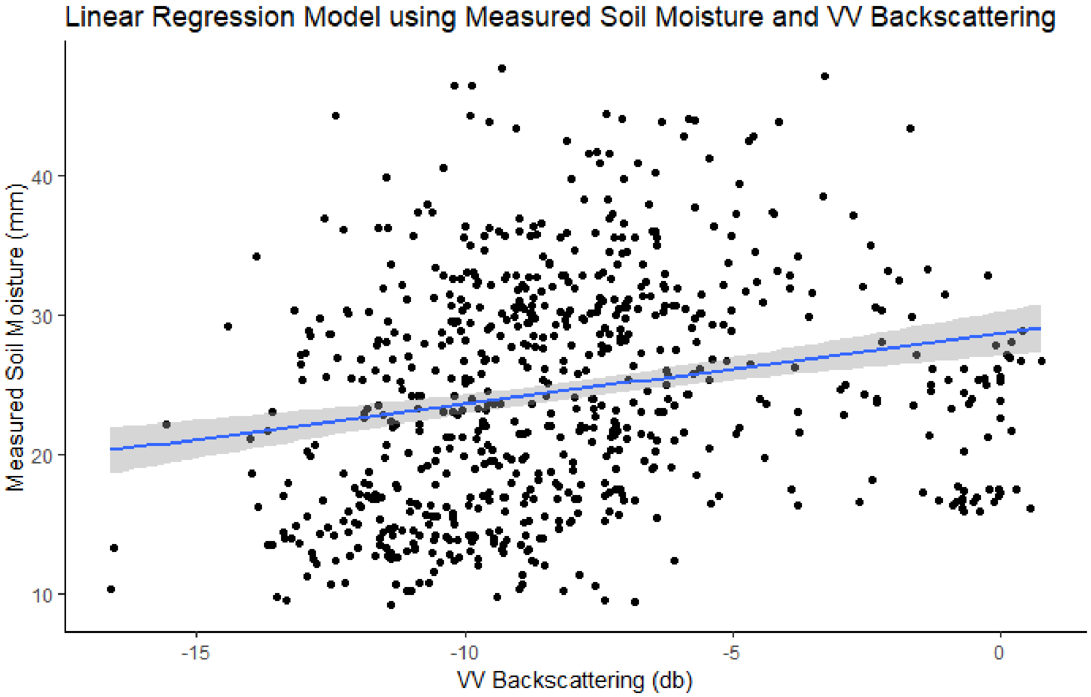

Figure 46: Linear Regression Model using Measured Soil Moisture and VV Backscattering.

The calculated regression model equation was also applied on the test dataset in order to evaluate the results. The comparison between the predicted and the measured soil moisture values is presented below.

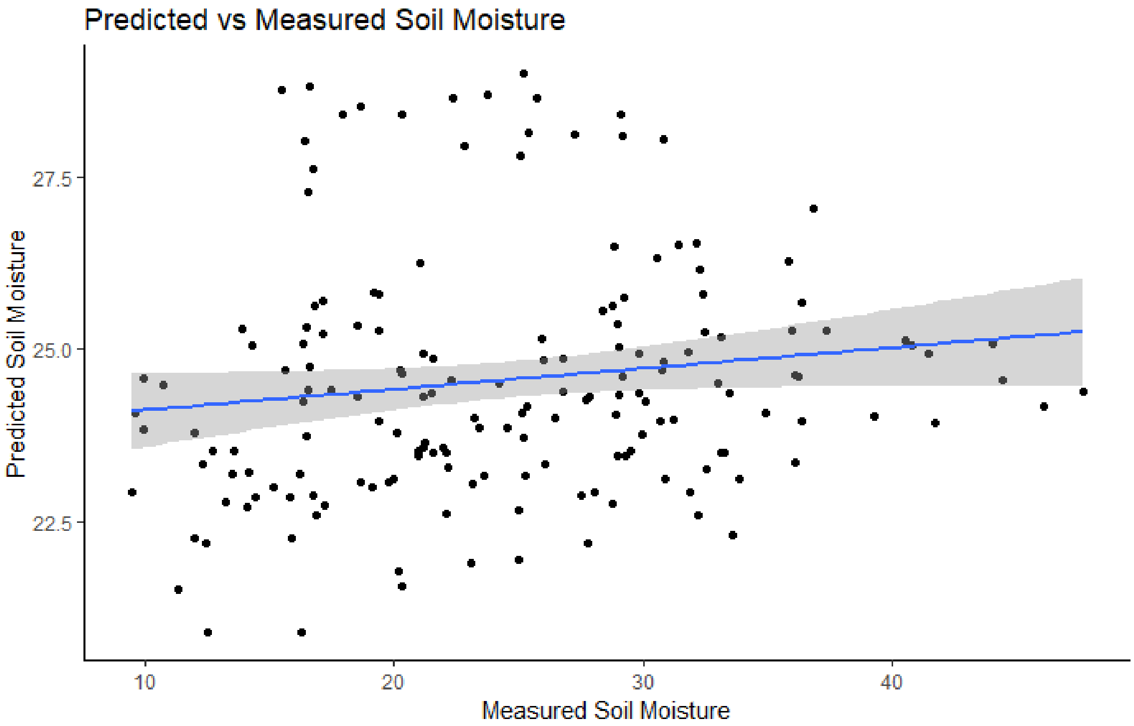

Figure 47: Predicted vs Measured Soil Moisture using Linear Regression Model and VV Backscattering (n = 173 observations of the validation set).

According to the metrics and the plots, the linear regression model using the VV Backscattering seems to fit better than the models using the indices derived by Landsat 8 data. The r^2 seems to be extremely low, but there are cases in the literature where r^2 is low and the models are accurate and vice versa. The RMSE in all cases ranges between 7 and 8 which is acceptable considering the range of the soil moisture values.

The use of linear regression models resulted in mainly unsatisfactory results. For this reason, polynomial regression was also applied using the same variables.

Firstly, the NDVI was used as independent variable in polynomial regression model. After many attempts, the model that was found to be more significant to use was a fifth-order polynomial regression model which is visualized in the next graph.

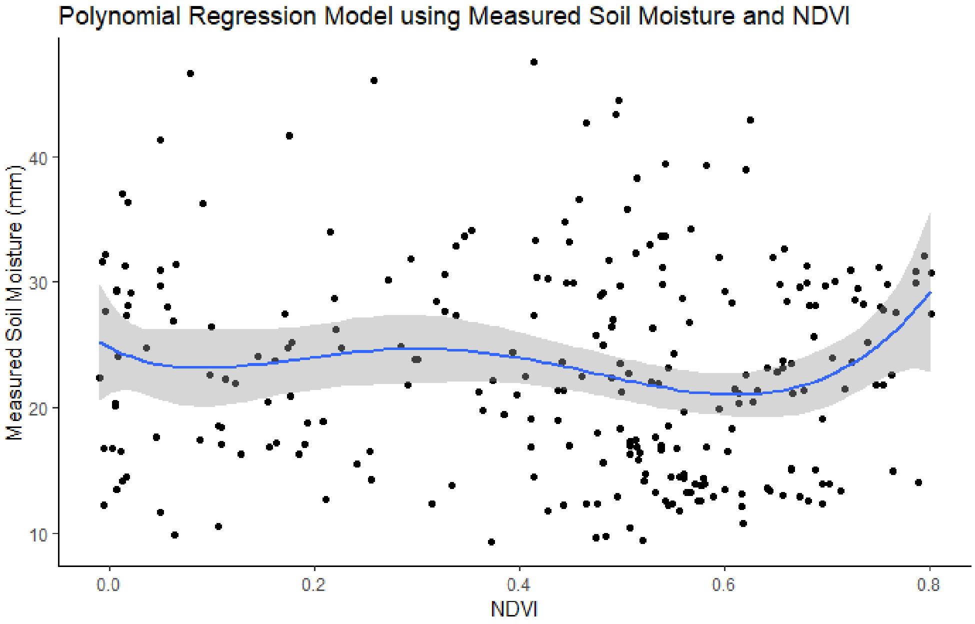

Figure 48: Polynomial Regression Model using Measured Soil Moisture and NDVI.

The RMSE of the model was 8.229, while the r^2 and the p-value were 0.016 and 0.099 respectively. The application of the model on the test dataset resulted in the following plot.

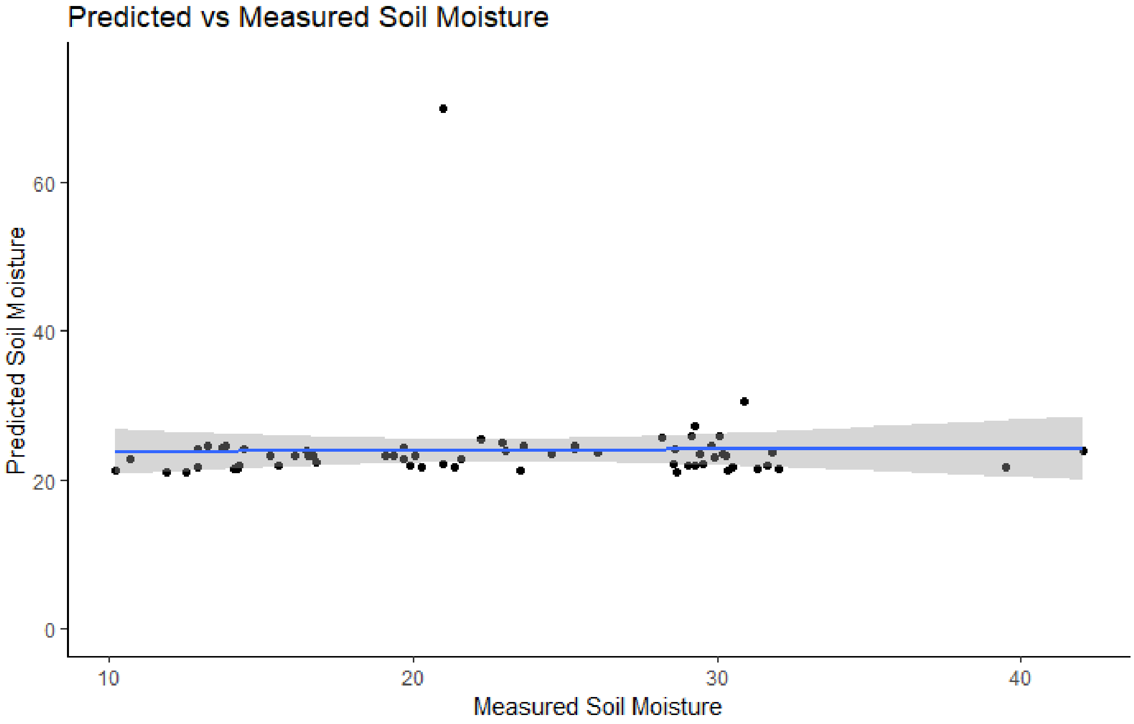

Figure 49: Predicted vs Measured Soil Moisture using Polynomial Regression Model and NDVI (n = 66 observations of the validation set).

Both the plots and the metrics, reveal that this model fitted poorly.

The next independent variable that was used was the NDMI. This time a second-order polynomial regression model was implemented. The visualization of the polynomial model using NDMI is presented below.

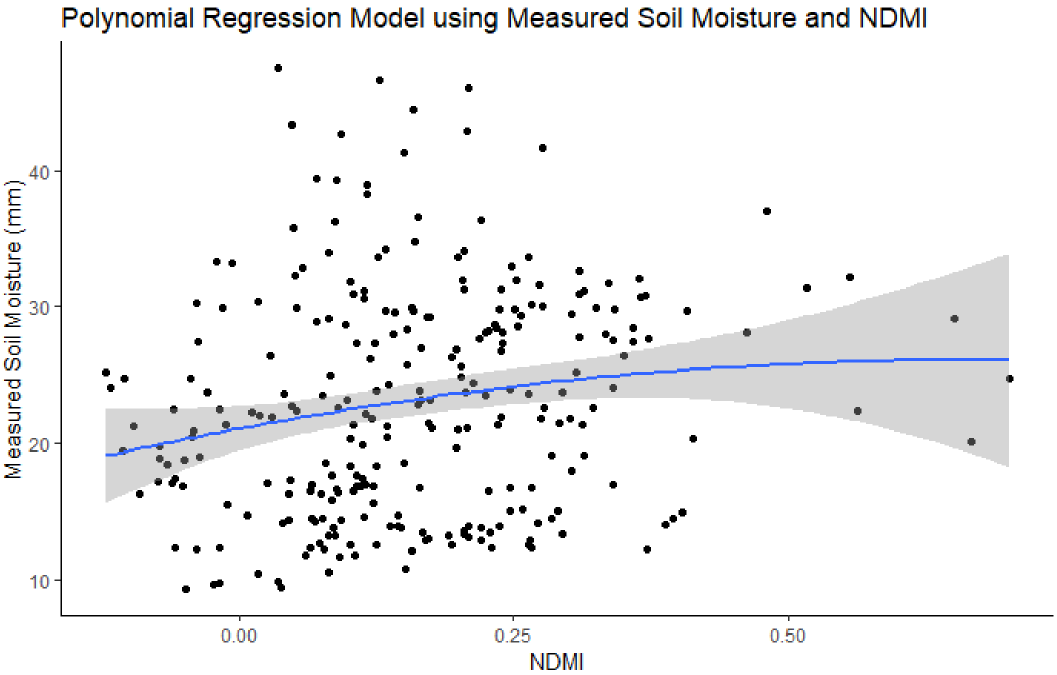

Figure 50: Polynomial Regression Model using Measured Soil Moisture and NDMI.

The RMSE of the model was 7.646 while the r^2 was 0.02. The p-value was 0.012, indicating a not statistically significant result. The following plot presents the comparison between the predicted soil moisture values and the measured ones, in order to evaluate the model.

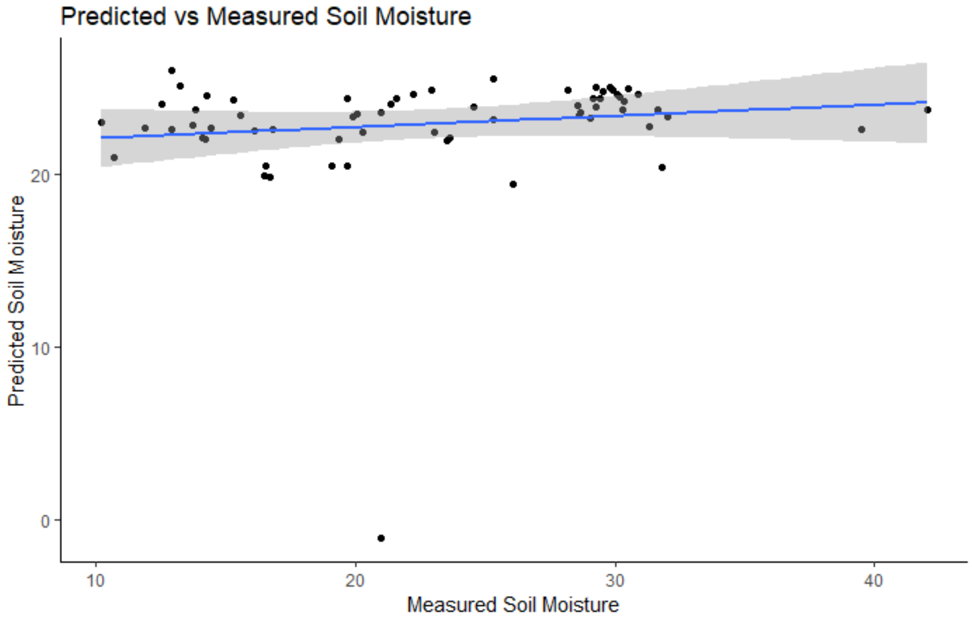

Figure 51: Predicted vs Measured Soil Moisture using Polynomial Regression Model and NDMI (n = 66 observations of the validation set).

Afterwards, the MI was used as independent variable in a third-order polynomial regression model. The RMSE and r^2 of the model were 7.273 and 0.038 respectively. The p-value was 0.00027, indicating a statistically significant result. The visualization of the model is presented below.

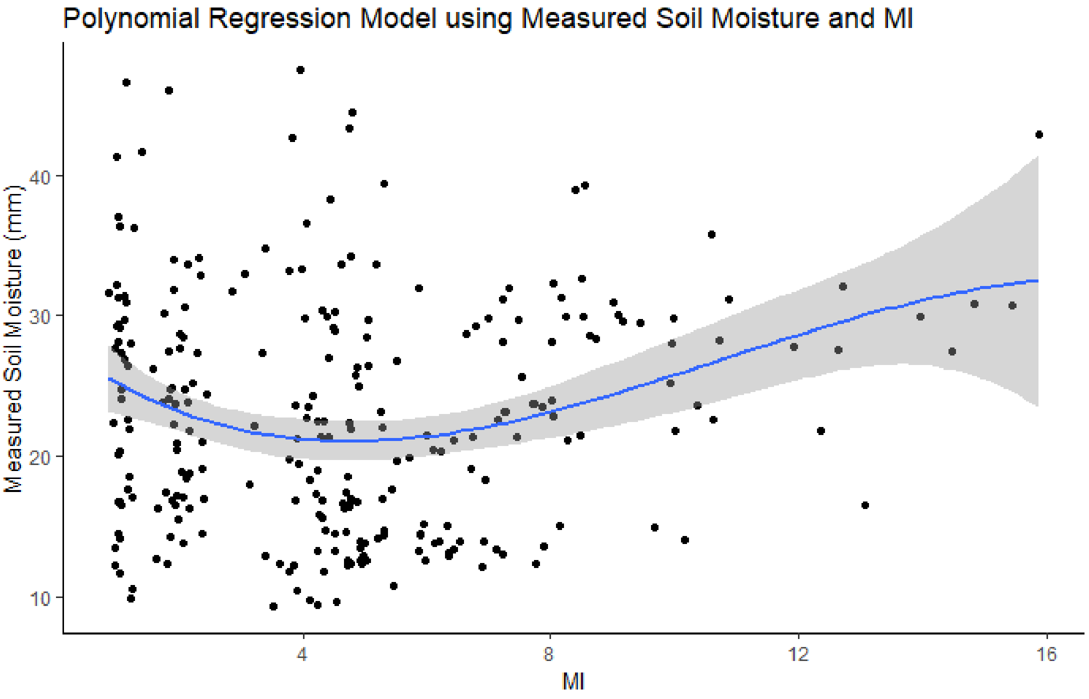

Figure 52: Polynomial Regression Model using Measured Soil Moisture and MI.

The results of the third-order polynomial model on the test dataset compared to the measured soil moisture values, can be evaluated by the following plot.

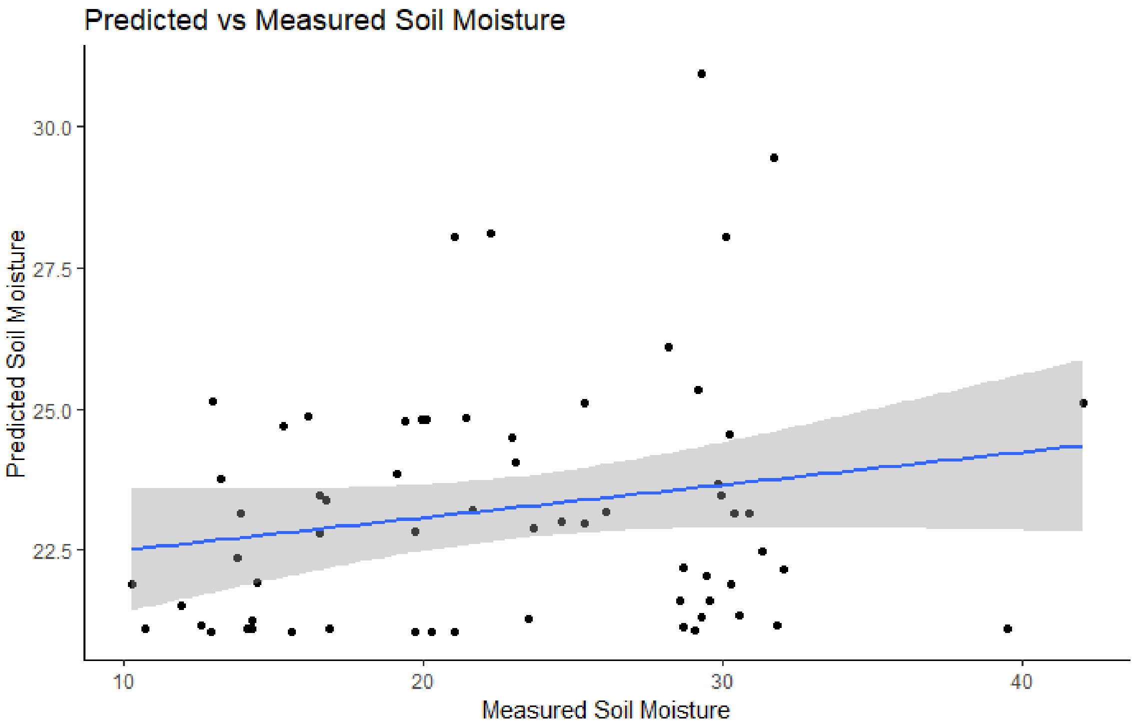

Figure 53: Predicted vs Measured Soil Moisture using Polynomial Regression Model and MI (n = 66 observations of the validation set).

As a next step, polynomial regression was also applied using the VV Backscattering as independent variable of the model. This variable appeared to produce better results than the previous ones while applying the polynomial model. The model that was applied was a third-order polynomial model and the resulting RMSE was 8.058 and the r^2 was 0.042.

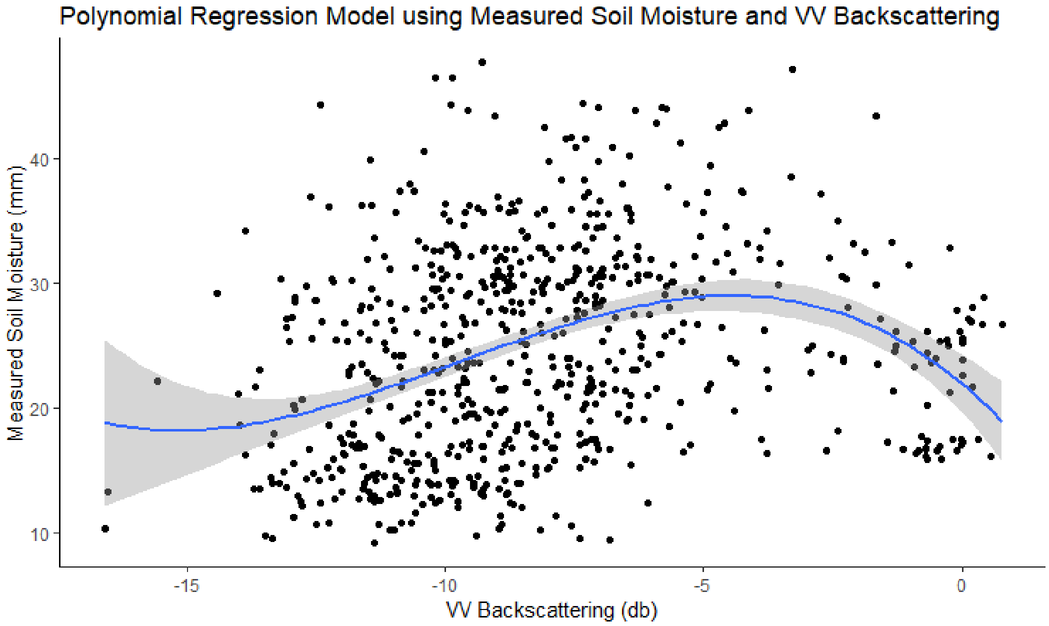

Figure 54: Polynomial Regression Model using Measured Soil Moisture and VV Backscattering.

After calculating the polynomial model equation, it was applied to the test dataset. The predicted and the measured soil moisture were compared and the result is presented in the following plot.

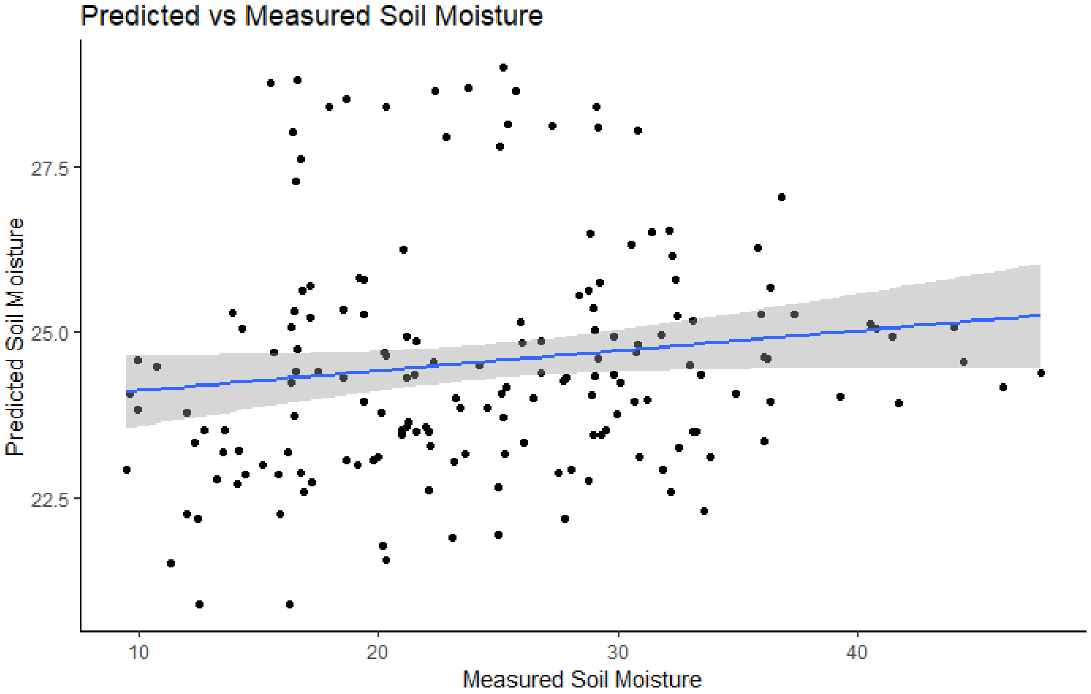

Figure 55: Predicted vs Measured Soil Moisture using Polynomial Regression Model and VV Backscattering (n = 173 observations of the validation set).

Apart from Linear Regression and Polynomial Regression Analysis, Generalized Additive Models were also implemented using each independent variable that was used in the previously implemented models.

Firstly, NDVI was used as the independent variable in the Generalized Additive Model. The resulting RMSE and r^2 were 7.441, 0.03 respectively. The model is presented in the following plot.

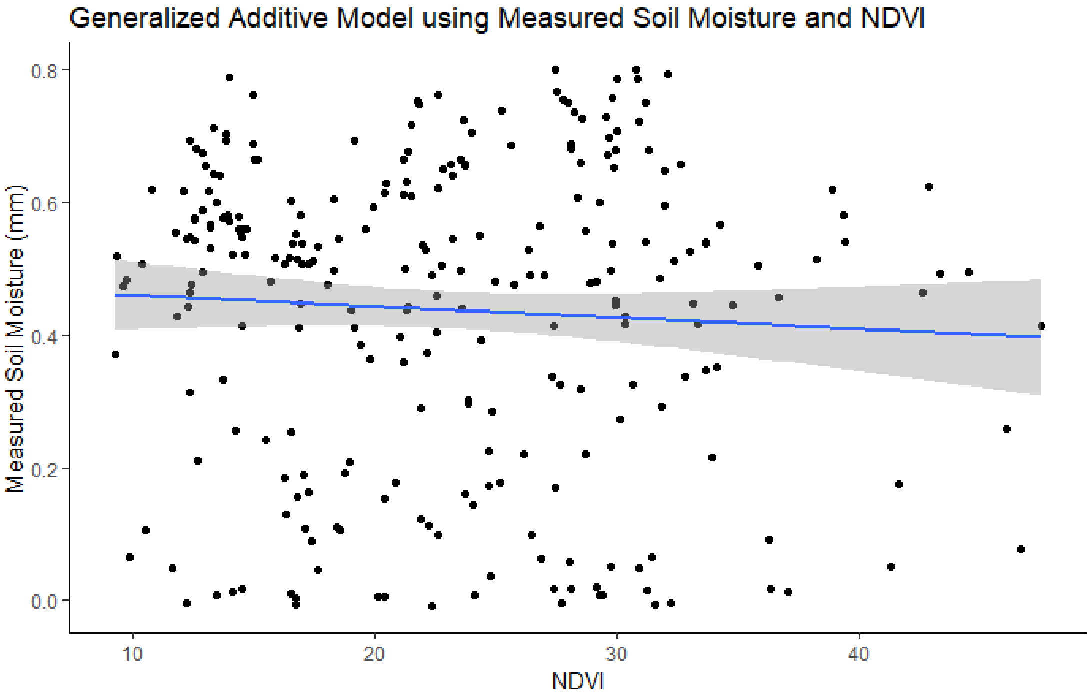

Figure 56: Generalized Additive Model using Measured Soil Moisture and NDVI.

In order to evaluate the model, the calculated model equation was applied to the test dataset and the results were compared to the measured soil moisture. The results are presented in the following plot.

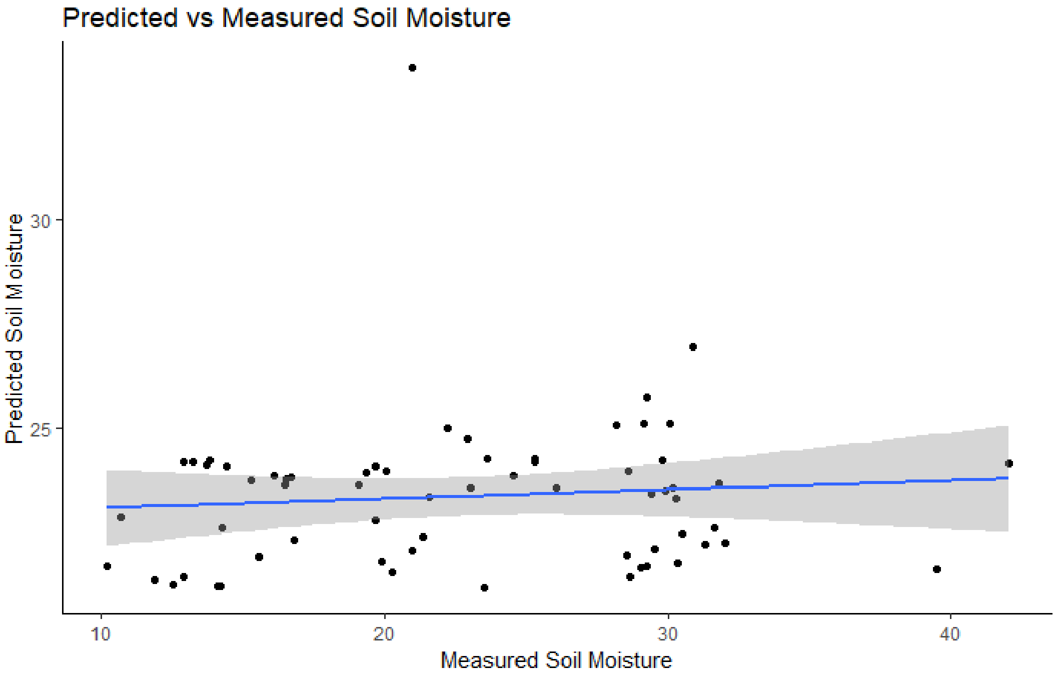

Figure 57: Predicted vs Measured Soil Moisture using Generalized Additive Models and NDVI (n = 66 observations of the validation set).

Afterwards, the same methodology was applied using the NDMI as the predictor variable of soil moisture. The RMSE of this model was 7.268 while the r^2 was 0.033. The resulting model is presented in the following plot.

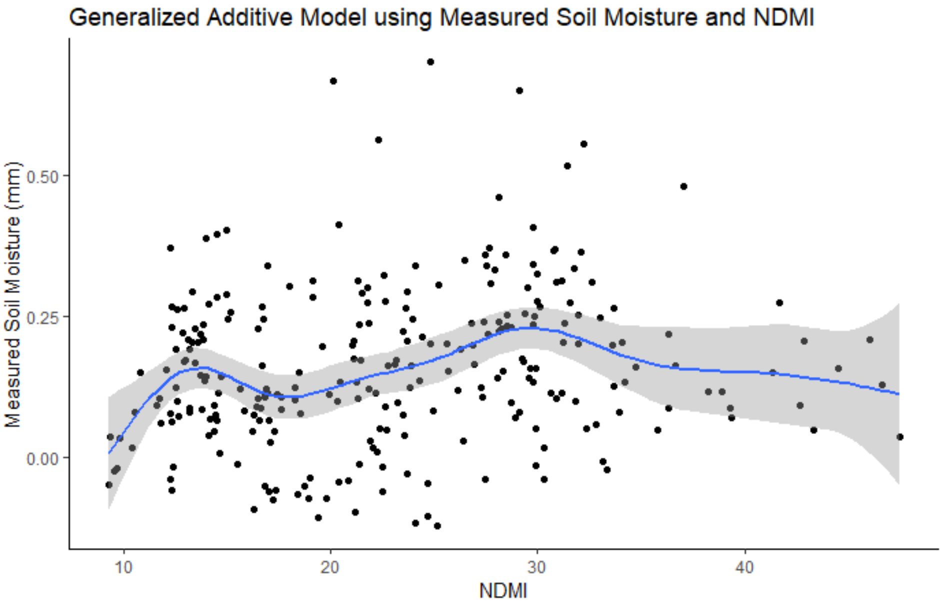

Figure 58: Generalized Additive Model using Measured Soil Moisture and NDMI.

The comparison of the measured and the predicted values of soil moisture seemed more successful than the previous two methodologies, as it can be observed in the following plot.

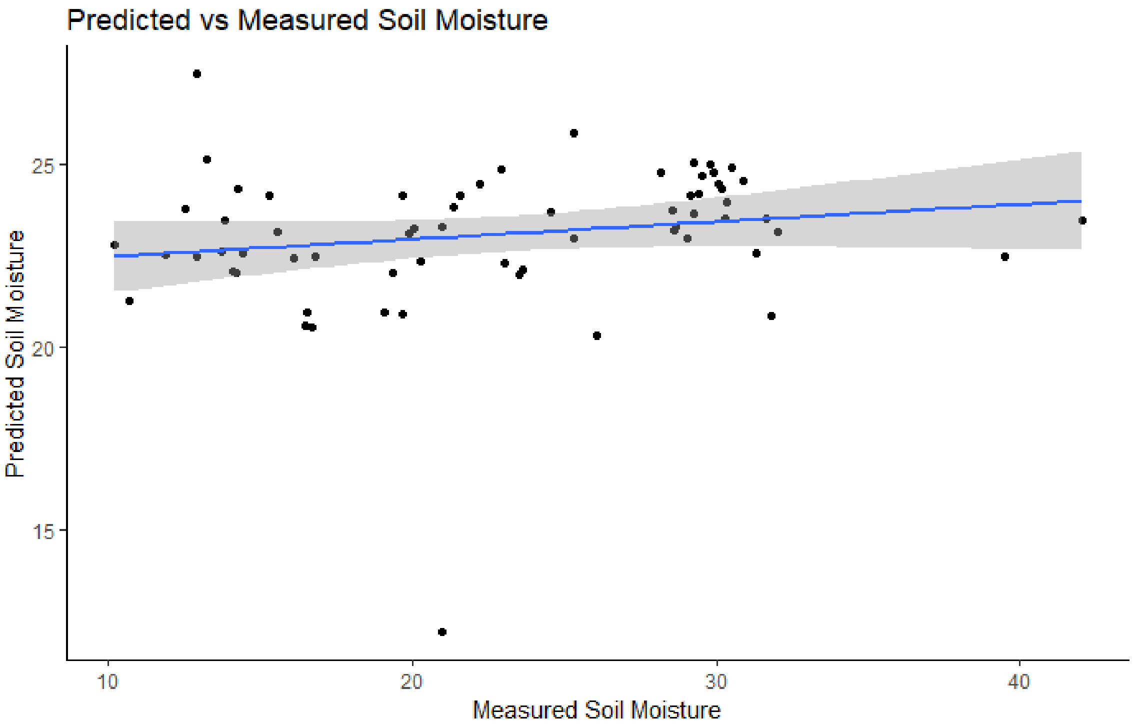

Figure 59: Predicted vs Measured Soil Moisture using Generalized Additive Models and NDMI (n = 66 observations of the validation set).

Generalized Additive Model was also applied using the MI as the independent variable which led to an RMSE value of 8.985 and an r^2 value of 0.085. The model is presented in the following plot.

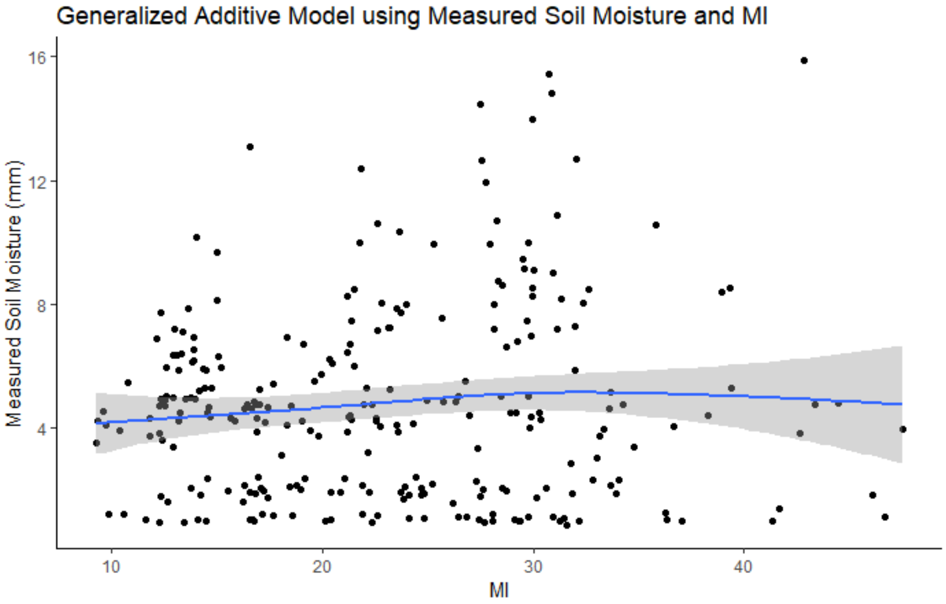

Figure 60: Generalized Additive Model using Measured Soil Moisture and MI.

After calculating the model, the evaluation of its performance took place by applying it to the test dataset. The comparison between the predicted and the measured soil moisture values was still satisfactory and can be observed in the following plot.

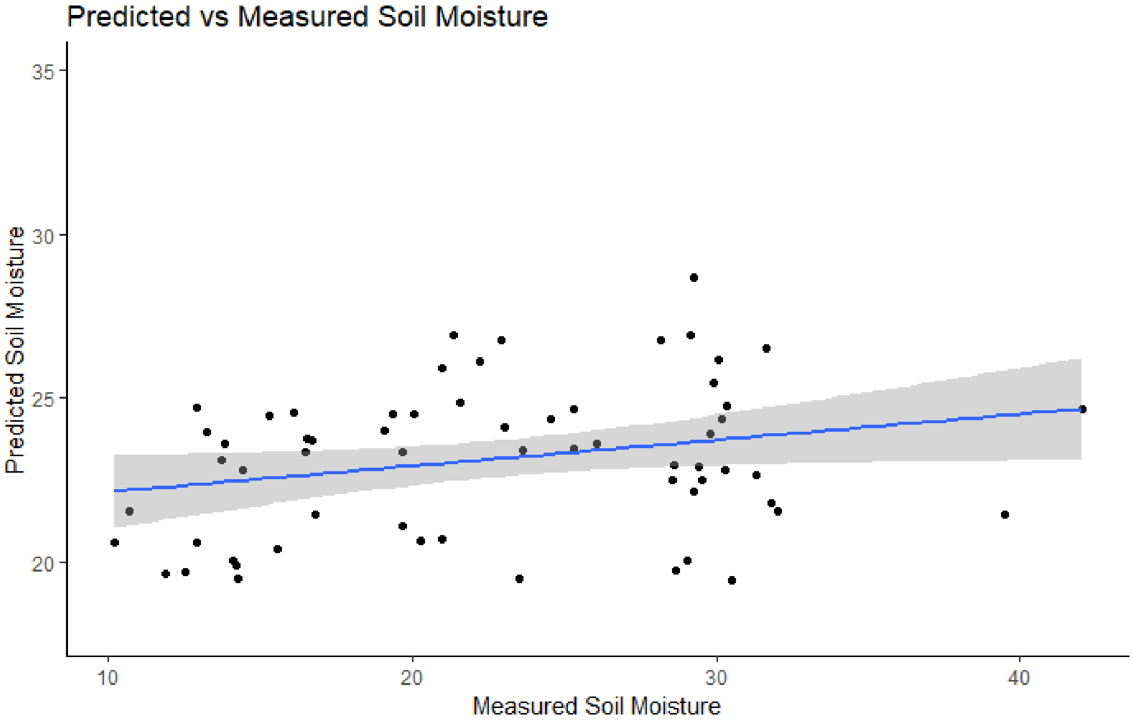

Figure 61: Predicted vs Measured Soil Moisture using Generalized Additive Models and MI (n = 66 observations of the validation set).

The Generalized Additive Model was also applied using the VV Backscattering information as the predictor of soil moisture. The resulting RMSE of the model was 7.79 while the r^2 was 0.12. The resulting model is presented below.

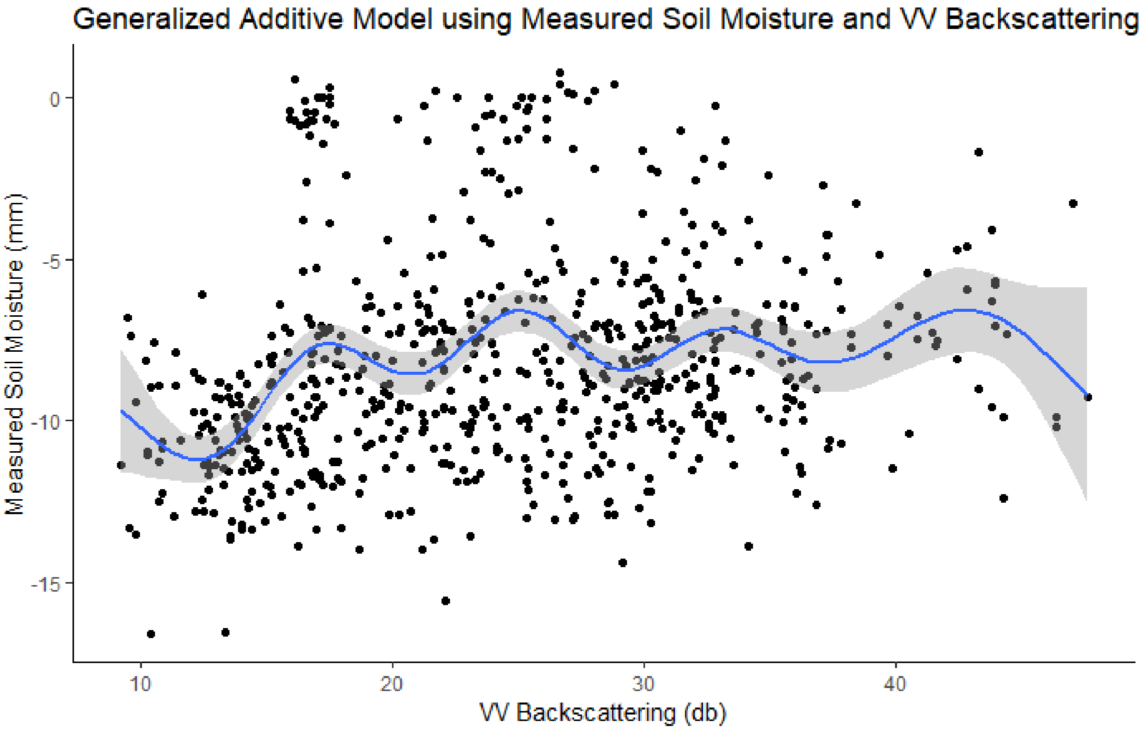

Figure 62: Generalized Additive Model using Measured Soil Moisture and VV Backscattering.

A comparison between the predicted and the measured soil moisture values was also performed and the results are presented in the following plot.

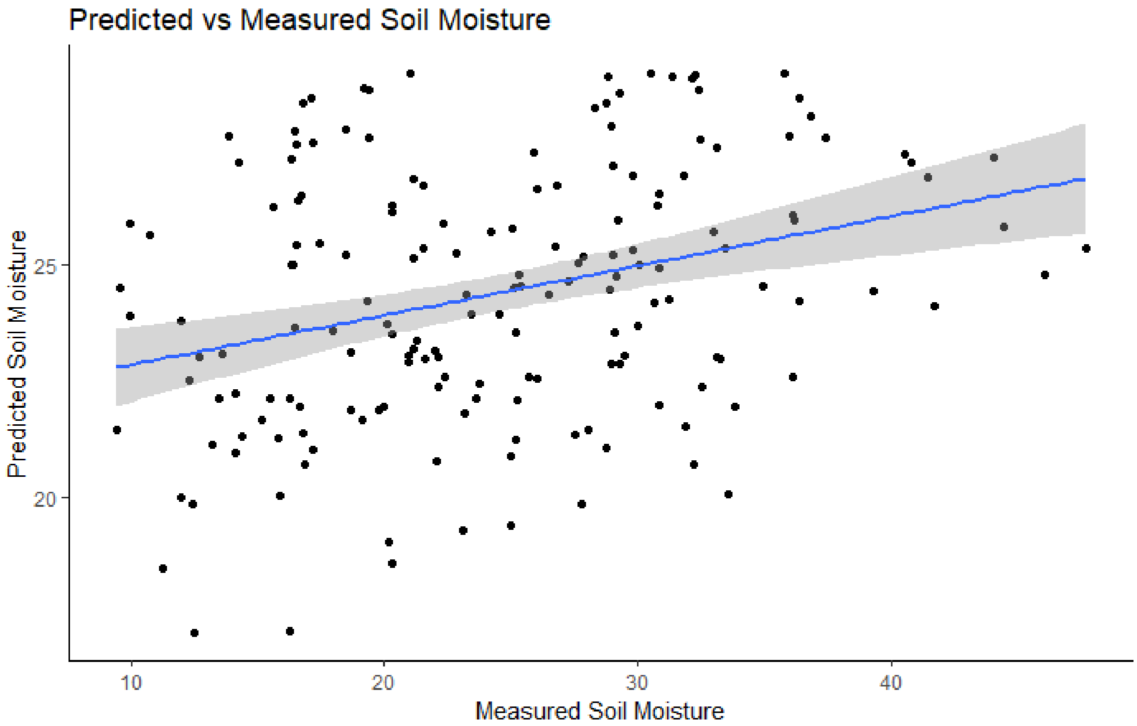

Figure 63: Predicted vs Measured Soil Moisture using Generalized Additive Models and VV Backscattering (n = 173 observations of the validation set).

Despite the low r^2 values, the Generalized Additive model appeared to fit better than the previous models in every case examined.

After executing the Linear Regression, the Polynomial Regression and the Generalized Additive Models, a Neural Network model was also developed. Using TensorFlow API along with Keras, better results were achieved compared to the package neuralnet. The training of the Neural Network was time consuming and based on trial and error, since there are no rules in terms of setting the numbers of hidden layers and neurons in order to achieve satisfactory results. This resulted in experimenting with the model parameters several times and going back and forth in the procedure until the output indicated that the parameters were right.

During the training of the network, the following two plots were produced.

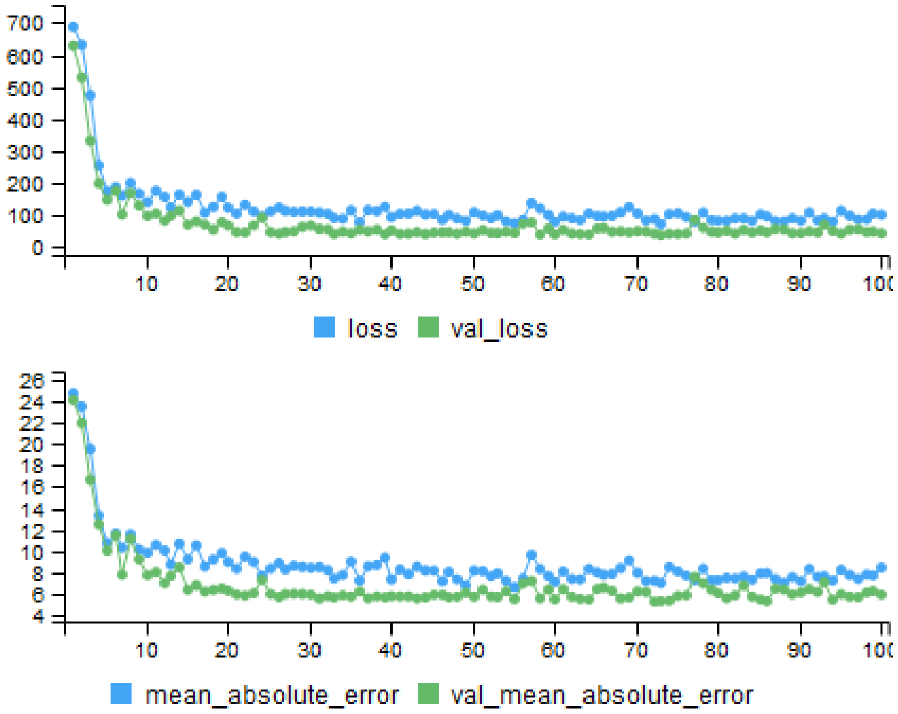

Figure 64: Performance plots of Artificial Neural Networks.

According to the first plot, the value of the loss function using the training set was really high at the beginning of the training process but it started decreasing fast. Since the 20th epoch the value seems to be stable with a slight decrease. The same observation was made on the test dataset too. However, the test dataset seems to achieve even lower loss function values.

Moreover, the Mean Absolute Error seemed to follow the same pattern. The training is initiated with a high MAE value, whereas until the 10th epoch it is being decreased dramatically. It becomes almost stable since the 20th epoch using both the training and the test datasets.

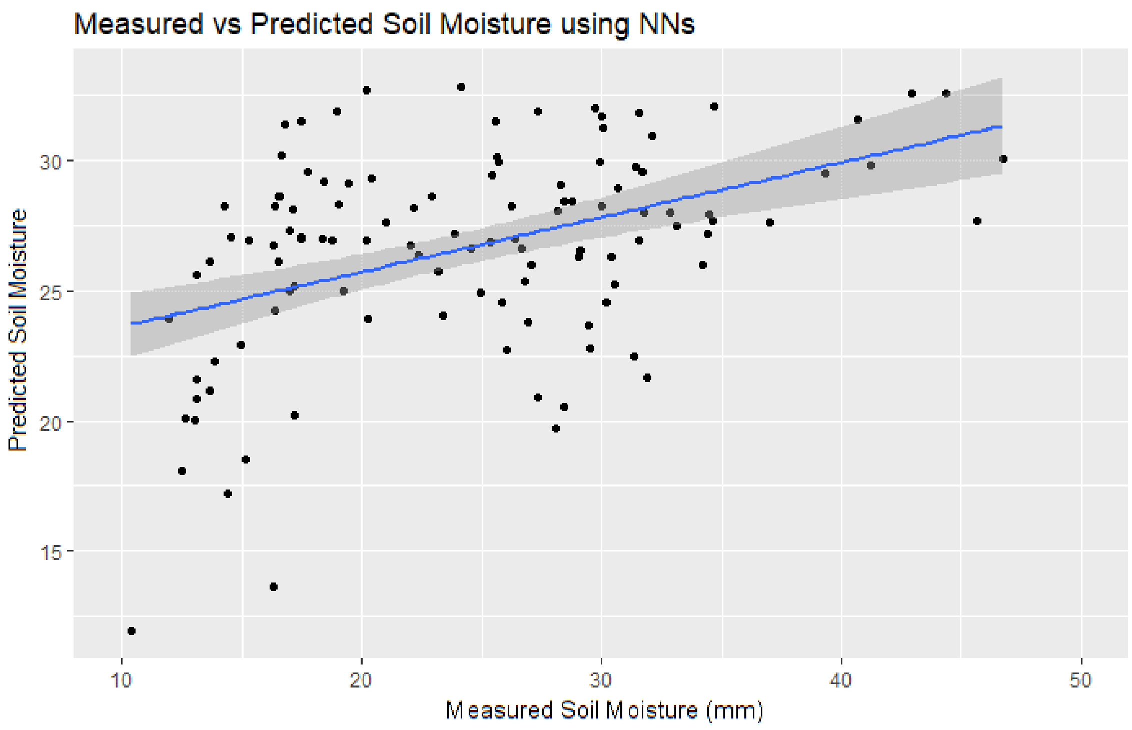

Figure 65: Predicted vs Measured Soil Moisture using Artificial Neural Networks, along with VV Backscattering and NDVI (plotted n = 114 observations of the full dataset).

As soon as the training process was completed, an evaluation of the model took place, by plotting and comparing the predicted Soil Moisture values with the measured ones. The model seemed to need further tuning thought the result was better than those of the previously mentioned methodologies. The RMSE was 6.204.

In the following table the metrics of all the applied models are presented.

Table 13: Comparison of the results of the applied methodologies.

Linear Regression			
Predictor	**RMSE**	**r^2**	**p-value**
NDVI	7.479	0.04	0.33
NDMI	7.268	0.033	0.004
MI	7.222	0.043	0.1549
VV Backscattering	8.058	0.043	0.00000006
Polynomial Regression			
NDVI	8.229	0.016	0.099
NDMI	7.646	0.02	0.012
MI	7.273	0.038	0.00027
VV Backscattering	8.058	0.042	0.0000000000000022
Generalized Additive Models			

NDVI	7.441	0.03	-
NDMI	7.268	0.033	-
MI	8.985	0.085	-
VV Backscattering	7.79	0.12	-
Artificial Neural Network			
NDVI + VV Backscattering	6.204		

According to the table above NDVI did not produce well-fitted models in any applied method, NDMI produced more satisfactory results in Linear Regression and MI produced good results in the Polynomial Regression and Generalized Additive Models but the RMSE of the last-mentioned technique was too high, indicated high mean deviation between the measured and the predicted soil moisture values. VV Backscattering appeared to produce the most satisfactory results among all the predictors, especially in Generalized Additive Models, the use of VV Backscattering as the independent variable resulted in an r^2 value of 0.12 and an RMSE value that indicated a mean deviation of +/-7.79 mm between the measured and the predicted soil moisture values (sample size, n=865). Moreover, the neural network that was applied using NDVI and VV Backscattering, resulted in an RMSE value which revealed a mean deviation of +/-6.204 mm between the measured and the estimated soil moisture values (sample size, n=114), which is better than the RMSEs produced by the previously implemented models.

5 DISCUSSION

The aim of this study was to examine the correlation between soil moisture In-Situ measurements and the indices derived by Landsat 8 surface Reflectance data along with Sentinel 1 Images, by applying Statistical and Machine Learning Techniques. Moreover, this study showcases the capabilities and advantages of using the Google Earth Engine. During the course of this study, several limitations showed up which should be mentioned, along with several useful findings. It is worth mentioning that using Google Earth Engine in order to process Remote Sensing data makes processing time extremely less, as the data are already preprocessed up to a specific point. Its usage also helps saving time as the processing is not being executed locally but using large remote CPUs. This decreased computational time dramatically. It should be noted though that, in spite the fact that a high-level programming language is used, good programming skills are highly required in order to fully understand all the functions and use them efficiently, but also to be able to customize and create new ones which would be fully adapted to each research question. The documentation provided by Google is complete with really good and helpful examples, but the lack of programming skills could make them confusing or incomprehensible as well as difficult to customize. One more thing that can make the life of a scientist using Google Earth Engine easier, is the existence of the Google Earth Engine Developers' List. In this group, experts of Google Earth Engine and other scientists discuss related topics but also answer to many questions in detail.

Except for Sentinel 1 and Landsat 8 Surface Reflectance, Sentinel 2 data were also queried. However, they are not atmospherically corrected and no atmospheric correction algorithm for S2 products is still implemented in Google Earth Engine. So, in order to avoid downloading this dataset and processing the images using another tool, the S2 Images were not used.

After processing the data in Google Earth Engine though, the retrieved values should be exported in .csv format as, unfortunately, there is still no implementation for Neural Network applications in Google Earth Engine. This is something highly asked by the Google Earth Engine community which will probably be implemented in the near future. At this point the results were exported from Google Earth Engine and implemented in R statistical package. R is a user friendly and easy to learn programming language with many capabilities. In the R environment, several machine learning techniques were executed, including Linear Regression, Polynomial Regression and Generalized Additive Models. The computation of these models led to extremely low r^2 values, along with low p-values. The observed RMSEs thought were not bad considering the value range of soil moisture. After examining the aforementioned methodologies, a Deep Learning technique was also implemented using TensorFlow and Keras. The installation of Keras though was more time consuming than expected though as there was a bug in the installation process and the solution was not straightforward. Moreover, the creation of a neural network is a time-consuming process, as it implies trial and error when it comes to determining its architecture parameters. Despite that, neural networks are a powerful Deep Learning technique. The results of this technique appeared to be more satisfactory than those of the previously implemented techniques.

It should be noted though that, despite the literature, none of the combinations of the implemented statistical and machine learning models, managed to produce satisfactory correlation results. However, Álvarez-Mozos et al., (2005) also observed low point scale correlations[1] between soil moisture and backscattering coefficient, with r^2 values ranging between 0.25 and 0.37. This could be due to the heterogeneity of the dataset by means of different In-Situ measuring instruments as well as the different properties of each station. Alexakis et al., (2017) applied Artificial Neural Networks on a sample of 640 measurements, consisting of the following variables as inputs: backscattering coefficient, NDVI, Thermal Infrared Temperature values and incidence angle θ, derived by Sentinel 1 and Landsat 8 data, and they observed r^2 values ranging between 0.400 and 0.914 and RMSE values which indicated a mean offset ranging between 0.022 $m^3\ m^{-3}$ and 0.058 $m^3\ m^{-3}$ [2] between the measured and the predicted soil moisture content values. In the current study, the results of the Deep Neural Network that was implemented were the most satisfactory ones but the values of the r^2 were lower than the ones reported from Alexakis et al..

In a future related research, more indices could be used in order to estimate soil moisture, such as the combination of Surface Temperature and NDVI in order to retrieve the Soil Moisture Index. Also, models per station could be implemented to overcome the limitations that the heterogenous data caused as well. Models per dry and rainy seasons could also be estimated. It could be considered a good practice to calculate the mean of a 5x5 pixels’ kernel as the independent variables’ value instead of the individual pixel’s value. Moreover, Soil Moisture products could be used as validation datasets along with the In-Situ measurements. Last but not least, the use of Sentinel 2 could be an interesting addition in the examination of the soil moisture estimation.

---

[1] In the research mentioned (Alvarez et al., 2005), point, field and catchment scale correlations where implemented.

[2] Referring to the Soil Moisture Content.

6 CONCLUSION

The purpose of this study was to examine the correlations between soil moisture In-Situ measurements and indices, derived by multispectral data, as well as VV Backscattering values, derived by SAR Images, by applying statistical and machine learning techniques. The data that were used included Landsat 8 Surface Reflectance and Sentinel 1 Images. Firstly, In-Situ data were collected from the Enhydris project, were soil moisture measurements from 6 stations were found. The stations where soil moisture was measured were Agios Spyridonas, Kommeno, Kompoti, Kampi, TEI Epirus – Kostakii and TOEB Lourou and they were located in the broader region of Arta. Having the In-Situ data, the satellite data where chosen through Google Earth Engine, which appeared to be an extremely helpful and time-saving tool. When all the images were processed, the values of NDVI, NDMI, MI on each point location were extracted, using the Landsat 8 data, as well as the VV Backscattering values of the stations' points, using the Sentinel 1 Images. Those data along with the In-Situ measurements were imported in R, where they were processed and merged. The resulting dataset included information of the NDVI, NDMI, MI, VV Backscattering and In-Situ Soil Moisture of each station.

The first technique that was applied was Linear Regression using soil moisture as dependent variable and each time one of the rest parameters (NDVI, NDMI, MI, VV Backscattering) as independent variables. In Linear Regression, the best results were produced when using VV Backscattering as an independent variable as well as NDMI. The Linear Regression using VV Backscattering as the predictor resulted in an extremely low p-value, the highest r^2 in comparison to the other variables, though still low, and an RMSE indicating a mean deviation of +/-8.058 mm between the measured and the estimated soil moisture values (sample size, n=865), which was higher than those of the other variables. In Polynomial Regression, VV Backscattering (sample size, n=865) and MI (sample size, n=328) produced the best models with RMSE values revealing mean deviations of +/-8.058 mm and +/-7.273 mm, respectively, between the measured and the predicted soil moisture values, r^2 values of 0.042 and 0.038 respectively and p-values of 0.00000000000000022 and 0.00027 respectively. Generalized Additive Models produced better results when VV Backscattering (sample size, n=865) was used as the predictor with an RMSE value indicating a mean deviation of +/-7.79 mm between the measured and the predicted soil moisture values and an r^2 value of 0.12.

The models that were implemented using statistical and machine learning techniques, did not manage to reveal strong correlations between the examined data. The main reason of this problem could be the heterogeneity of the data, since the instruments of the In-Situ stations as well as the environmental properties of each station were different.

Evaluating the results of each predictor, it was observed that NDVI did not perform well as a sole predictor of soil moisture in any of the applied statistical and machine learning techniques whereas NDMI produced better results in Linear Regression model. Moreover, the use of MI as the predictor was found effective when Polynomial Regression but also Generalized Additive Models were applied. However, the RMSE of the application of Generalized Additive Models using MI was too high, indicating a high mean deviation between the measured and the predicted soil moisture values. As long as VV Backscattering is concerned, using it as the sole predictor led to the most efficient results and the best fitted models, in comparison to the other predictors. Especially the application of Generalized Additive Model using VV Backscattering as the independent variable, resulted in the highest r^2 value of 0.12 and an RMSE value indicating a mean deviation of +/-7.79 mm between the measured and the predicted soil moisture values (sample size, n=865).

Last but not least, the application of the neural network model using NDVI and VV Backscattering as independent variables, led to an RMSE value revealing a mean deviation of +/-6.204 mm between the measured and the predicted soil moisture (sample size, n=114), which was the lowest RMSE value observed among all the previously implemented models.

7 REFERENCES

- Abadi, M., Barham, P., Chen, J., Chen, Z., Davis, A., Dean, J., Devin M., Ghemawat S., Irving G., Isard M., Kudlur M.. (2016, November). Tensorflow: a system for large-scale machine learning. *OSDI* (Vol. 16, pp. 265-283).

- Ahmad, M. F., Runping, S., & Jing, Y. (2012). Soil Moisture Retrieval through Satellite Data for Gansu and Xinjiang Region of China. Pakistan Journal of Meteorology, 9(17).

- Akinremi, O. O., & McGinn, S. M. (1996). Usage of soil moisture models in agronomic research. *Canadian journal of soil science, 76(3)*, 285-295.

- Alexakis, D. D., Mexis, F. D. K., Vozinaki, A. E. K., Daliakopoulos, I. N., & Tsanis, I. K. (2017). Soil moisture content estimation based on Sentinel-1 and auxiliary earth observation products. A hydrological approach. *Sensors, 17(6)*, 1455.

- Altobelli, A., Feoli, E., Napoletano, R., & Cinco, M. (2001). Remote sensing/GIS technique for risk assessment of Borrelia burgdorferi infection. *The Geomatics Workbook*.

- Álvarez-Mozos, J., Casalí, J., González-Audícana, M., & Verhoest, N. E. (2005). Correlation between ground measured soil moisture and RADARSAT-1 derived backscattering coefficient over an agricultural catchment of Navarre (North of Spain). *Biosystems Engineering, 92(1)*, 119-133

- AWMB. (2014). Amvrakikos Wetlands Management Body Web site. Available at: http://www.amvrakikos.eu.

- Baup, F., Mougin, E., de Rosnay, P., Timouk, F. and Chênerie, I. (2007). Surface soil moisture estimation over the AMMA Sahelian site in Mali using ENVISAT/ASAR data. *Remote Sensing of Environment, 109(4)*, pp.473-481.

- Brocca, L., Hasenauer, S., Lacava, T., Melone, F., Moramarco, T., Wagner, W., Dorigo, W., Matgen, P., Martínez-Fernández, J., Llorens, P., Latron, J., Martin, C. and Bittelli, M. (2011). Soil moisture estimation through ASCAT and AMSR-E sensors: An intercomparison and validation study across Europe. *Remote Sensing of Environment, 115(12)*, pp.3390-3408.
- Chollet & Allaire (2017, Dec. 20). TensorFlow for R: Time Series Forecasting with Recurrent Neural Networks. Retrieved from

https://blogs.rstudio.com/tensorflow/posts/2017-12-20-time-series-forecasting-with-recurrent-neural-networks/

- Christofides A, Kozanis S, Karavokiros G, Koukouvinos A (2011a) Enhydris, Filotis & openmeteo.org: free software for environmental management, *FLOSS conference 2011, Athens*, http://conferences.ellak.gr/2011/, 2011.

- Christofides, A., Kozanis, S., Karavokiros, G., Markonis, Y., & Efstratiadis, A. (2011b). Enhydris: A free database system for the storage and management of hydrological and meteorological data. *European Geosciences Union General Assembly Geophysical Research Abstracts, 13*. European Geosciences Union, Vienna.

- Dancho (2018, Jan. 11). TensorFlow for R: Deep Learning With Keras To Predict Customer Churn. Retrieved from https://blogs.rstudio.com/tensorflow/posts/2018-01-11-keras-customer-churn/.

- Dente, L. (2016). Microwave remote sensing for soil moisture monitoring: synergy of active and passive observations and validation of retrieved products.

- Dupigny-Giroux, L. A., & Lewis, J. E. (1999). A moisture index for surface characterization over a semiarid area. *Photogrammetric Engineering and Remote Sensing, 65,* 937-946.

- EEA, 2014. Amvrakikos Wetlands National Park. Available at: http://natura2000.eea.europa.eu/natura2000/SDF.aspx?site=GR2110004

- EKBY, 2014. Amvrakikos Wetlands National Park. Available at: http://www.ekby.gr/ekby/en/EKBY_Natura2000_en.html.

- El Hajj, M., Baghdadi, N., Zribi, M., Belaud, G., Cheviron, B., Courault, D. and Charron, F. (2016). Soil moisture retrieval over irrigated grassland using X-band SAR data. Remote Sensing of Environment, 176, pp.202-218.

- ESRI, E. (1998). Shapefile technical description. *An ESRI White Paper*.

- Famiglietti, J. S., Rudnicki, J. W., & Rodell, M. (1998). Variability in surface moisture content along a hillslope transect: Rattlesnake Hill, Texas. *Journal of Hydrology, 210(1-4)*, 259-281.

- Gao, B. C. (1996). NDWI—A normalized difference water index for remote sensing of vegetation liquid water from space. *Remote sensing of environment, 58(3)*, 257-266.

- GCOS (2010) Implementation Plan for the Global Observing System for Climate and Support of the UNFCCC, GCOS-138. *In, GCOS Reports* (p. 180). http://www.wmo.int/pages/prog/gcos/Publications.

- Gherboudj, I., Magagi, R., Berg, A. and Toth, B. (2011). Soil moisture retrieval over agricultural fields from multi-polarized and multi-angular RADARSAT-2 SAR data. Remote Sensing of Environment, 115(1), pp.33-43.

- Goldsborough, P. (2016). A tour of tensorflow. arXiv preprint arXiv:1610.01178.

- Gonzalez, H., Halevy, A., Jensen, C. S., Langen, A., Madhavan, J., Shapley, R., & Shen, W. (2010, June). Google fusion tables: data management, integration and collaboration in the cloud. *In Proceedings of the 1st ACM symposium on Cloud computing* (pp. 175-180). ACM.

- Gorelick, N., Hancher, M., Dixon, M., Ilyushchenko, S., Thau, D., & Moore, R. (2017). Google Earth Engine: Planetary-scale geospatial analysis for everyone. Remote Sensing of Environment.

- Halevy, A., & Shapley, R. (2009). Google fusion tables. Research Blog, June, 9.

- Hinton, G., Srivastava, N., & Swersky, K. (2012). Rmsprop: Divide the gradient by a running average of its recent magnitude. Neural networks for machine learning, Coursera lecture 6e.

- Ihaka, R., & Gentleman, R. (1996). R: a language for data analysis and graphics. *Journal of computational and graphical statistics, 5(3)*, 299-314.

- Kallio, J. (2017). Support Vector Machine and Deep Learning in Medical Applications *(Master's thesis)*.

- Kolassa, J., Gentine, P., Prigent, C. and Aires, F. (2016). Soil moisture retrieval from AMSR-E and ASCAT microwave observation synergy. Part 1: Satellite data analysis. Remote Sensing of Environment, 173, pp.1-14.

- Kolassa, J., Reichle, R., Liu, Q., Alemohammad, S., Gentine, P., Aida, K., Asanuma, J., Bircher, S., Caldwell, T., Colliander, A., Cosh, M., Holifield Collins, C., Jackson, T., Martínez-Fernández, J., McNairn, H., Pacheco, A., Thibeault, M. and Walker, J. (2018). Estimating surface soil moisture from SMAP observations using a Neural Network technique. Remote Sensing of Environment, 204, pp.43-59.

- Lakhankar, T., Ghedira, H., Temimi, M., Sengupta, M., Khanbilvardi, R. and Blake, R. (2009). Non-parametric Methods for Soil Moisture Retrieval from Satellite Remote Sensing Data. Remote Sensing, 1(1), pp.3-21.

- Legates, D. R., Mahmood, R., Levia, D. F., DeLiberty, T. L., Quiring, S. M., Houser, C., & Nelson, F. E. (2011). Soil moisture: A central and unifying theme in physical geography. *Progress in Physical Geography, 35(1)*, 65-86.

- Liu, Q., Reichle, R. H., Bindlish, R., Cosh, M. H., Crow, W. T., De Jeu, R., ... & Jackson, T. J. (2011). The contributions of precipitation and soil moisture observations to the skill of soil moisture estimates in a land data assimilation system. *Journal of Hydrometeorology, 12(5)*, 750-765.

- Magagi, R. and Kerr, Y. (2001). Estimating surface soil moisture and soil roughness over semiarid areas from the use of the copolarization ratio. Remote Sensing of Environment, 75(3), pp.432-445.

- Malamos, N., Tsirogiannis, I. L., Christofides, A., Anastasiadis, S., & Vanino, S. (2015). Main Features and Application of a Web-based Irrigation Management Tool for the Plain of Arta. *In HAICTA* (pp. 174-185).
- R Core Team (2014). R: A language and environment for statistical computing. R Foundation for Statistical Computing, Vienna, Austria. URL http://www.R-project.org/.

- Ramsar Convention (2014). Amvrakikos gulf 3GR009 site No61. Available at: http://ramsar.wetlands.org/Database/SearchforRamsarsites/tabid/765/Default.aspx.

- Rigas Y., Petrou N., Zogaris S. (2003). Amvrakikos nowhere else on earth. Koan Editions, Athens.

- Rotich, N. (2014). Forecasting of wind speeds and directions with artificial neural networks.

- Rouse, J. W., Haas, R. H., Schell, J. A., Deering, D. W., & Harlan, J. C. (1974). Monitoring the vernal advancement of retrogradation of natural vegetation, *NASA/GSFC, Type III, Final Report*. Greenbelt, MD, 371.

- Santi, E., Paloscia, S., Pettinato, S., Brocca, L., Ciabatta, L. and Entekhabi, D. (2018). On the synergy of SMAP, AMSR2 AND SENTINEL-1 for retrieving soil moisture. International Journal of Applied Earth Observation and Geoinformation, 65, pp.114-123.

- Sharma, S. (2006). Soil moisture estimation using active and passive microwave remote sensing techniques. *Andhra University, Indian Institute of Remote Sensing*, Dehradun, India.

- Snoeij, P., Attema, E., Davidson, M., Duesmann, B., Floury, N., Levrini, G., Rommen B., Rosich, B. (2009, October). The Sentinel-1 radar mission: status and performance. *In Radar Conference-Surveillance for a Safer World, 2009. RADAR. International (pp. 1-6)*. IEEE.

- Srivastava, N., Hinton, G., Krizhevsky, A., Sutskever, I., & Salakhutdinov, R. (2014). Dropout: a simple way to prevent neural networks from overfitting. *The Journal of Machine Learning Research, 15(1),* 1929-1958.

- Tsirogiannis, I. L., Karras, G., Tsolis, D., & Barelos, D. (2015). Irrigation and Drainage Scheme of the Plain of Arta–Effects on the Rural Landscape and the Wetlands of Amvrakikos' Natura Area. *Agriculture and agricultural science procedia, 4*, 20-28.

- van der Velde, R., Su, Z., van Oevelen, P., Wen, J., Ma, Y. and Salama, M. (2012). Soil moisture mapping over the central part of the Tibetan Plateau using a series of ASAR WS images. Remote Sensing of Environment, 120, pp.175-187.

- Vermote, E., Justice, C., Claverie, M., & Franch, B. (2016). Preliminary analysis of the performance of the Landsat 8/OLI land surface reflectance product. *Remote Sensing of Environment, 185*, 46-56.

- Verstraeten, W., Veroustraete, F., van der Sande, C., Grootaers, I. and Feyen, J. (2006). Soil moisture retrieval using thermal inertia, determined with visible and thermal spaceborne data, validated for European forests. Remote Sensing of Environment, 101(3), pp.299-314.

- Wagner, W., Lemoine, G. and Rott, H. (1999). A Method for Estimating Soil Moisture from ERS Scatterometer and Soil Data. Remote Sensing of Environment, 70(2), pp.191-207.

- Wang, X., Xie, H., Guan, H., & Zhou, X. (2007). Different responses of MODIS-derived NDVI to root-zone soil moisture in semi-arid and humid regions. *Journal of hydrology, 340(1-2)*, 12-24.

- Wang, L., & Qu, J. J. (2009). Satellite remote sensing applications for surface soil moisture monitoring: A review. Frontiers of Earth Science in China, *3(2)*, 237-247.

- Wang, D., Huang, P., Huang, M. and Liu, A. (2013). Simple algorithm for soil moisture retrieval with co-polarized SAR data. Journal of Electronics (China), 30(3), pp.237-242.

- Wang, H., Magagi, R. and Goita, K. (2017). Comparison of different polarimetric decompositions for soil moisture retrieval over vegetation covered agricultural area. Remote Sensing of Environment, 199, pp.120-136.

- Zhang, T., Wen, J., Su, Z., Velde, R., Timmermans, J., Liu, R., Liu, Y. and Li, Z. (2009). Soil moisture mapping over the Chinese Loess Plateau using ENVISAT/ASAR data. Advances in Space Research, 43(7), pp.1111-1117.

- Zhao, Y., Tang, J., Graham, C., Zhu, Q., Takagi, K., & Lin, H. (2012). Hydropedology in the Ridge and Valley: Soil Moisture Patterns and Preferential Flow Dynamics in Two Contrasting Landscapes. *In Hydropedology (pp. 381-411). Elsevier*. DOI: 10.1016/B978-0-12-386941-8.00012-5.

7.1 WEB PAGES

- Arta Irrigation Management – IRMA, http://arta.irrigation-management.eu
- European Space Agency – Sentinel, https://sentinel.esa.int
- Google Earth Engine,
- Jove, https://www.jove.com
- Keras Documentation, keras.io
- Satellite Imaging Corporation, https://www.satimagingcorp.com
- USGS – Landsat , https://landsat.usgs.gov
- https://www.cs.ccu.edu.tw/~wylin/BA/Fusion_of_Biometrics_II.ppt
- https://towardsdatascience.com

APPENDICES

APPENDIX A – Sentinel 1 Metadata of the Selected Images

Date	Instrument	Instrument Mode	Platform	Product Class	Product Type	Orbit Pass	Relative Orbit	Resolution	Transmitter Receiver Polarisation
2015-03-04	Synthetic Aperture Radar	IW	A	SAR Standard L1 Product	GRD	DESCENDING	80	H-10	[VV, VH]
2015-03-10	Synthetic Aperture Radar	IW	A	SAR Standard L1 Product	GRD	ASCENDING	175	H-10	[VV, VH]
2015-03-16	Synthetic Aperture Radar	IW	A	SAR Standard L1 Product	GRD	DESCENDING	80	H-10	[VV, VH]
2015-03-22	Synthetic Aperture Radar	IW	A	SAR Standard L1 Product	GRD	ASCENDING	175	H-10	[VV, VH]
2015-03-28	Synthetic Aperture Radar	IW	A	SAR Standard L1 Product	GRD	DESCENDING	80	H-10	[VV, VH]
2015-04-03	Synthetic Aperture Radar	IW	A	SAR Standard L1 Product	GRD	ASCENDING	175	H-10	[VV, VH]
2015-04-09	Synthetic Aperture Radar	IW	A	SAR Standard L1 Product	GRD	DESCENDING	80	H-10	[VV, VH]
2015-04-15	Synthetic Aperture Radar	IW	A	SAR Standard L1 Product	GRD	ASCENDING	175	H-10	[VV, VH]

2015-04-21	Synthetic Aperture Radar	IW	A	SAR Standard L1 Product	GRD	DESCENDING	80	H-10	[VV, VH]
2015-04-27	Synthetic Aperture Radar	IW	A	SAR Standard L1 Product	GRD	ASCENDING	175	H-10	[VV, VH]
2015-05-03	Synthetic Aperture Radar	IW	A	SAR Standard L1 Product	GRD	DESCENDING	80	H-10	[VV, VH]
2015-05-09	Synthetic Aperture Radar	IW	A	SAR Standard L1 Product	GRD	ASCENDING	175	H-10	[VV, VH]
2015-05-15	Synthetic Aperture Radar	IW	A	SAR Standard L1 Product	GRD	DESCENDING	80	H-10	[VV, VH]
2015-05-21	Synthetic Aperture Radar	IW	A	SAR Standard L1 Product	GRD	ASCENDING	175	H-10	[VV, VH]
2015-05-27	Synthetic Aperture Radar	IW	A	SAR Standard L1 Product	GRD	DESCENDING	80	H-10	[VV, VH]
2015-06-02	Synthetic Aperture Radar	IW	A	SAR Standard L1 Product	GRD	ASCENDING	175	H-10	[VV, VH]
2015-06-08	Synthetic Aperture Radar	IW	A	SAR Standard L1 Product	GRD	DESCENDING	80	H-10	[VV, VH]
2015-06-14	Synthetic Aperture Radar	IW	A	SAR Standard L1 Product	GRD	ASCENDING	175	H-10	[VV, VH]
2015-06-20	Synthetic Aperture Radar	IW	A	SAR Standard L1 Product	GRD	DESCENDING	80	H-10	[VV, VH]

2015-06-26	Synthetic Aperture Radar	IW	A	SAR Standard L1 Product	GRD	ASCENDING	175	H-10	[VV, VH]
2015-07-20	Synthetic Aperture Radar	IW	A	SAR Standard L1 Product	GRD	ASCENDING	175	H-10	[VV, VH]
2015-07-26	Synthetic Aperture Radar	IW	A	SAR Standard L1 Product	GRD	DESCENDING	80	H-10	[VV, VH]
2015-08-13	Synthetic Aperture Radar	IW	A	SAR Standard L1 Product	GRD	ASCENDING	175	H-10	[VV, VH]
2015-08-19	Synthetic Aperture Radar	IW	A	SAR Standard L1 Product	GRD	DESCENDING	80	H-10	[VV, VH]
2015-08-25	Synthetic Aperture Radar	IW	A	SAR Standard L1 Product	GRD	ASCENDING	175	H-10	[VV, VH]
2015-08-31	Synthetic Aperture Radar	IW	A	SAR Standard L1 Product	GRD	DESCENDING	80	H-10	[VV, VH]
2015-11-23	Synthetic Aperture Radar	IW	A	SAR Standard L1 Product	GRD	DESCENDING	80	H-10	[VV, VH]
2015-11-29	Synthetic Aperture Radar	IW	A	SAR Standard L1 Product	GRD	ASCENDING	175	H-10	[VV, VH]
2015-12-05	Synthetic Aperture Radar	IW	A	SAR Standard L1 Product	GRD	DESCENDING	80	H-10	[VV, VH]
2015-12-11	Synthetic Aperture Radar	IW	A	SAR Standard L1 Product	GRD	ASCENDING	175	H-10	[VV, VH]

2015-12-17	Synthetic Aperture Radar	IW	A	SAR Standard L1 Product	GRD	DESCENDING	80	H-10	[VV, VH]
2015-12-23	Synthetic Aperture Radar	IW	A	SAR Standard L1 Product	GRD	ASCENDING	175	H-10	[VV, VH]
2015-12-29	Synthetic Aperture Radar	IW	A	SAR Standard L1 Product	GRD	DESCENDING	80	H-10	[VV, VH]
2016-01-04	Synthetic Aperture Radar	IW	A	SAR Standard L1 Product	GRD	ASCENDING	175	H-10	[VV, VH]
2016-01-10	Synthetic Aperture Radar	IW	A	SAR Standard L1 Product	GRD	DESCENDING	80	H-10	[VV, VH]
2016-01-22	Synthetic Aperture Radar	IW	A	SAR Standard L1 Product	GRD	DESCENDING	80	H-10	[VV, VH]
2016-01-28	Synthetic Aperture Radar	IW	A	SAR Standard L1 Product	GRD	ASCENDING	175	H-10	[VV, VH]
2016-01-28	Synthetic Aperture Radar	IW	A	SAR Standard L1 Product	GRD	ASCENDING	175	H-10	[VV, VH]
2016-02-03	Synthetic Aperture Radar	IW	A	SAR Standard L1 Product	GRD	DESCENDING	80	H-10	[VV, VH]
2016-02-03	Synthetic Aperture Radar	IW	A	SAR Standard L1 Product	GRD	DESCENDING	80	H-10	[VV, VH]
2016-02-09	Synthetic Aperture Radar	IW	A	SAR Standard L1 Product	GRD	ASCENDING	175	H-10	[VV, VH]

2016-02-15	Synthetic Aperture Radar	IW	A	SAR Standard L1 Product	GRD	DESCENDING	80	H-10	[VV, VH]
2016-02-21	Synthetic Aperture Radar	IW	A	SAR Standard L1 Product	GRD	ASCENDING	175	H-10	[VV, VH]
2016-02-27	Synthetic Aperture Radar	IW	A	SAR Standard L1 Product	GRD	DESCENDING	80	H-10	[VV, VH]
2016-03-04	Synthetic Aperture Radar	IW	A	SAR Standard L1 Product	GRD	ASCENDING	175	H-10	[VV, VH]
2016-03-10	Synthetic Aperture Radar	IW	A	SAR Standard L1 Product	GRD	DESCENDING	80	H-10	[VV, VH]
2016-03-16	Synthetic Aperture Radar	IW	A	SAR Standard L1 Product	GRD	ASCENDING	175	H-10	[VV, VH]
2016-03-28	Synthetic Aperture Radar	IW	A	SAR Standard L1 Product	GRD	ASCENDING	175	H-10	[VV, VH]
2016-04-03	Synthetic Aperture Radar	IW	A	SAR Standard L1 Product	GRD	DESCENDING	80	H-10	[VV, VH]
2016-04-09	Synthetic Aperture Radar	IW	A	SAR Standard L1 Product	GRD	ASCENDING	175	H-10	[VV, VH]
2016-04-15	Synthetic Aperture Radar	IW	A	SAR Standard L1 Product	GRD	DESCENDING	80	H-10	[VV, VH]
2016-04-21	Synthetic Aperture Radar	IW	A	SAR Standard L1 Product	GRD	ASCENDING	175	H-10	[VV, VH]

2016-04-27	Synthetic Aperture Radar	IW	A	SAR Standard L1 Product	GRD	DESCENDING	80	H-10	[VV, VH]
2016-05-03	Synthetic Aperture Radar	IW	A	SAR Standard L1 Product	GRD	ASCENDING	175	H-10	[VV, VH]
2016-05-09	Synthetic Aperture Radar	IW	A	SAR Standard L1 Product	GRD	DESCENDING	80	H-10	[VV, VH]
2016-05-15	Synthetic Aperture Radar	IW	A	SAR Standard L1 Product	GRD	ASCENDING	175	H-10	[VV, VH]
2016-05-21	Synthetic Aperture Radar	IW	A	SAR Standard L1 Product	GRD	DESCENDING	80	H-10	[VV, VH]
2016-05-27	Synthetic Aperture Radar	IW	A	SAR Standard L1 Product	GRD	ASCENDING	175	H-10	[VV, VH]
2016-06-02	Synthetic Aperture Radar	IW	A	SAR Standard L1 Product	GRD	DESCENDING	80	H-10	[VV, VH]
2016-06-08	Synthetic Aperture Radar	IW	A	SAR Standard L1 Product	GRD	ASCENDING	175	H-10	[VV, VH]
2016-06-14	Synthetic Aperture Radar	IW	A	SAR Standard L1 Product	GRD	DESCENDING	80	H-10	[VV, VH]
2016-07-02	Synthetic Aperture Radar	IW	A	SAR Standard L1 Product	GRD	ASCENDING	175	H-10	[VV, VH]
2016-07-08	Synthetic Aperture Radar	IW	A	SAR Standard L1 Product	GRD	DESCENDING	80	H-10	[VV, VH]

2016-07-14	Synthetic Aperture Radar	IW	A	SAR Standard L1 Product	GRD	ASCENDING	175	H-10	[VV, VH]
2016-07-26	Synthetic Aperture Radar	IW	A	SAR Standard L1 Product	GRD	ASCENDING	175	H-10	[VV, VH]
2016-08-01	Synthetic Aperture Radar	IW	A	SAR Standard L1 Product	GRD	DESCENDING	80	H-10	[VV, VH]
2016-08-07	Synthetic Aperture Radar	IW	A	SAR Standard L1 Product	GRD	ASCENDING	175	H-10	[VV, VH]
2016-08-13	Synthetic Aperture Radar	IW	A	SAR Standard L1 Product	GRD	DESCENDING	80	H-10	[VV, VH]
2016-08-19	Synthetic Aperture Radar	IW	A	SAR Standard L1 Product	GRD	ASCENDING	175	H-10	[VV, VH]
2016-08-25	Synthetic Aperture Radar	IW	A	SAR Standard L1 Product	GRD	DESCENDING	80	H-10	[VV, VH]
2016-08-31	Synthetic Aperture Radar	IW	A	SAR Standard L1 Product	GRD	ASCENDING	175	H-10	[VV, VH]
2016-09-06	Synthetic Aperture Radar	IW	A	SAR Standard L1 Product	GRD	DESCENDING	80	H-10	[VV, VH]
2016-09-12	Synthetic Aperture Radar	IW	A	SAR Standard L1 Product	GRD	ASCENDING	175	H-10	[VV, VH]
2016-09-18	Synthetic Aperture Radar	IW	A	SAR Standard L1 Product	GRD	DESCENDING	80	H-10	[VV, VH]

2016-09-24	Synthetic Aperture Radar	IW	A	SAR Standard L1 Product	GRD	ASCENDING	175	H-10	[VV, VH]
2016-10-06	Synthetic Aperture Radar	IW	B	SAR Standard L1 Product	GRD	DESCENDING	80	H-10	[VV, VH]
2016-10-06	Synthetic Aperture Radar	IW	A	SAR Standard L1 Product	GRD	ASCENDING	175	H-10	[VV, VH]
2016-11-23	Synthetic Aperture Radar	IW	A	SAR Standard L1 Product	GRD	ASCENDING	175	H-10	[VV, VH]
2016-11-23	Synthetic Aperture Radar	IW	B	SAR Standard L1 Product	GRD	DESCENDING	80	H-10	[VV, VH]
2016-12-05	Synthetic Aperture Radar	IW	B	SAR Standard L1 Product	GRD	DESCENDING	80	H-10	[VV, VH]
2016-12-05	Synthetic Aperture Radar	IW	A	SAR Standard L1 Product	GRD	ASCENDING	175	H-10	[VV, VH]
2016-12-17	Synthetic Aperture Radar	IW	A	SAR Standard L1 Product	GRD	ASCENDING	175	H-10	[VV, VH]
2016-12-17	Synthetic Aperture Radar	IW	B	SAR Standard L1 Product	GRD	DESCENDING	80	H-10	[VV, VH]
2016-12-23	Synthetic Aperture Radar	IW	A	SAR Standard L1 Product	GRD	DESCENDING	80	H-10	[VV, VH]
2016-12-23	Synthetic Aperture Radar	IW	B	SAR Standard L1 Product	GRD	ASCENDING	175	H-10	[VV, VH]

2017-06-03	Synthetic Aperture Radar	IW	B	SAR Standard L1 Product	GRD	DESCENDING	80	H-10	[VV, VH]
2017-06-03	Synthetic Aperture Radar	IW	A	SAR Standard L1 Product	GRD	ASCENDING	175	H-10	[VV, VH]
2017-06-09	Synthetic Aperture Radar	IW	A	SAR Standard L1 Product	GRD	DESCENDING	80	H-10	[VV, VH]
2017-06-09	Synthetic Aperture Radar	IW	B	SAR Standard L1 Product	GRD	ASCENDING	175	H-10	[VV, VH]
2017-06-15	Synthetic Aperture Radar	IW	B	SAR Standard L1 Product	GRD	DESCENDING	80	H-10	[VV, VH]
2017-06-15	Synthetic Aperture Radar	IW	A	SAR Standard L1 Product	GRD	ASCENDING	175	H-10	[VV, VH]
2017-06-21	Synthetic Aperture Radar	IW	B	SAR Standard L1 Product	GRD	ASCENDING	175	H-10	[VV, VH]
2017-06-21	Synthetic Aperture Radar	IW	A	SAR Standard L1 Product	GRD	DESCENDING	80	H-10	[VV, VH]
2017-06-27	Synthetic Aperture Radar	IW	A	SAR Standard L1 Product	GRD	ASCENDING	175	H-10	[VV, VH]
2017-06-27	Synthetic Aperture Radar	IW	B	SAR Standard L1 Product	GRD	DESCENDING	80	H-10	[VV, VH]
2017-07-03	Synthetic Aperture Radar	IW	B	SAR Standard L1 Product	GRD	ASCENDING	175	H-10	[VV, VH]

2017-07-03	Synthetic Aperture Radar	IW	A	SAR Standard L1 Product	GRD	DESCENDING	80	H-10	[VV, VH]
2017-07-09	Synthetic Aperture Radar	IW	B	SAR Standard L1 Product	GRD	DESCENDING	80	H-10	[VV, VH]
2017-07-09	Synthetic Aperture Radar	IW	A	SAR Standard L1 Product	GRD	ASCENDING	175	H-10	[VV, VH]
2017-07-15	Synthetic Aperture Radar	IW	B	SAR Standard L1 Product	GRD	ASCENDING	175	H-10	[VV, VH]
2017-07-15	Synthetic Aperture Radar	IW	A	SAR Standard L1 Product	GRD	DESCENDING	80	H-10	[VV, VH]
2017-07-21	Synthetic Aperture Radar	IW	B	SAR Standard L1 Product	GRD	DESCENDING	80	H-10	[VV, VH]
2017-07-21	Synthetic Aperture Radar	IW	A	SAR Standard L1 Product	GRD	ASCENDING	175	H-10	[VV, VH]
2017-08-20	Synthetic Aperture Radar	IW	B	SAR Standard L1 Product	GRD	ASCENDING	175	H-10	[VV, VH]
2017-08-20	Synthetic Aperture Radar	IW	A	SAR Standard L1 Product	GRD	DESCENDING	80	H-10	[VV, VH]
2017-08-26	Synthetic Aperture Radar	IW	A	SAR Standard L1 Product	GRD	ASCENDING	175	H-10	[VV, VH]
2017-09-01	Synthetic Aperture Radar	IW	A	SAR Standard L1 Product	GRD	DESCENDING	80	H-10	[VV, VH]

2017-09-01	Synthetic Aperture Radar	IW	B	SAR Standard L1 Product	GRD	ASCENDING	175	H-10	[VV, VH]
2017-09-07	Synthetic Aperture Radar	IW	B	SAR Standard L1 Product	GRD	DESCENDING	80	H-10	[VV, VH]
2017-09-07	Synthetic Aperture Radar	IW	A	SAR Standard L1 Product	GRD	ASCENDING	175	H-10	[VV, VH]
2017-10-01	Synthetic Aperture Radar	IW	B	SAR Standard L1 Product	GRD	DESCENDING	80	H-10	[VV, VH]
2017-10-07	Synthetic Aperture Radar	IW	B	SAR Standard L1 Product	GRD	ASCENDING	175	H-10	[VV, VH]
2017-10-07	Synthetic Aperture Radar	IW	A	SAR Standard L1 Product	GRD	DESCENDING	80	H-10	[VV, VH]
2017-10-25	Synthetic Aperture Radar	IW	A	SAR Standard L1 Product	GRD	ASCENDING	175	H-10	[VV, VH]
2017-10-25	Synthetic Aperture Radar	IW	B	SAR Standard L1 Product	GRD	DESCENDING	80	H-10	[VV, VH]
2017-11-12	Synthetic Aperture Radar	IW	B	SAR Standard L1 Product	GRD	ASCENDING	175	H-10	[VV, VH]
2017-11-12	Synthetic Aperture Radar	IW	A	SAR Standard L1 Product	GRD	DESCENDING	80	H-10	[VV, VH]
2018-01-23	Synthetic Aperture Radar	IW	B	SAR Standard L1 Product	GRD	ASCENDING	175	H-10	[VV, VH]

2018-01-23	Synthetic Aperture Radar	IW	A	SAR Standard L1 Product	GRD	DESCENDING	80	H-10	[VV, VH]
2018-01-29	Synthetic Aperture Radar	IW	A	SAR Standard L1 Product	GRD	ASCENDING	175	H-10	[VV, VH]
2018-01-29	Synthetic Aperture Radar	IW	B	SAR Standard L1 Product	GRD	DESCENDING	80	H-10	[VV, VH]
2018-02-04	Synthetic Aperture Radar	IW	A	SAR Standard L1 Product	GRD	DESCENDING	80	H-10	[VV, VH]
2018-02-04	Synthetic Aperture Radar	IW	B	SAR Standard L1 Product	GRD	ASCENDING	175	H-10	[VV, VH]
2018-02-10	Synthetic Aperture Radar	IW	A	SAR Standard L1 Product	GRD	ASCENDING	175	H-10	[VV, VH]
2018-02-10	Synthetic Aperture Radar	IW	B	SAR Standard L1 Product	GRD	DESCENDING	80	H-10	[VV, VH]
2018-02-16	Synthetic Aperture Radar	IW	A	SAR Standard L1 Product	GRD	DESCENDING	80	H-10	[VV, VH]
2018-02-16	Synthetic Aperture Radar	IW	B	SAR Standard L1 Product	GRD	ASCENDING	175	H-10	[VV, VH]
2018-02-22	Synthetic Aperture Radar	IW	A	SAR Standard L1 Product	GRD	ASCENDING	175	H-10	[VV, VH]
2018-02-22	Synthetic Aperture Radar	IW	B	SAR Standard L1 Product	GRD	DESCENDING	80	H-10	[VV, VH]

2018-02-28	Synthetic Aperture Radar	IW	A	SAR Standard L1 Product	GRD	DESCENDING	80	H-10	[VV, VH]
2018-02-28	Synthetic Aperture Radar	IW	B	SAR Standard L1 Product	GRD	ASCENDING	175	H-10	[VV, VH]
2018-03-06	Synthetic Aperture Radar	IW	A	SAR Standard L1 Product	GRD	ASCENDING	175	H-10	[VV, VH]
2018-03-06	Synthetic Aperture Radar	IW	B	SAR Standard L1 Product	GRD	DESCENDING	80	H-10	[VV, VH]
2018-03-12	Synthetic Aperture Radar	IW	A	SAR Standard L1 Product	GRD	DESCENDING	80	H-10	[VV, VH]
2018-03-12	Synthetic Aperture Radar	IW	B	SAR Standard L1 Product	GRD	ASCENDING	175	H-10	[VV, VH]
2018-03-18	Synthetic Aperture Radar	IW	A	SAR Standard L1 Product	GRD	ASCENDING	175	H-10	[VV, VH]
2018-03-18	Synthetic Aperture Radar	IW	B	SAR Standard L1 Product	GRD	DESCENDING	80	H-10	[VV, VH]
2018-03-24	Synthetic Aperture Radar	IW	A	SAR Standard L1 Product	GRD	DESCENDING	80	H-10	[VV, VH]
2018-03-24	Synthetic Aperture Radar	IW	B	SAR Standard L1 Product	GRD	ASCENDING	175	H-10	[VV, VH]
2018-03-30	Synthetic Aperture Radar	IW	A	SAR Standard L1 Product	GRD	ASCENDING	175	H-10	[VV, VH]

2018-03-30	Synthetic Aperture Radar	IW	B	SAR Standard L1 Product	GRD	DESCENDING	80	H-10	[VV, VH]
2018-04-05	Synthetic Aperture Radar	IW	A	SAR Standard L1 Product	GRD	DESCENDING	80	H-10	[VV, VH]
2018-04-05	Synthetic Aperture Radar	IW	B	SAR Standard L1 Product	GRD	ASCENDING	175	H-10	[VV, VH]
2018-04-11	Synthetic Aperture Radar	IW	A	SAR Standard L1 Product	GRD	ASCENDING	175	H-10	[VV, VH]
2018-04-11	Synthetic Aperture Radar	IW	B	SAR Standard L1 Product	GRD	DESCENDING	80	H-10	[VV, VH]

APPENDIX B – Landsat 8 Metadata of the Selected Images

IMAGE ID	Date	CLOUD COVER (LAND)	SATELLITE	WRS PATH	WRS ROW
LC08_184033_20150310	2015-03-10	93,24	LANDSAT_8	184	33
LC08_185033_20150317	2015-03-17	99,91	LANDSAT_8	185	33
LC08_185033_20150402	2015-04-02	12,9	LANDSAT_8	185	33
LC08_184033_20150411	2015-04-11	2,62	LANDSAT_8	184	33
LC08_185033_20150418	2015-04-18	22,31	LANDSAT_8	185	33
LC08_184033_20150427	2015-04-27	12,89	LANDSAT_8	184	33
LC08_185033_20150504	2015-05-04	1,35	LANDSAT_8	185	33
LC08_184033_20150513	2015-05-13	7,67	LANDSAT_8	184	33
LC08_185033_20150520	2015-05-20	18,15	LANDSAT_8	185	33
LC08_184033_20150529	2015-05-29	45,75	LANDSAT_8	184	33
LC08_185033_20150605	2015-06-05	16,98	LANDSAT_8	185	33
LC08_184033_20150614	2015-06-14	2,13	LANDSAT_8	184	33
LC08_185033_20150621	2015-06-21	46,58	LANDSAT_8	185	33
LC08_184033_20150630	2015-06-30	81,8	LANDSAT_8	184	33
LC08_185033_20150707	2015-07-07	3,2	LANDSAT_8	185	33
LC08_184033_20150716	2015-07-16	17,65	LANDSAT_8	184	33
LC08_185033_20150723	2015-07-23	0,89	LANDSAT_8	185	33
LC08_184033_20150801	2015-08-01	1,21	LANDSAT_8	184	33
LC08_185033_20150808	2015-08-08	45,63	LANDSAT_8	185	33
LC08_184033_20150817	2015-08-17	12,86	LANDSAT_8	184	33
LC08_185033_20150824	2015-08-24	11,29	LANDSAT_8	185	33
LC08_184033_20151121	2015-11-21	98,42	LANDSAT_8	184	33
LC08_185033_20151128	2015-11-28	77,52	LANDSAT_8	185	33
LC08_184033_20151207	2015-12-07	6,48	LANDSAT_8	184	33
LC08_185033_20151214	2015-12-14	49,05	LANDSAT_8	185	33
LC08_184033_20151223	2015-12-23	1,3	LANDSAT_8	184	33
LC08_185033_20151230	2015-12-30	27,74	LANDSAT_8	185	33
LC08_184033_20160108	2016-01-08	3,25	LANDSAT_8	184	33
LC08_184033_20160124	2016-01-24	2,8	LANDSAT_8	184	33
LC08_185033_20160131	2016-01-31	52,15	LANDSAT_8	185	33
LC08_184033_20160209	2016-02-09	30,96	LANDSAT_8	184	33
LC08_185033_20160216	2016-02-16	96,32	LANDSAT_8	185	33
LC08_185033_20160303	2016-03-03	82,08	LANDSAT_8	185	33
LC08_185033_20160319	2016-03-19	24,27	LANDSAT_8	185	33
LC08_184033_20160328	2016-03-28	56,8	LANDSAT_8	184	33
LC08_185033_20160404	2016-04-04	0,66	LANDSAT_8	185	33
LC08_184033_20160413	2016-04-13	12,61	LANDSAT_8	184	33

LC08_185033_20160420	2016-04-20	2,69	LANDSAT_8	185	33
LC08_184033_20160429	2016-04-29	96,95	LANDSAT_8	184	33
LC08_185033_20160506	2016-05-06	38,13	LANDSAT_8	185	33
LC08_184033_20160515	2016-05-15	29,36	LANDSAT_8	184	33
LC08_185033_20160522	2016-05-22	45,06	LANDSAT_8	185	33
LC08_184033_20160531	2016-05-31	8,12	LANDSAT_8	184	33
LC08_185033_20160607	2016-06-07	16,35	LANDSAT_8	185	33
LC08_184033_20160616	2016-06-16	0,81	LANDSAT_8	184	33
LC08_185033_20160623	2016-06-23	0,86	LANDSAT_8	185	33
LC08_184033_20160702	2016-07-02	10,46	LANDSAT_8	184	33
LC08_185033_20160709	2016-07-09	0,23	LANDSAT_8	185	33
LC08_184033_20160718	2016-07-18	1,64	LANDSAT_8	184	33
LC08_185033_20160725	2016-07-25	28,73	LANDSAT_8	185	33
LC08_184033_20160803	2016-08-03	5,89	LANDSAT_8	184	33
LC08_185033_20160810	2016-08-10	7,63	LANDSAT_8	185	33
LC08_184033_20160819	2016-08-19	1,69	LANDSAT_8	184	33
LC08_185033_20160826	2016-08-26	3,5	LANDSAT_8	185	33
LC08_184033_20160904	2016-09-04	11,16	LANDSAT_8	184	33
LC08_185033_20160911	2016-09-11	59,84	LANDSAT_8	185	33
LC08_184033_20160920	2016-09-20	25,21	LANDSAT_8	184	33
LC08_185033_20160927	2016-09-27	23,17	LANDSAT_8	185	33
LC08_184033_20161006	2016-10-06	10,01	LANDSAT_8	184	33
LC08_184033_20161123	2016-11-23	56,78	LANDSAT_8	184	33
LC08_185033_20161130	2016-11-30	76,87	LANDSAT_8	185	33
LC08_184033_20170603	2017-06-03	48,97	LANDSAT_8	184	33
LC08_185033_20170610	2017-06-10	16,31	LANDSAT_8	185	33
LC08_184033_20170619	2017-06-19	40,02	LANDSAT_8	184	33
LC08_185033_20170626	2017-06-26	1,43	LANDSAT_8	185	33
LC08_184033_20170705	2017-07-05	41,19	LANDSAT_8	184	33
LC08_185033_20170712	2017-07-12	0,06	LANDSAT_8	185	33
LC08_184033_20170721	2017-07-21	4,83	LANDSAT_8	184	33
LC08_184033_20170822	2017-08-22	64,29	LANDSAT_8	184	33
LC08_185033_20170829	2017-08-29	61,04	LANDSAT_8	185	33
LC08_184033_20170907	2017-09-07	0,06	LANDSAT_8	184	33
LC08_184033_20170923	2017-09-23	1,05	LANDSAT_8	184	33
LC08_185033_20170930	2017-09-30	49,7	LANDSAT_8	185	33
LC08_184033_20171009	2017-10-09	0,13	LANDSAT_8	184	33
LC08_184033_20171025	2017-10-25	75,77	LANDSAT_8	184	33
LC08_184033_20171110	2017-11-10	10,92	LANDSAT_8	184	33
LC08_184033_20180129	2018-01-29	1,85	LANDSAT_8	184	33
LC08_185033_20180205	2018-02-05	2,73	LANDSAT_8	185	33

LC08_184033_20180214	2018-02-14	47,63	LANDSAT_8	184	33
LC08_184033_20180302	2018-03-02	94,35	LANDSAT_8	184	33
LC08_185033_20180309	2018-03-09	83,75	LANDSAT_8	185	33
LC08_184033_20180318	2018-03-18	97,52	LANDSAT_8	184	33
LC08_184033_20180403	2018-04-03	1,54	LANDSAT_8	184	33
LC08_185033_20180410	2018-04-10	32,15	LANDSAT_8	185	33

List Of Figures

Figure 1: Επίγειες μετρήσεων εδαφικής υγρασίας (In-situ) και τιμές πολυφασματικών δεικτών NDVI, NDMI, MI. Συνολικά 328 μετρήσεις και αντίστοιχες τιμές (x10) NDVI, (x10) NDMI και (x3) MI σε ένα διαστημα +/- 2 ημερών. 9
Figure 2: Επίγειες μετρήσεων εδαφικής υγρασίας (In-situ) και τιμές οπισθοσκέδασης VV (db). Συνολικά 865 μετρήσεις και αντίστοιχες τιμές (+30) VV σε ένα διαστημα +/- 2 ημερών. 10
Figure 3: Σύγκριση υπολογισμένων και πραγματικών τιμών υγρασία με ανεξάρτητη μεταβλητή τον NDVI (αριστερά) και τον NDMI (δεξιά) στο Μοντέλο Γραμμικής Παλινδρόμησης (n = 66 παρατηρήσεις των δεδομένων επαλήθευσης). 12
Figure 4: Σύγκριση υπολογισμένων και πραγματικών τιμών υγρασίας με ανεξάρτητη μεταβλητή τον MI (αριστερά) (n = 66 παρατηρήσεις των δεδομένων επαλήθευσης) και την οπισθοσκέδαση VV (δεξιά) (n = 173 παρατηρήσεις των δεδομένων επαλήθευσης) στο Μοντέλο Γραμμικής Παλινδρόμησης. 12
Figure 5: Σύγκριση υπολογισμένων και πραγματικών τιμών υγρασίας με ανεξάρτητη μεταβλητή τον NDVI (αριστερά) και του NDMI (δεξιά) στο Μοντέλο Πολυωνυμικής Παλινδρόμησης (n = 66 παρατηρήσεις των δεδομένων επαλήθευσης). 13
Figure 6: Σύγκριση υπολογισμένων και πραγματικών τιμών υγρασίας με ανεξάρτητη μεταβλητή τον MI (αριστερά) (n = 66 παρατηρήσεις των δεδομένων επαλήθευσης) και την οπισθοσκέδαση VV (δεξιά) (n = 173 παρατηρήσεις των δεδομένων επαλήθευσης) στο Μοντέλο Πολυωνυμικής Παλινδρόμησης. 13
Figure 7: Σύγκριση υπολογισμένων και πραγματικών τιμών υγρασίας με ανεξάρτητη μεταβλητή τον MI (αριστερά) (n = 66 παρατηρήσεις των δεδομένων επαλήθευσης) και την οπισθοσκέδαση VV (δεξιά) (n = 173 παρατηρήσεις των δεδομένων επαλήθευσης) στο Γενικευμένο Προσθετικό Μοντέλο. 14
Figure 8: Σύγκριση υπολογισμένων και πραγματικών τιμών υγρασίας με ανεξάρτητη μεταβλητή τον NDVI (αριστερά) και του NDMI (δεξιά) στο Γενικευμένο Προσθετικό Μοντέλο (n = 66 παρατηρήσεις των δεδομένων επαλήθευσης). 14
Figure 9: Σύγκριση υπολογισμένων και πραγματικών τιμών υγρασίας με ανεξάρτητες μεταβλητές τον NDVI και τις τιμές οπισθοσκέδασης VV στο Μοντέλο Τεχνητών Νευρωνικών Δικτύων (n = 114 παρατηρήσεις). 15
Figure 10: Pore spaces of soil (Source: https://www.jove.com) 1
Figure 11: Comparison of the porosity of sandy soil and clay soil 2
Figure 12: Soil Moisture Conditions 3
Figure 13: Passive (left) and Active (right) sensors. Source: NASA (www.nasa.gov) 5
Figure 14: Sentinel-1 spacecraft (image credit: ESA, TAS-I) 6
Figure 15: Overview of a Sentinel 1 mission spacecraft. (Source: https://sentinel.esa.int) 7
Figure 16: Sentinel 1 Orbit Tube (https://sentinel.esa.int/web/sentinel/missions/sentinel-1/satellite-description/orbit) 8
Figure 17: Sentinel 1 Coverage (Source: https://sentinel.esa.int) 8
Figure 18: Sentinel 1 Constellation and orbits (Source: https://sentinel.esa.int) 9
Figure 19: Sentinel 1 Modes (Source: https://sentinel.esa.int) 10
Figure 20: The OLI Instrument (Source: https://landsat.usgs.gov) 13
Figure 21: The TIRS Instrument (https://landsat.usgs.gov) 13
Figure 22: Spectral Bands of Landsat 8 and Landsat 7 (Graphic created by L.Rocchio & J.Barsi., accessed through https://landsat.gsfc.nasa.gov) 14

Figure 23: The study area including the Arta plain and the Amvrakikos Wetlands National Park. (Source: http://arta.irrigation-management.eu/).. 18
Figure 24: The irrigation scheme of the plain of Arta (white lines;Arta (west part); black lines; Peta-Kompoti (east part)), the 3 rivers (blue lines; from left to right: Louros, Aracthos and Vovos) and the 3 main drainage canals of the plain (yellow lines; from left to right: Salaoras (DC1), Fidocastrou (DC2) and Neochoriou (DC3)) (Source: Tsirogiannis et al. 2015) 19
Figure 25: Map of In-Situ Measurements's Locations (Background Image by Bing Maps).................. 21
Figure 26: The User Interface of the Google Earth Engine Code Editor 27
Figure 27: Google Earth Engine's System Architecture... 30
Figure 28: Users download R and install Packages (uploaded by Statisticians around the world) to their own computer via their nearest CRAN 31
Figure 29: The R environment 32
Figure 30: RStudio User Interface.. 32
Figure 31: Flowchart of the applied methodology (purple color indicates the processing steps in GEE, yellow color indicates the processing steps that were executed in R)... 33
Figure 32: Vegetation indices with percentage of radiations emitted (Source: www.agricolus.com) 35
Figure 33: NDVI value interpretation (Source: www.agricolus.com) 35
Figure 34: Soil Moisture In-Situ Measurements and values of NDVI, NDMI and MI, retrieved by Landsat 8 data. A total of 328 measurements of (x10) NDVI, (x10) NDMI and (x3) MI during a time range difference of +/- 2 days. 37
Figure 35: In-Situ Measurements of Soil Moisture and VV Backscattering values (db). A total of 865 measurements and the corresponding values of (+30) VV Backscattering during a time range of +/- 2 days. 38
Figure 36: Plot of Measured Soil Moisture versus NDVI.. 45
Figure 37: Linear Regression Model using Measured Soil Moisture and NDVI.................................. 46
Figure 38: Predicted vs Measured Soil Moisture using Linear Regression Model and NDVI (n = 66 observations of the validation set)... 47
Figure 39: Plot of Measured Soil Moisture versus NDMI 47
Figure 40: Linear Regression Model using Measured Soil Moisture and NDMI. 48
Figure 41: Predicted vs Measured Soil Moisture using Linear Regression Model and NDMI (n = 66 observations of the validation set)... 49
Figure 42: Plot of Measured Soil Moisture versus MI... 49
Figure 43: Linear Regression Model using Measured Soil Moisture and MI....................................... 50
Figure 44: Predicted vs Measured Soil Moisture using Linear Regression Model and MI (n = 66 observations of the validation set)... 51
Figure 45: Plot of Measured Soil Moisture versus VV Backscattering. 51
Figure 46: Linear Regression Model using Measured Soil Moisture and VV Backscattering. 52
Figure 47: Predicted vs Measured Soil Moisture using Linear Regression Model and VV Backscattering (n = 173 observations of the validation set). 53
Figure 48: Polynomial Regression Model using Measured Soil Moisture and NDVI........................... 54
Figure 49: Predicted vs Measured Soil Moisture using Polynomial Regression Model and NDVI (n = 66 observations of the validation set)... 54
Figure 50: Polynomial Regression Model using Measured Soil Moisture and NDMI. 55
Figure 51: Predicted vs Measured Soil Moisture using Polynomial Regression Model and NDMI (n = 66 observations of the validation set)... 56
Figure 52: Polynomial Regression Model using Measured Soil Moisture and MI............................... 56

Figure 53: Predicted vs Measured Soil Moisture using Polynomial Regression Model and MI (n = 66 observations of the validation set). 57
Figure 54: Polynomial Regression Model using Measured Soil Moisture and VV Backscattering. 58
Figure 55: Predicted vs Measured Soil Moisture using Polynomial Regression Model and VV Backscattering (n = 173 observations of the validation set). 58
Figure 56: Generalized Additive Model using Measured Soil Moisture and NDVI. 59
Figure 57: Predicted vs Measured Soil Moisture using Generalized Additive Models and NDVI (n = 66 observations of the validation set). 60
Figure 58: Generalized Additive Model using Measured Soil Moisture and NDMI. 60
Figure 59: Predicted vs Measured Soil Moisture using Generalized Additive Models and NDMI (n = 66 observations of the validation set). 61
Figure 60: Generalized Additive Model using Measured Soil Moisture and MI. 62
Figure 61: Predicted vs Measured Soil Moisture using Generalized Additive Models and MI (n = 66 observations of the validation set). 62
Figure 62: Generalized Additive Model using Measured Soil Moisture and VV Backscattering. 63
Figure 63: Predicted vs Measured Soil Moisture using Generalized Additive Models and VV Backscattering (n = 173 observations of the validation set). 64
Figure 64: Performance plots of Artificial Neural Networks. 65
Figure 65: Predicted vs Measured Soil Moisture using Artificial Neural Networks, along with VV Backscattering and NDVI (plotted n = 114 observations of the full dataset). 66

List Of Tables

Table 1: Σύνοψη των αποτελεσμάτων των εφαρμοσμένων μοντέλων 15
Table 2: Sentinel 1 Specifications 7
Table 3: Description of the four Acquisition Modes 10
Table 4: IW GRD High Resolution product characteristics per beam mode (Source: https://sentinel.esa.int) 11
Table 5: IW GRD High Resolution product characteristics common to all beams (Source: https://sentinel.esa.int) 11
Table 6: Description of Landsat 8 spectral bands (created by B. Markham, accessed through https://landsat.gsfc.nasa.gov) 14
Table 7: Description of In-situ Measurements’ stations (Source: http://openmeteo.org) 20
Table 8: GEE Landsat 8 Image Collection Band Description (Source: GEE Documentation). 22
Table 9: GEE Sentinel-1 Image Collection Band Description (Source: GEE Documentation) 25
Table 10: Available data in the Google Earth Engine Catalogue (Source: GEE Documentation). 28
Table 11: Landsat 8 Metadata of the Joined Images 39
Table 12: Sentinel 1 Metadata of the Joined Images 40
Table 13: Comparison of the results of the applied methodologies. 66